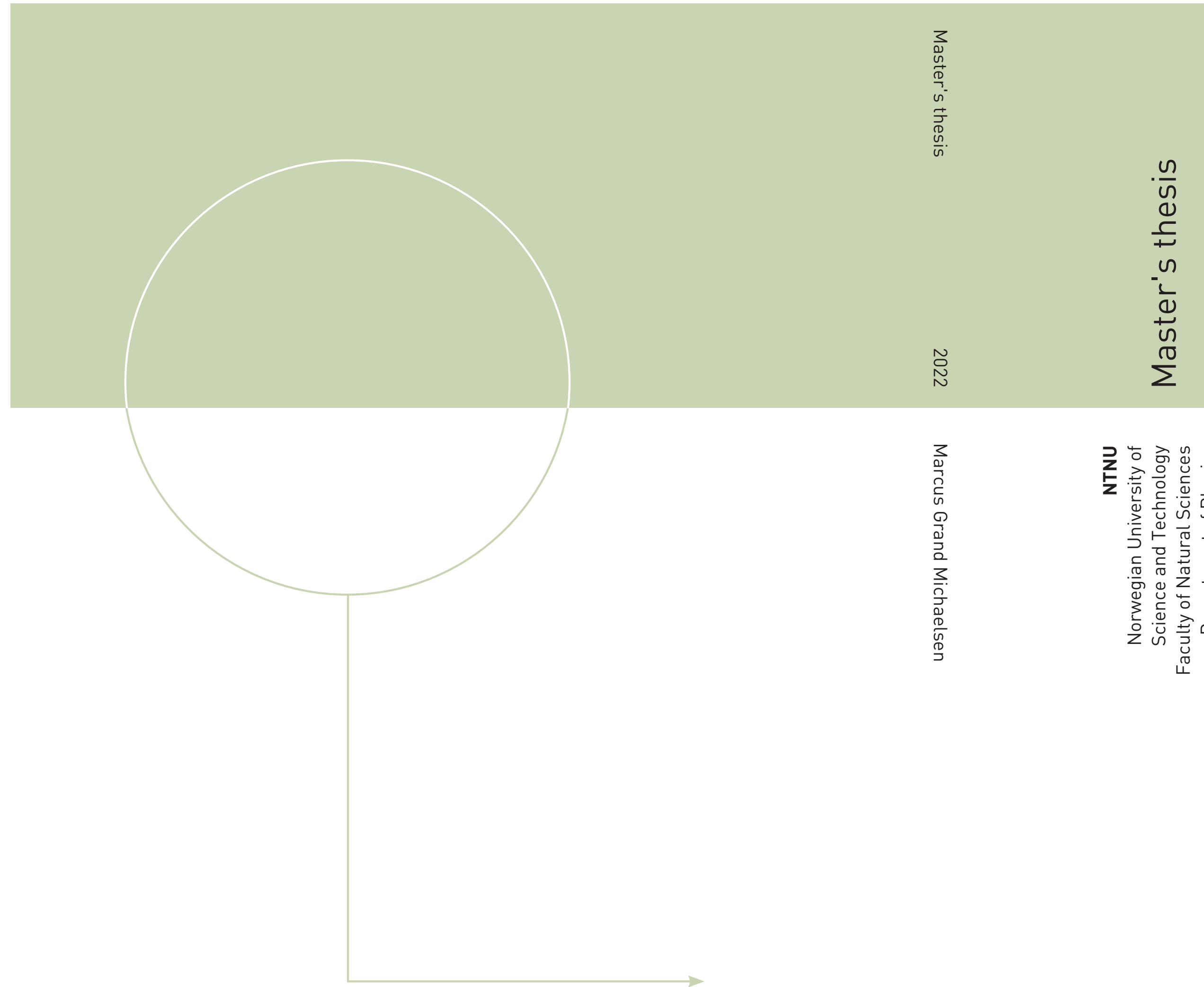

Marcus Grand Michaelsen

Pulsed Laser Deposited TiO_2

X-Ray Diffraction and Raman Spectroscopy Studies

July 2022

NTNU
Norwegian University of
Science and Technology

NTNU
Norwegian University of
Science and Technology

Norwegian University of
Science and Technology

Pulsed Laser Deposited TiO_2

X-Ray Diffraction and Raman Spectroscopy Studies

Marcus Grand Michaelsen

Master of Science in Physics
Submission date: July 2022
Supervisor: Turid Reenaas
Co-supervisor: Hogne Lysne

Norwegian University of Science and Technology
Department of Physics

Abstract

Pulsed laser deposited TiO_2 thin films have been investigated using X-Ray diffraction and Raman spectroscopy. The studied TiO_2 films were undoped and (Cr,N)-codoped. The background for this study was to investigate (Cr,N)-codoped TiO_2 as a candidate for realizing intermediate band materials, for use in intermediate band solar cells—a proposed addition to the third generation of solar cells, aiming to surpass the maximum efficiency of conventional solar cells.

The series of undoped TiO_2 films was deposited using conventional pulsed laser deposition (PLD). The series consisted of six uniform films, each with different deposition parameters, that had been simultaneously deposited on Si (100), LAO (001), STO (001) and sapphire (0001) substrates. In this thesis the films were studied using conventional θ–2θ X-Ray Diffraction (XRD), Grazing-Incidence X-Ray-Diffraction (GIXRD), High Resolution X-Ray Diffraction (HRXRD) and Raman spectroscopy. It was found that the amount of rutile or anatase, texture and structural quality could be tuned by varying the oxygen pressure during deposition. It was also observed that the amount of rutile or anatase in the film was largely influenced by the choice of substrate. Some films on LAO (001) and STO (001) were found to consist of textured, (001)-oriented anatase, even for deposition conditions which favored growth of polycrystalline rutile. However, for these samples the textured anatase seemed to coexist with un-textured, polycrystalline rutile. The different XRD techniques used were evaluated, and it was concluded that the GIXRD method proved insufficient in describing several of the thin films.

The (Cr,N)-codoped TiO_2 films was a series of films deposited using combinatorial PLD. This had resulted in films with continuous gradients in doping concentrations across the samples. For some of the films, the gas flow during deposition had been cycled between O_2 and N_2 in order to hinder formation of chromium oxide, and thus increase the amount of nitrogen in the films. In this thesis it was found that (Cr,N)-codoping, as well as cycling between O_2 and N_2 gas, negatively affected the overall structural quality of the films. Furthermore, characteristics of CrO_2 and Cr_2O_3 was found for all of the doped samples. However, both (Cr,N)-doping and cycling to N_2 seemed to favor growth of rutile (001). For low doping concentrations and deposition under pure O_2 gas, textured (001)-anatase was observed.

The conventional θ–2θ XRD method proved to be an efficient method of characterizing the structural composition of the films. The conclusions drawn from the XRD data generally agreed with the conclusions drawn from Raman spectroscopy, as well as Transmission Electron Microscopy data from the study of a sample that was similar to one of the doped samples presented here.

Sammendrag

Pulserende laserdeponerte TiO_2-tynnfilmer har blitt undersøkt ved røntgendiffraksjon (XRD) og ramanspektroskopi. Utvalget av TiO_2-tynnfilmer bestod av både udopede og (Cr,N)-dopede filmer. Bakgrunnen for studien var å undersøke (Cr,N)-dopet TiO_2 som en kandidat for å realisere mellombånd-solceller. Mellombånd-solceller er et konsept som tilhører tredje generasjons solceller, hvor målet er å øke energieffektiviteten utover dagens konvensjonelle solceller.

Serien med udopede TiO_2-tynnfilmer var deponert gjennom konvensjonell pulserende laserdeponering (PLD). Serien bestoed av seks uniforme filmer, hver av dem deponert med forskjellige deponeringsparametre, som hadde blitt deponert på fire substrater samtidig: Si (100), LAO (001), STO (001) og safir (0001). I denne oppgaven ble filmene undersøkt gjennom konvensjonell θ–2θ XRD, Grazing-Incidence XRD (GIXRD), High Resolution XRD (HRXRD) og ramanspektroskopi. Det ble observert at mengden rutil til anatase, tekstur og strukturell kvalitet kunne påvirkes ved å variere oksygentrykket under deponering. Det ble også observert at mengden rutil til anatase var sterkt påvirket av valg av substrat. Noen av filmene på LAO (001) og STO (001) bestod av teksturert, (001)-orientert anatase, selv for deponeringsparametre som så ut til å favorisere polykrystallinsk rutilvekst. For disse filmene ble det også observert at uteksturert rutil framkom sammen med teksturert anatase. De forskjellige XRD-teknikkene ble evaluert, og det ble konkludert med at GIXRD-metoden ikke var tilstrekkelig for å beskrive flere av filmene.

Utvalget av (Cr,N)-dopede TiO_2-filmer va deponert ved kombinatoriell PLD. Dette hadde resultert i filmer med en kontinuerlig gradient i dopingkonsentrasjoner gjennom prøven. For noen av filmene hadde deponeringsgassen blitt syklet mellom O_2 og N_2 for å hindre dannelsen av kromoksider, og derfor øke mengder nitrogen i filmene. Tegn til CrO_2 eller Cr_2O_3 ble observert for alle de dopede prøvene. Det ble funnet at både (Cr,N)-doping samt N_2-gass frambringte rutil (001) i filmene. For lave dopingkonsentrasjoner og deponering under ren O_2 gass ble teksturert anatase (001) observert.

Den konvensjonelle θ–2θ XRD-metoden var en effektiv teknikk for å gjøre strukturell karakterisering av filmene. Konklusjonene som fremkom av XRD-dataene samstemte generelt godt med konklusjonene fra ramanspektroskopi, så vel som transmisjons elektronmikroskopidata til en lignende prøve for en av de dopede prøvene presentert her.

Acknowledgements

This is my final work as a student at NTNU Trondheim. It has been five amazing years that have had a profound impact on the person I have become so far. I want to thank my supervisor, Professor Turid Reenaas at the Department of Physics—you have provided me with sound guidance while also allowing me to pursue my own curiosity. I am also grateful for your compassionate understanding of what it really means to be a student.

I also want to thank my co-supervisor, PhD Candidate Hogne Lysne, as well as PhD Candidate Thomas Brakstad, who were responsible for the previous groundwork for this thesis. Your willingness to help and cooperate with me and the other master's students in our group has been invaluable. I also want to thank the other master's students, Andreas, Stine, and Petter, for both helpful discussions as well as social morale in the group.

Viviann Hole Pedersen and Tron Arne Nilsen, thank you for training in XRD equipment, as well as for your patience in dealing with my endless questions. I also want to acknowledge NTNU NanoLab for Raman spectroscopy training and facilities.

Finally, I want to thank Stundersamfundet i Trondhjem, Strindens Promenade Orchester, S. Møller storband, Trondhjems studentersangforening, UKA-17, UKA-19, UKA-21 and specifically UKErevyen 21 "Razzmatazz". These organizations are what *truly* defined my years of studying in Trondheim and made me the person I am today.

Marcus Grand Michaelsen

NTNU Trondheim

July 2022

Table of Contents

1 Introduction **1**

2 Theory **5**

2.1 X-ray Diffraction 5

2.1.1 Bragg's Law and The Laue Condition 5

2.1.2 Un-textured, Textured and Single Crystal–Like Materials . . . 7

2.1.3 XRD Measurement Configurations 8

2.2 Raman Spectroscopy 10

2.3 Titanium Dioxide (TiO_2) 11

2.3.1 The Anatase–to–Rutile Phase Transformation 12

2.3.2 XRD Characteristics of Rutile and Anatase 12

2.3.3 Raman Spectra of TiO_2 14

2.4 Pulsed Laser Deposition 16

2.4.1 Combinatorial PLD 17

2.4.2 Epitaxial Film Growth 17

2.4.3 Growth Mechanics 18

2.4.4 Preferred Orientation of Pulsed Laser Deposited Films 19

2.5 Substrate Materials 20

2.6 Pulsed Laser Deposition of TiO_2 Thin Films 22

3 Data Analysis **25**

3.1 Qualitative XRD Analysis 25

3.1.1 Phase Identification 25

3.2 Quantitative XRD Analysis 27

3.2.1 Peak Fitting 27

3.2.2 Uniform and Non-Uniform Strain 28

3.2.3 Crystallite Size Estimation 29

3.2.4 Preferred Orientation and Texture Coefficient 30

3.2.5 Phase Quantification of Rutile and Anatase Mixtures 32

3.2.6 Estimation of Uncertainties 33
3.3 Raman Spectroscopy Analysis 36

4 Experimental Details 37

4.1 Preparation of Uniform Undoped Samples 37
4.2 Continuous Compositional Spread (CCS) Samples 38
4.2.1 CCS–Si–NoCap and CCS–Si–NoCap–Ref 40
4.2.2 CCS-Si-Cap, CCS-Si-Cap-Ref and CCS-LAO-Cap 42
4.3 X-ray Diffraction Setup 44
4.4 Raman Spectroscopy Setup 45

5 Results and Discussion 47

5.1 Uniform Undoped Samples on Si (100) 48
5.1.1 Theta-2Theta Measurements 48
5.1.2 GIXRD Measurements 54
5.1.3 Raman Spectroscopy 57
5.2 Uniform Undoped Samples on LAO (001) 60
5.2.1 Theta–2Theta Measurements 60
5.2.2 GIXRD Measurements 63
5.2.3 Raman Spectroscopy 66
5.2.4 HRXRD Measurements 69
5.3 Uniform Undoped Samples on STO (001) 72
5.3.1 Theta–2Theta Measurements 72
5.3.2 GIXRD Measurements 75
5.3.3 Raman Spectroscopy 78
5.3.4 HRXRD Measurements 80
5.4 Uniform Undoped Samples on Sapphire (0001) 82
5.4.1 Theta–2Theta Measurements 82
5.4.2 GIXRD Measurements 85
5.4.3 Raman Spectroscopy 86

5.4.4 HRXRD Measurements 88
5.5 Summary of Discussion from Characterization of Uniform Undoped Samples 90
5.5.1 Discussion of Deposition Parameters 90
5.5.2 Evaluation of Characterization Methods 92
5.6 Continuous Compositional Spread (CCS) Samples 94
5.6.1 CCS-Si-NoCap-Ref 94
5.6.2 CCS-Si-NoCap 94
5.6.3 CCS-Si-Cap-Ref 101
5.6.4 CCS-Si-Cap 105
5.6.5 CCS-LAO-Cap 112
5.7 Summary of Discussion from Characterization of CCS Samples 115

6 Conclusion **119**

7 Suggestions for Future Work **121**

References **123**

A Basic crystallography **129**

B XRD Signatures of CrO_2, Cr_2O_3 and CrN **131**

C CrN films deposited on silicon **132**

1 Introduction

In February 2022, the United Nations' Intergovernmental Panel on Climate Change (IPCC) released part of the Sixth Assessment Report on climate change. The report concluded with very high confidence that global warming exceeding 1.5 °C in the near-term (2021-2040) will present severe risks to humans and ecosystems. Unless current greenhouse gas (GHG) emissions rapidly decline, prospects for sustainable development will be increasingly limited with such warming in the near-term. The energy sector accounts for 70% percent of world GHG emissions, primarily owing to the use of fossil fuels. [1]

While calls for GHG emission cuts are strong, the world energy demand is increasing as a result of population increase and economic growth. It is clear that a massive global energy transition towards renewable energy sources is critical. The United Nations High-Level Energy Dialogue of September 2021 called for a substantial increase of renewable energy sources' share in the global energy mix. This is necessary for near-term emissions cuts, and obviously essential in order to reach a decarbonized global energy system by 2050. [2]

Among renewable energy sources, solar photovoltaics (PVs) have for long been a promising source of renewable energy. Solar PVs already rival fossil fuels in terms of levelized cost of electricity, and the cost per kWh is set to continue declining towards 2050. The International Renewable Energy Agency (IRENA) proposes that Solar PVs could be the second largest source of power, just behind wind power, by 2050. In their proposed scenario, solar PVs would generate 25% of total global electricity needs. However, such a scenario requires long term innovation, development and investment, in order to accelerate solar power production capability and efficiency. [3]

Current solar PVs is dominated by the so-called first generation solar cells, such as the conventional and widespread silicon wafer cells. After the establishment of conventional solar cells, it was proposed that a second generation of solar cells, employing thin film technology, would eventually come to dominate over the first generation cells [4]. The second generation offered significantly lower material costs, albeit at a lower efficiency. However, the cost of implementing first generation silicon cells has plunged downwards. Being well established in industry, the first generation will lead solar PVs in achieving near-term sustainability goals.

A third generation of solar cells was also proposed, and one concept belonging to this generation (tandem cells) was later realized commercially [4]. This generation seeks to create solar cells with efficiencies exceeding the maximum efficiency of conventional solar cells. The maximum efficiency of today's most widespread silicon solar cells is known to be around 30% at one sun concentration [5]. Several concepts have been proposed for a third generation of cells to exceed this efficiency limit, and while first generation solar PVs will dominate well into the 2030s, the third generation could be a significant contributor to a decarbonized society by 2050.

Intermediate band solar cells (IBSC) belongs to the third generation of solar PVs, and is the research backdrop of the present thesis. The IBSC is based upon having

a material with an intermediate energy band positioned in between the valence band and conduction band [6][7]. The maximum efficiency of such a cell would be approximately 49% at one sun concentration, and IBSCs could potentially give highly efficient cells with a simple design. Although proof of concept has been demonstrated, IBSCs has yet to be fully realized and implemented on a practical scale [8]. However, the concept is an exciting topic of research moving forward towards 2050.

Doping of semiconductors has been proposed as a way of realizing intermediate band (IB) materials. A specific doping strategy called *non compensated n-p codoping* of titanium dioxide (TiO_2), specifically (Cr,N) co-doping of anatase-phase TiO_2, has been proposed as a possible candidate [9]. As part of the research carried out at the Department of Physics at NTNU Trondheim, where such a candidacy is investigated, this thesis will concern characterization of undoped and doped TiO_2 thin films deposited by pulsed laser deposition. The doped samples are made through the combinatorial pulsed laser deposition method, where each film has a continuous gradient of doping concentrations and structural characteristics across the film.

Titanium dioxide is a wide band-gap semiconductor that has received widespread attention in recent decades. Since its potential for photogenerated water splitting was reported by Fujishima and Honda [10], TiO_2 has been studied for applications in photocatalysis [11], dye-sensitized solar cells [12], anti-fogging [13] and anti-bacterial surfaces [14]. It is only recently that attention has been drawn to the possibility of creating IB materials by non-compensated n-p codoping of TiO_2 [15], extending its interest into the field of intermediate band solar cells. While the latter is mostly studied by physicists, the former draw attention from applied chemistry, electrochemistry, surface engineering and environmental sciences. Because of the inter-disciplinary interest in TiO_2, a range of scientific fields may benefit from each other's results and shared knowledge base.

The objective of this thesis is thus characterization of TiO_2 thin films, with the goal of adding to the increasing knowledge base of undoped and (Cr,N)-codoped TiO_2 thin films. Conventional θ–2θ X-Ray Diffraction, thin film Grazing-Incidence X-Ray Diffraction, and thin film High Resolution X-Ray Diffraction will be applied. The results will be investigated qualitatively and quantitatively. As a complementary method, Raman spectroscopy will be used to assess the validity of the X-ray diffraction conclusions.

Outline of The Thesis

The thesis will first present the relevant theory in Section 2. This includes basic theory for XRD, Raman spectroscopy, as well as theory for TiO_2, PLD and relevant substrate materials. In Section 2.6, a brief literature study for PLD deposited TiO_2 is presented.

In Section 3, the methods employed in the data analysis of XRD and Raman spectroscopy results are presented. This also includes a description of how uncertainties and possible errors will be accounted for. Section 4 presents the experimental details, and Section 5 presents the results and discussion.

Finally, the conclusion is presented in Section 6.

2 Theory

This section will define the theoretical framework for the results of this thesis. A brief summary of the main X-ray diffraction concepts is presented, along with the basic principles of Raman spectroscopy. The section then continues with relevant theory for TiO_2 studies, pulsed laser deposition, and substrate materials described in this thesis. At the end, a summary of findings from the literature on pulsed laser deposited TiO_2 thin films wil be presented. Figures are provided by the author.

2.1 X-ray Diffraction

This section is based on Kittel [16], Cullity [17] or Klug & Alexander [18]. Citations for these works will be omitted, but references (both from new references, as well as the mentioned ones) will be included when it is appropriate. Familiarity with diffraction and basic crystallography is assumed, but short review of the fundamental concepts can be found in Appendix A.

The theory presented in this thesis will be based on the kinematical theory of diffraction, which assumes only a single scattering event for each photon [17], as opposed to the dynamical theory which accounts for multiple scattering events. For nano-scale materials, like the films presented in this work, the kinematical theory is expected to be sufficient. Note that effects of dynamical scattering will be observed from some of the substrates presented.

2.1.1 Bragg's Law and The Laue Condition

In real space, for a set of crystal planes (hkl), the condition for diffraction of photons to occur is understood through Bragg's law:

$$n\lambda = 2d \sin\theta \tag{1}$$

where d is the distance between parallel atomic planes, λ is the wavelength of the incident photons, n is the order of diffraction and θ is the angle of incidence. Note that this assumes monochromatic radiation. In this work, the notation (hkl) will refer to all planes related by symmetry (e.g. (100), (010), (001) and so on for a simple cubic crystal). When waves are incident on a material, then at any angle for which equation (1) is satisfied, constructive interference will occur between outgoing waves, and a diffraction peak will be measured at an angle 2θ to the incident wave. The Bragg condition is illustrated in Figure 1.

In reciprocal space, diffraction occurs when the Laue condition is satisfied:

$$\mathbf{k} = \mathbf{k}_{\text{out}} - \mathbf{k}_{\text{in}} = \mathbf{G}, \tag{2}$$

where $\mathbf{k}$ is called the scattering vector, $\mathbf{k}_{\text{in}}$ and $\mathbf{k}_{\text{out}}$ are the incoming and outgoing

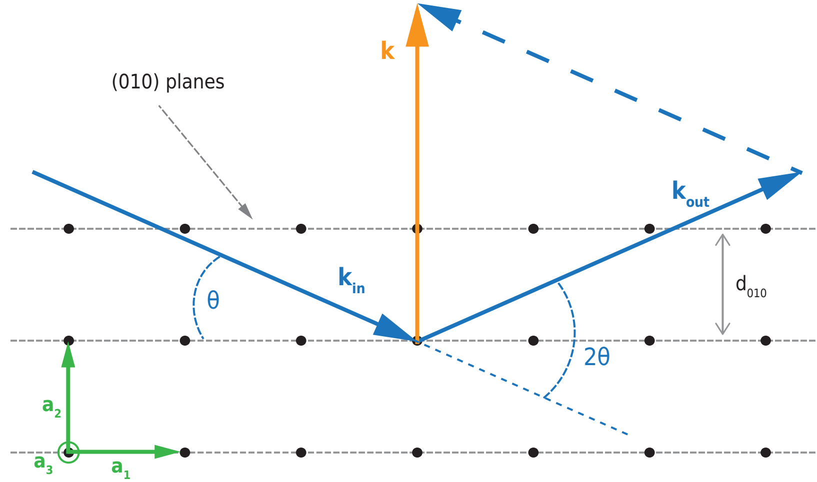

Figure 1: Schematic illustration of the Bragg condition, for crystal diffraction from the (010) planes of a single crystal. Green arrows indicate the crystal lattice translation vectors. Blue arrows indicate the wave vectors for the incoming and outgoing photons with wavelengths λ. Orange arrow indicates the scattering vector of eq. 2. Whenever θ satisfies eq. 1, there will be constructive interference between photons scattered from the (010) planes.

wavevectors, and $\mathbf{G}$ is a reciprocal lattice vector. In other words, when waves are incident on a crystal, diffraction will occur whenever the scattering vector is equal to a vector of the crystal's reciprocal lattice. The Laue condition is illustrated in Figure 2.

Effectively, when performing XRD measurements one scans parts of the 3D reciprocal space with the variable vector $\mathbf{k}$. Whenever $\mathbf{k}$ passes through a reciprocal lattice point, diffraction is detected. In this thesis, $\mathbf{k}$ will always move within a plane, and hence the reciprocal space will be illustrated in two dimensions, as in Figure 2.

The direction and magnitude of $\mathbf{k}$, and hence which diffraction peaks will be measured, depend on the measurement technique that is utilized. The next two sections will explain some consequences of this.

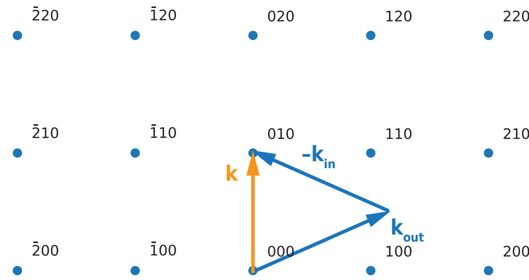

Figure 2: Illustration of the Laue condition in reciprocal space. The wave vectors are equivalent to those of Figure 1.

2.1.2 Un-textured, Textured and Single Crystal–Like Materials

While the reciprocal space for an ideal single crystal consists of small, single spots like in Figure 2, the situation can be quite different for polycrystalline materials. Consider Figure 3, which displays three variations of polycrystalline materials. In Fig. 3 (a), the crystallite grains are randomly oriented, so that instead of reciprocal lattice *points*, each family of planes is represented by a *ring*, since every spot is effectively rotated about all angles. Such a sample will be referred to as "un-textured".

In Fig. 3 (b), the crystallite sizes are similar to those of (a), but now the material is *textured*. The grains are all oriented in a similar direction, with only a slight variation in orientations, i.e. *mosaicity*. Such a material would be called textured, polycrystalline with a certain (hkl) preferred orientation. In reciprocal space, each family of planes is represented by a finite arc. The length of the arc reveals the material's mosaic spread.

In Fig. 3 (c), the grains are considerably large, with only a tiny mosaic spread. Such a material would be called single crystal–like. Exactly at what point a material is denoted textured vs. single crystal–like is somewhat arbitrary. In this thesis the term *highly textured* will usually be applied for materials in between textured and single crystal–like.

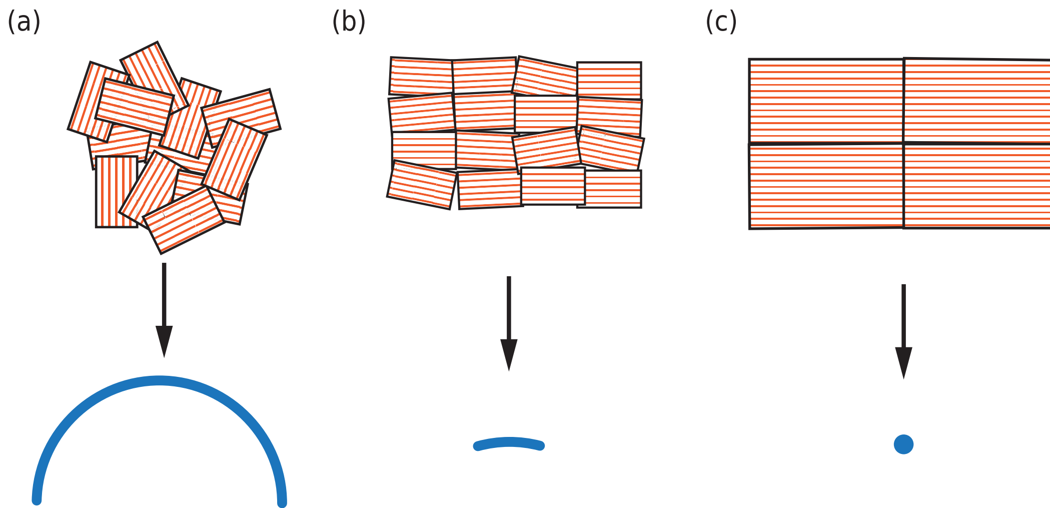

Figure 3: Real space and reciprocal space for: (a) An un-textured polycrystalline aggregate. The crystallites (black boxes) are randomly oriented, so that a family of planes (orange lines) is represented by a uniform ring in reciprocal space; (b) A polycrystalline but *textured* material, in which the crystallites all have a similar orientation, but with some *mosaicity* (small variation in orientations). This results in each family of planes being represented by a small arc in reciprocal space; (c) A single crystal–like material, in which the crystallites are large, although some small mosaicity may be present. This results in single spots for each family of planes in reciprocal space. A near-perfect crystal would consist of very large crystallites.

2.1.3 XRD Measurement Configurations

There are several measurement techniques which fall under the term "XRD". In this thesis, the different techniques will be referred to as different *scans* or *configurations*. The information extracted, as well as applications and limitations, vary between configurations. An understanding of the most widespread techniques is essential to understand the results presented in this work.

θ–2θ scan: One of the most utilized configurations in XRD is the θ–2θ scan. The technique is also referred to as "Bragg-Brentano geometry", a "coupled scan" or just "powder XRD" [19]. The θ–2θ scan is defined by a fixed relation between the X-ray source and the detector. Whenever the source is moved to an angle θ with respect to the sample surface, the detector is moved to 2θ with respect to the incident beam. This ensures that the scattering vector $\mathbf{k}$ maintains a fixed direction in reciprocal space, while its magnitude increases with θ. Figure 4 (a) shows the trajectory in reciprocal space (orange curve) for a (010)-oriented simple cubic (single) crystal. The blue dots indicate points on the reciprocal lattice. Note that for θ–2θ scans of single crystals, only one family of planes will be detected. A simulated diffractogram from a single crystal based on Fig. 4 (a) is shown in Figure 5.

For a *polycrystalline material*, the θ–2θ diffractogram will generally be different from a single crystal. For *randomly oriented* grains, each point on the reciprocal lattice will be represented by a uniform *ring* in reciprocal space. A representation of this can be seen from the blue arcs in Fig. 4 (b). In a randomly oriented, polycrystalline aggregate, *all* families of planes will be detected. This scenario is often called a "powder diffractogram". The powder diffractogram of a material with simple cubic structure is shown in Figure 6.

The application of θ-2θ to powders or polycrystalline aggregates is in fact a discipline in itself [18]. A polycrystalline material of a certain phase ("phase" will in this thesis be used to distinguish both materials of different chemical compositions,

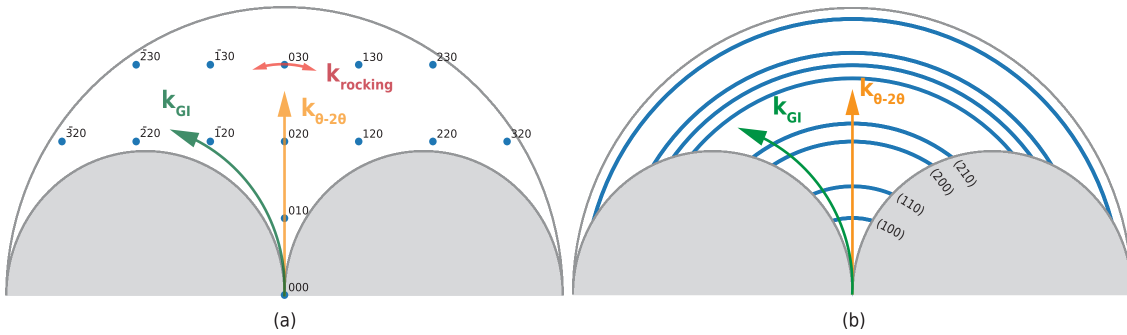

Figure 4: Schematic drawing illustrating trajectories traced out in reciprocal space when performing three different XRD scan configurations; (a) Trajectories of a θ–2θ scan (orange), grazing-incidence (GI) scan (green) and rocking curve (red) for a single crystal; (b) θ–2θ and GI configurations for a polycrystalline material with random orientations. Each ring in (b) corresponds to a family of planes related by symmetry. Gray areas correspond to negative angles of incidence, or no reflection.

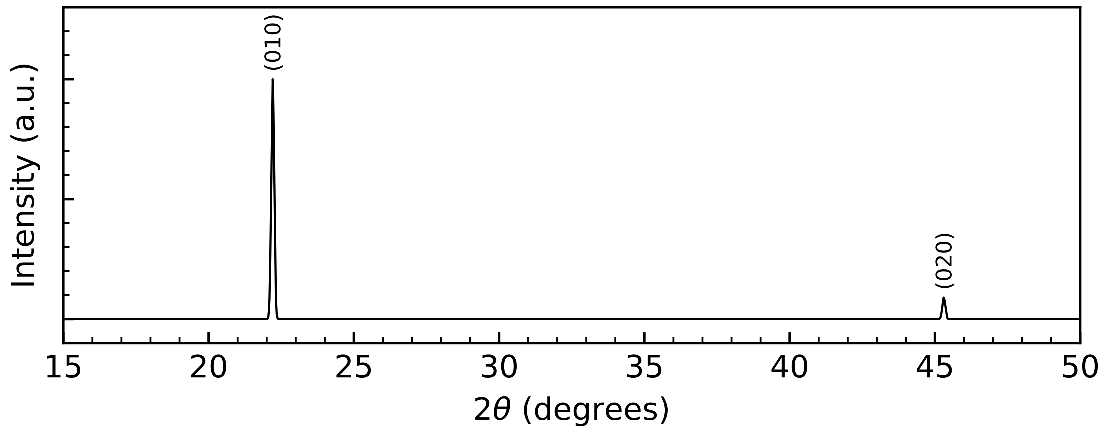

Figure 5: A simulated θ–2θ scan from a single crystal with the simple cubic structure, the the (010) planes being oriented paralell to the surface. The diffractogram is what would be measured based on the θ–2θ trajectory in Fig. 4 (a).

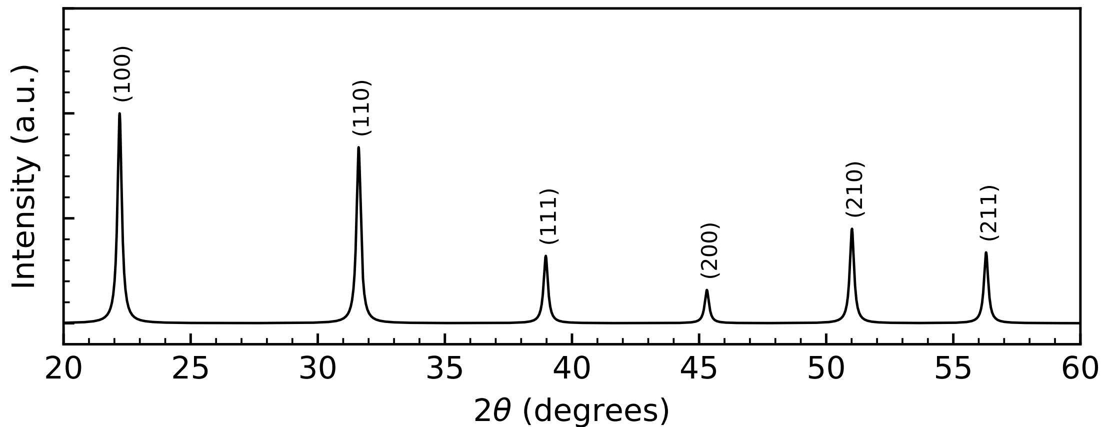

Figure 6: Simulated θ–2θ scan from a polycrystalline aggregate of a simple cubic material. This is the diffractogram which would result from the trajectories of Fig. 4 (b).

as well as different polymorphs of the same material) will produce a distinct fingerprint in θ-2θ XRD, allowing for effective qualitative (and also quantitative, to be discussed in Section 3.2.5) phase identification. Certain planes will diffract X-rays more effectively than others, meaning that there is an intrinsic relation between the intensities of different reflections. When the grains of a material are randomly oriented, all reflections will be measured, and the intensities of the peaks will correspond to the intrinsic relative intensities of the material (dictated by the structure factor [16]). Qualitative phase analysis is then possible by comparing the positions and intensities of an XRD pattern to reference or theoretical values. This is an extensively used method for phase identification in materials [17][18].

Grazing-incidence X-ray diffraction (GIXRD): In the grazing-incidence (GI) configuration, θ is kept at a fixed, low angle of incidence, while the detector rotates about the sample [20]. The technique sometimes goes by the name glancing-angle

XRD, but here the GIXRD term will be used. The measured angle is still labeled 2θ, but the direction and magnitude of $\mathbf{k}$ now changes as the detector rotates. The scattering vector thus traces out a curve in reciprocal space. As seen in Figure 4 (a) and (b), for a single crystal, GIXRD runs the risk of entirely missing any spots, whereas for a randomly oriented polycrystalline sample, the result will be similar to the θ-2θ scan.

The GI scan is commonly used for thin film analysis. Because of the low angle of incidence, GIXRD allows for low penetration depths [19]. This in turn allows for a stronger film signal, as absorption of the incident X-rays is limited, and undesirable substrate artifacts can be avoided.

Rocking curve: A third configuration of XRD is the so called omega scan, or "rocking curve" [17], illustrated by the red arrow in Fig. 4 (a). In this configuration, the source and detector are rotated about the sample in a fixed manner, so that the relative angle between the source and detector remains the same. In practice, this is equivalent to keeping the source and detector still, while the sample is tilted or "rocked". Although the angle of incidence changes, 2θ remains the same, and in the reciprocal space, $\mathbf{k}$ maintains a constant magnitude while changing its direction. The rocking curve is usually used for characterization of single crystals or epitaxial layers.

The rocking curve reveals the distribution of orientations for the grains in a sample. Such a spread could come from mosaicity in a nearly perfect (high long range order) crystal. It could also come from a polycrystalline aggregate which is highly *textured* (a term that will be defined in Section 3.2.4). In any case, the rocking curve gives a measure of the degree of crystal perfection in the sample: a near perfect crystal will have a narrow rocking curve, whereas a polycrystalline but textured material will have a wider rocking curve distribution.

High Resolution X-Ray Diffraction (HRXRD): HRXRD is in itself not a unique configuration, but is a widely used term so that an explanation is in order. In HRXRD, the use of a monochromator is essential, as well as a more careful alignment of the sample. In this work, HRXRD will be used for rocking curve measurements and θ–2θ scans, which from now on will be referred to as ω–2θ scans in the context of HRXRD, in order to distinguish them from the "ordinary" θ–2θ scans. A detailed explanation of the HRXRD procedure will be given in Section 4.

2.2 Raman Spectroscopy

Raman spectroscopy is a spectroscopic characterization technique widely used for chemical analysis of materials. A short but comprehensive review can be found in [21]. The technique is based on inelastic scattering of photons, also called Raman scattering, where the scattered photons are shifted in frequency due to interaction with the vibrational modes of the measured sample. Raman spectroscopy is mostly used as a qualitative method, and will in this work be used exclusively as a qualitative complementary method to XRD.

In Raman spectroscopy, a sample is illuminated using monochromatic light (typically a laser). The scattered light is then measured using a spectrometer, and the spectrum is represented by counting the amount of photons shifted by each wavenumber (cm^{-1}) in the measured range. Here, only *positive shifts* in wavenumber, denoted "Raman shift", will be considered.

In crystals, the vibrational modes causing Raman scattering are associated with lattice vibrations, i.e. creation and annihilation of phonons [16]. The Raman spectrum for a crystalline material will therefore be determined by the crystal structure and symmetry, as well as the chemical composition of the material. By comparing a measured spectrum to known Raman spectra, similar to in XRD, phases can be identified within the sample. Examples of Raman spectra from TiO_2 will be presented in Section 2.3.3.

2.3 Titanium Dioxide (TiO_2)

Titanium dioxide (titania, TiO_2) is a transition metal oxide that has been extensively studied for several decades. In particular, since Fujishima and Honda reported its ability for photoinduced water-splitting [10], TiO_2 has been studied as one of the most promising photocatalysts [11].

TiO_2 has three primary, naturally occuring polymorphs: rutile, anatase and brookite [22]. The crystal structure, lattice constants and space groups are displayed in Table 1, and the unit cell of each polymorph are shown in Figure 7. Brookite is highly unstable and not expected to be found in any of the studied samples in this thesis, so no further attention will be paid to this polymorph.

Rutile is the most common and most stable polymorph, and for a long time it was the only one extensively studied. However, as interest in TiO_2 has grown, more attention has been drawn to other phases. Tang et al. reported on the electronic and optical properties of anatase thin films in 1993 [23], and extensive theoretical studies on anatase and other phases have been recently carried out, as by De Angelis et al. in 2014 [24]. In most studies, great emphasis is put on the wide and interdisciplinary interest in TiO_2.

The band gaps of bulk rutile and anatase are experimentally observed to be 3.0 eV and 3.2 eV, respectively, at room temperature [25].

Table 1: Crystallographic parameters of the three main TiO_2 polymorphs. From refs. [26] and [27].

	Rutile [26]	**Anatase** [26]	**Brookite** [27]
Crystal structure	Tetragonal	Tetragonal	Orthorhombic
Lattice constants (Å)	a = 4.5937	a = 3.7845	a = 9.1840
	c = 2.9587	c = 9.5143	b = 5.4470
			c = 5.1450
Space group	$P4_2/mnm$	$I4_1/amd$	$Pbca$

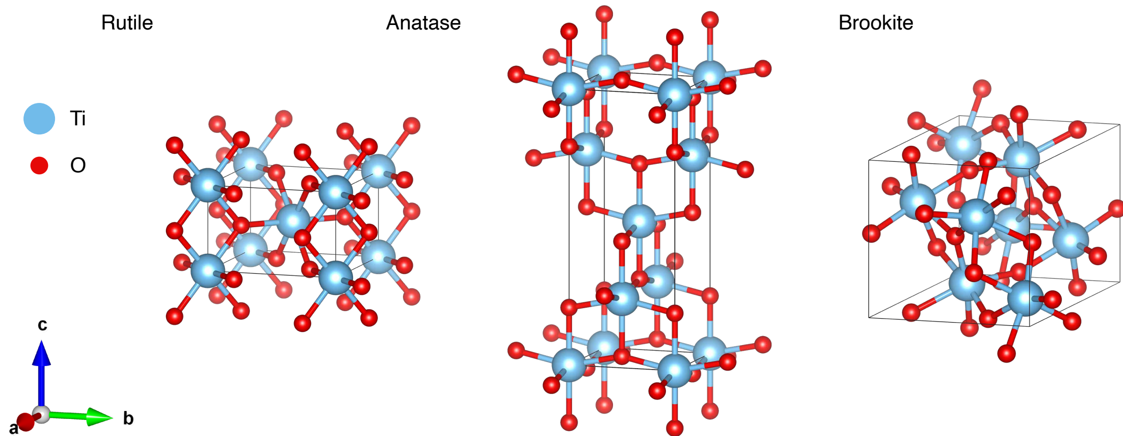

Figure 7: Unit cells of the three main TiO_2 polymorphs, made using VESTA [28].

2.3.1 The Anatase–to–Rutile Phase Transformation

It is well known that, in air, anatase transforms irreversibly to rutile at temperatures exceeding $\sim$ 600 °C [22]. Furthermore, rutile (100) planes may nucleate at twin interfaces of (112) anatase planes. This results in the rutile (100) planes lying parallel to the anatase (112) planes. The anatase phase is also known to have lower surface energies than rutile, and thus the anatase phase may be preferred for nano-sized grains [22][29].

2.3.2 XRD Characteristics of Rutile and Anatase

Owing to their different crystal structures, rutile and anatase are easily distinguishable in XRD. The powder XRD patterns from the parameters of Table 1 were calculated using VESTA [28], and are shown in Figure 8. The precise values for the 2θ angles and relative intensities of peaks are displayed in tables 2 and 3 for rutile and anatase, respectively, along with the calculated d-spacings for each plane. Only the range $2\theta < 60°$ is given, as the data in this thesis will mostly focus on this range.

As can be seen from Figure 8, the XRD patterns of powder–like rutile and anatase are dissimilar. The various diffraction peaks are denoted R (hkl) and A (hkl) for rutile and anatase, respectively. (hkl) refers to the peak coming from the (hkl) family of planes, and this notation will be used throughout this thesis.

No peak positions in Figure 12 match exactly, and the overall patterns are substantially different. The A (101) and R (110) reflections, the most intense powder XRD peaks, will be referred to as the "characteristic" peaks, because in an un-textured sample with randomly oriented grains, these peaks would be the most obvious indicators of the presence of rutile or anatase in a sample.

Table 2: The calculated (hkl) reflections from an un-textured rutile sample, based on the lattice constants in Table 1.

Reflection	d_{hkl} (Å)	2θ (°)	Rel. intensity
R (110)	3.25	27.44	100.00
R (101)	2.49	36.08	46.7856
R (200)	2.30	39.19	7.18
R (111)	2.19	41.24	18.90
R (210)	2.05	44.04	6.77
R (211)	1.69	54.32	52.27
R (220)	1.62	56.63	17.74

Table 3: The calculated (hkl) reflections from a powder anatase samples, based on the lattice constants in Table 1.

Reflection	d_{hkl} (Å)	2θ (°)	Rel. intensity
A (101)	3.52	25.31	100.00
A (103)	2.43	36.95	6.55
A (004)	2.38	37.79	20.71
A (112)	2.33	38.57	7.59
A (200)	1.89	48.04	29.60
A (105)	1.70	53.89	19.24
A (211)	1.67	55.07	18.87

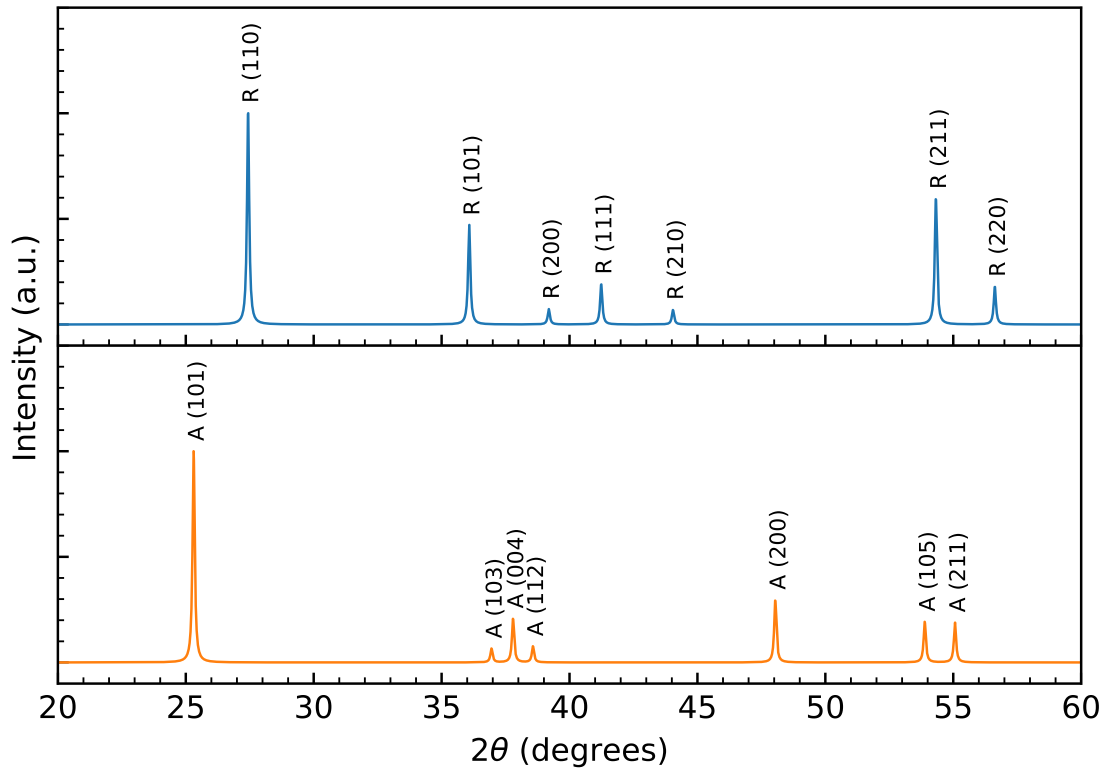

Figure 8: Simulated powder XRD patterns of (top) rutile and (bottom) anatase in the 2θ range $(20°, 60°)$. The intensities and position are the same as in tables 2 and 3, with the various (hkl) plane families indicated.

2.3.3 Raman Spectra of TiO_2

Both rutile and anatase have well documented Raman spectra [30]. The spectra agree with the predictions stemming from group theory, but there is some variation of measured values in literature. The variations, however, arise from small experimental differences, and are generally insignificant. Reference TiO_2 spectra for this thesis are taken from the RRUFF database [31], and are displayed in Figure 9.

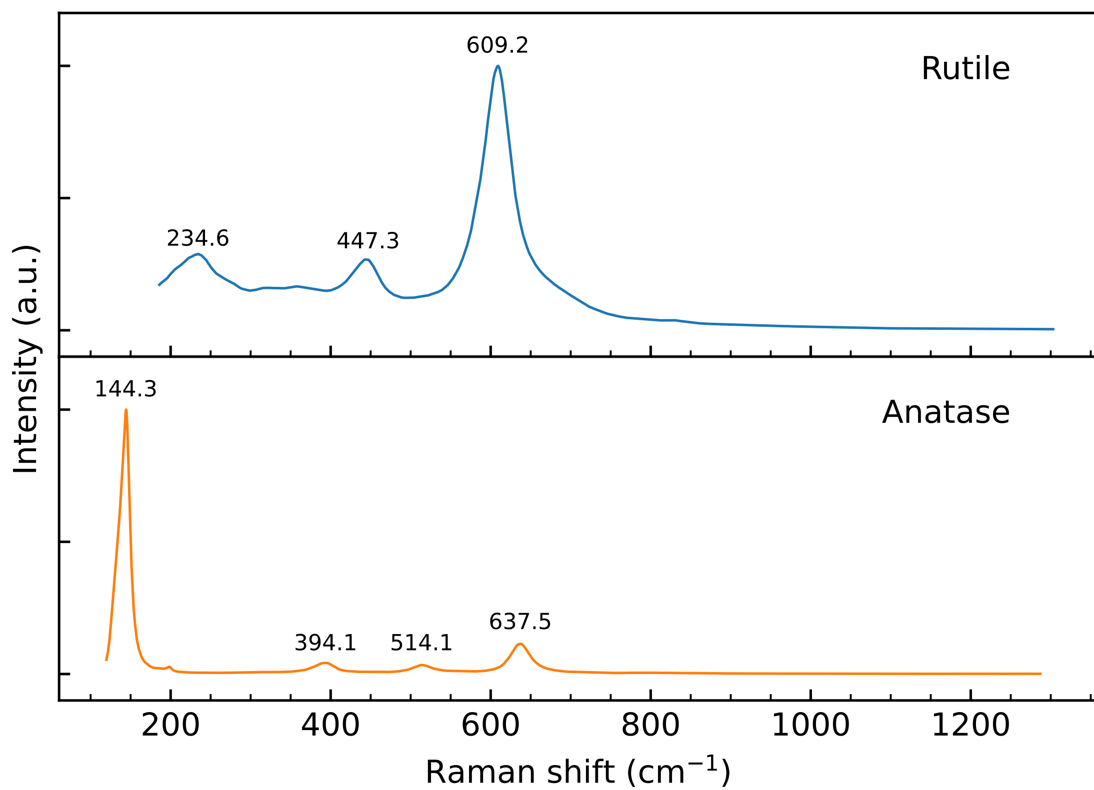

Figure 9: Reference Raman spectra for (top) rutile and (bottom) anatase [31]. The Raman shift positions for each peak are annotated.

2.4 Pulsed Laser Deposition

Pulsed laser deposition (PLD) is a thin film deposition technique, widely used in research and applications [32]. The process begins with focusing a pulsed laser onto a material, called the *target*. For a sufficient laser power density, the material from the target is ejected in the form of a plasma *plume*. Matter from the plume then condenses on a selected substrate. The plume is *non-uniform*, and matter thus condenses around a *plume center*. The plume density and kinetic energy of ablated species typically decrease away from the plume center [33]. Typical deposition rate is on the order of less than one to several nm per pulse.

Both the target and substrate are placed in a vacuum chamber. A passive or reactive gas may be supplemented during the deposition, which may or may not react with the plasma plume or surface deposition. This could for instance be molecular oxygen for the deposition of oxides [32]. An illustration of a PLD procedure, using a theoretical target "XZ_2", combined with reactive, molecular gas "Z_2", resulting in a deposited XZ_2 film, is shown in Figure 10.

Several parameters may be varied during deposition. The relevant parameters for the present work is the laser fluence (J/cm^2), the deposition pressure P_{dep} (mbar), oxygen, argon and nitrogen gas flow (sccm), as well as substrate temperature T_s.

PLD offers several advantages in thin film growth. The ability to transfer stoichiometry of even complex structures from the target to film is an often reported advantage [32]. Moreover, the pulsed nature of the laser allows for precise control of the growth rate.

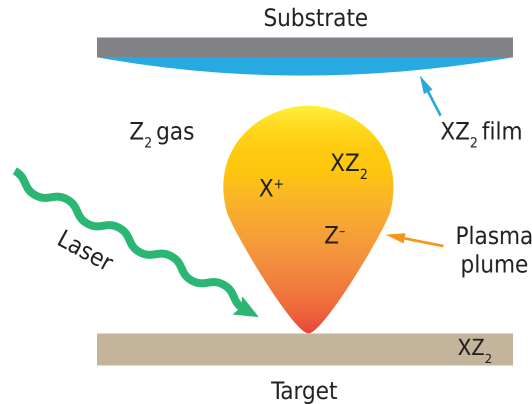

Figure 10: Illustration of a pulsed laser deposition procedure. A bulk target consisting of material "XZ_2" is ablated by an incident laser. A variety of species, such as X^+ or Z^- ions, or XZ_2 molecules, may be ejected from the target in a plasma plume. The species then condense on the substrate, possibly reacting with Z_2 molecules, to form an XZ_2 film. Note that this illustrates reactive PLD, but other variations exist. One could for instance ablate an XZ_2 target in an inert gas environment.

2.4.1 Combinatorial PLD

Combinatorial PLD is a deposition method where the non-uniformity of the plasma plume is exploited to produce a certain concentration and/or thickness gradient across the film. A key aspect lies in using multiple targets of different materials to expose the substrate to multiple, differing plumes. In this work, only two targets have been used to build up the deposited films, and the following explanation of combinatorial PLD will therefore focus on the two-target case.

The concept of combinatorial PLD with two targets is illustrated in Figure 11. The two targets consist of materials "1" and "2", respectively. First, Target 1 is ablated at a certain distance from the wafer center. This plume location will be referred to as the "first plume center" or "plume center one". Because of the non-uniformity of the plume, this deposits material 1 onto the substrate with a certain concentration gradient.

Next, Target 2 is ablated at a different position with respect to the wafer center; "plume center two". Thus, material 2 is deposited onto the film with a certain concentration gradient. Repetition of ablation with targets 1 and 2 leads to deposition of a layered film where concentration gradients of the respective materials lie parallel to the substrate surface.

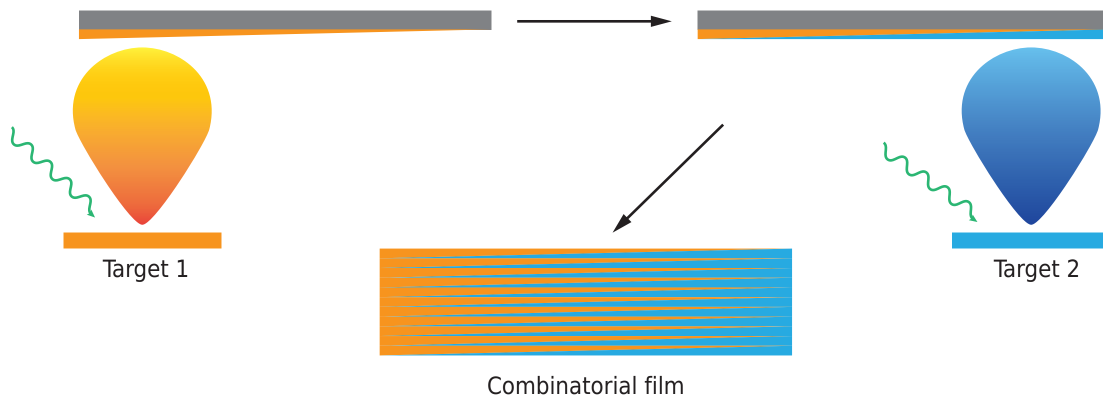

Figure 11: Schematic illustration of a combinatorial PLD procedure. Two targets of different materials are ablated at two different positions on the substrate (plume centers), resulting in a film with a concentration gradient between the two plume center positions. Note that the substrate is not rotated during the deposition of material.

2.4.2 Epitaxial Film Growth

Some of the thin films studied in this work are expected to have a certain growth relationship with their respective substrates. The terminology of *epitaxy* will therefore be used, although true epitaxial growth is not necessarily expected for any of the samples. The theory of this chapter is mainly drawn from *Materials Science of Thin Films* by Ohring. A deeper review of the concept of epitaxy with references may be found there. [34]

Epitaxy in film growth refers to the growth of one or more well-defined orientations of a crystal with respect to a crystalline substrate. The substrate thus acts as a seed for the epitaxial film. There are several manifestations of epitaxy, the two most basic of which are:

- *Homoepitaxy*: The substrate and deposited film are of the same material.
- *Heteroepitaxy*: The substrate and deposited film are of different materials.

In homoepitaxy, perfect alignment of the lattices is possible. In heteroepitaxial growth, however, there will typically be some mismatch in the lattice parameters. Three further forms of epitaxy are thus defined:

- *Lattice matched epitaxy*: The lattice constants of the film and substrate are nearly or perfectly identical.
- *Strained epitaxy*: The film lattice parameters are altered so as to match the substrate lattice. The film is thus strained and remains strained as it grows.
- *Relaxed epitaxy*: Dislocations are present at the film-substrate interface. The film lattice maintains its intrinsic lattice parameters away from the interface.

When the film is strained so as to match the substrate lattice, the film is said to grow *pseudomorphically.* An early theory developed by Frank and van der Merwe predicted that a lattice mismatch below 9% would lead to pseudomorphic growth [35]. Generally, strained epitaxy prevails in the early stages of film growth [34]. Pseudomorphic growth is exptected up to a critical film thickness d_c, at which the strain energy exceeds the energy of a relaxed structure. Beyond this film thickness, dislocations are expected to be introduced.

2.4.3 Growth Mechanics

The characterization techniques used in this thesis offer a broad picture on the long-range nature of the samples. However, the short-range(nano-scale) information that can be extracted is generally limited. Because of this, growth mechanics during PLD will not be discussed in detail in this thesis. However, a short description of the most important aspects, and the terms used, for deposition are presented:

The actual deposition is conventionally explained as occuring in six steps, as in ref. [36]. These steps are described in terms of (1) adsorption of the plasma plume species, (2) diffusion of adatoms before (3) reaction of adsorbed species, including both reaction with the surface and other adatoms. The initial aggregation of the film material is called (4) nucleation. Further on, the film (5) develops a structure as it grows thicker. The term "structure" in this case encompasses everything from amorphous to single crystal materials. (6) Finally, diffusional interactions may occur, including within the film and between the film and substrate.

For a more detailed investigation of growth mechanics, see Rosnes [37], where a sample similar to CCS-Si-Cap (to be presented in Section 5.6.4) was investigated by Transmission Electron Microscopy.

2.4.4 Preferred Orientation of Pulsed Laser Deposited Films

It is well established that during growth of crystalline thin films, a preferred orientation may develop among the grains, with respect to the substrate plane. This may happen even though the growth occurs on an amorphous surface [38]. The physical origins for the resulting preferred orientation vary.

Already in 1967, van der Drift proposed an "evolutionary selection" model for development of a preferred orientation in thin film deposition [39]. In the case that the vertical growth rates of crystal grains depend on orientation, van der Drift proposed that "survival of the fastest" would allow the orientation with the fastest growth rate to dominate as a film grows thicker. A consequence of this is that the degree of preferred orientation increases during vertical growth of the film. The model predicts the development of a preferred orientation, even starting from randomly oriented nuclei.

Preferred orientations will be investigated for the samples presented in this thesis.

2.5 Substrate Materials

The TiO_2 films studied in this work are simultaneously deposited on four different substrates: Si (100) [40], $LaAlO_3$ (001) [41], $SrTiO_3$ (001) [41] and Al_2O_3 [42] (0001). A brief summary of their relevant properties are given in Table 4.

Silicon: Silicon (Si) is widely used as a substrate for a vast range of crystal growth and film deposition methods. In this thesis, the silicon substrates used were not etched, and an amorphous SiO_2 layer was present on all the substrates. Note therefore that the silicon substrates will be regarded as amorphous substrates in the discussion of results.

$LaAlO_3$: Lanthanium aluminate (LAO) is a perovskite that is frequently observed in either rhombohedral or pseudo-cubic form. The substrates considered in the present work are pseudo-cubic and (001)-oriented, as confirmed by the XRD data, and so only the pseudo-cubic crystal structure will be presented here as a reference. LAO has the potential of lattice matching with anatase to approximately 0.15% if the anatase crystallizes with the (001) planes parallel to the LAO (001) planes. One might therefore expect that deposition of TiO_2 onto a (001) LAO will yield pseudomorphic growth of (001)-oriented anatase. This would manifest itself in θ–2θ XRD by showing a prominent A (004) peak.

LAO is known to form twin structures, resulting in "jagged" substrate surfaces. The details of this will not be discussed, but the twin domains will be seen in the rocking curves of the films on LAO substrates.

$SrTiO_3$: Strontium titanate (STO) is a cubic perovskite. The substrates used in this work are (001) oriented. STO (001) has a lattice mismatch of 3.18% with (001) oriented anatase. Pseudomorphic growth is therefore expected for deposition on these substrates. Similar to LAO, this would yield a strong A (004) peak in θ–2θ XRD.

Al_2O_3: Sapphire (Sap) is a variety of the mineral corundum. In this thesis, the sapphire substrates used are (0001) oriented (note the use of hexagonal index system). The lowest lattice mismatch between sapphire and TiO_2 is 3.58% for (100) oriented rutile. Pseudomorphic growth might therefore be expected, and in θ–2θ XRD this would result in a strong R (200) peak.

Table 4: Relevant crystallographic information for the substrates used in this thesis. Lattice mismatch denotes the lowest lattice mismatch with TiO_2, given by the orientation relationship column. [40][41][42]

Substrate	**Crystal structure**	**Lattice constants (Å)**	**Lattice mismatch**	**Orientation relationship**
Si (100)	Diamond cubic	a = 5.431	N/A	N/A
$LaAlO_3$ (001)	Pseudo-cubic perovskite	a = 3.790	0.15%	A (001) ‖ LAO (001), A [100] ‖ LAO [100]
$SrTiO_3$ (100)	Cubic perovskite	a = 3.905	3.18%	A (001) ‖ STO (001), A [100] ‖ STO [100]
Al_2O_3 (0001)	Hexagonal	a = 4.758 c = 12.992	3.58%	R (100) ‖ Sap (0001), R [001] ‖ Sap [1010]

2.6 Pulsed Laser Deposition of TiO_2 Thin Films

PLD, when used for TiO_2 thin film deposition, allows for tuning the resulting structure of the film by varying deposition parameters. It is reported in literature (to be presented below) that choice of reactive gas, gas pressure, substrate temperature, substrate material and laser fluence all affect the crystallinity of the thin films when one is varied, and other parameters remain unchanged.

Ref. [43] studied TiO_2 growth on Si (100) substrates by XRD and Raman spectroscopy. It was suggested that increasingly pure (001)-oriented anatase was achieved by increasing substrate temperatures from 350 °C to 800 °C, with pure oxygen gas at 5×10^{-2} mbar (given as 5 Pa in the article). At lower temperatures, some (101)-oriented anatase was also observed. The occurence of these orientations were attributed to them being "flat faces", so that these growth directions were favorable. Furthermore, the study claimed that because the Ti-O bond length is longest along the (001)-direction—corresponding to smallest bond energy—this direction is favored as temperature is increased. For substrate temperature 800 °C, the rutile phase was also observed. This was attributed to a phase transformation of anatase to rutile TiO_2 at higher temperatures. It will be seen that other literature, as well as the results of this thesis, agree with the above discussion.

Ref. [43] also studied the effects of ambient gas pressure. Keeping the substrate temperature at 500 °C while increasing oxygen pressure, it was observed that an oxygen pressure of 5×10^{-4} mbar favored growth of rutile, 5×10^{-3} mbar and 5×10^{-4} mbar favored anatase, whilst a high pressure of 3×10^{-1} mbar resulted in an amorphous film. The latter result was attributed to the high pressure preventing the target plasma from reaching the substrate. Moreover, it was observed that under pure argon pressure, varying the laser fluence could yield either a polycrystalline rutile-anatase mix or textured rutile, for high and low fluences respectively, at substrate temperature 750 °C.

Another study went more in depth on the effect on laser fluence when depositing on a Si (100) substrate [44]. At a substrate temperature of 650 °C and 5×10^{-2} mbar oxygen pressure, anatase and rutile were both observed, but the ratio (as seen in XRD) strongly depended on the laser fluence. For an oxygen pressure of 5×10^{-4} mbar, only rutile was observed, in agreement with ref. [43], though the latter used a lower laser fluence.

A study was carried out on TiO_2 deposited by reactive PLD on a Si (100) substrate using a metallic Ti-target [45]. The formation of TiO_2 thus depended on the Ti plasma reacting with the pure oxygen gas. Using XRD and Raman sepctroscopy, it was concluded that an oxygen pressure of 1×10^{-1} mbar yielded anatase phase films, whilst pressures of 1×10^{-3} and 1×10^{-4} mbar gave rutile phase films. The difference was attributed to a decrease in kinetic energy of laser evaporated species for lower pressures. The decrease in kinetic energy was then attributed to anatase growth, by noting that anatase is more stable at lower temperatures.

A wide range of literature exists for deposition of TiO_2 on other substrates. A study of deposition on a glass substrate reported growth of mainly anatase films for

temperatures below 700 °C, noting the appearance of rutile at 700 °C [46].

In a study of TiO_2 growth on $SrTiO_3$ (STO), pure (001)-anatase films were obtained even for very high temperatures [47]. It was observed through XRD that although the substrate temperature was increased from 200 to 1000 °C, far above the limit of thermodynamic stability for anatase, only (001)-oriented anatase was detected. The films deposited at the highest temperatures also gave the sharpest XRD peaks. The results were attributed to a low lattice mismatch ($\sim 3\%$) between the anatase (001) and STO (100) surfaces, and it was concluded that the substrate could stabilize the anatase film even for highly unfavorable temperatures.

Several studies have also been conducted for deposition of TiO_2 on $LaAlO_3$ (LAO) (001) substrates. LAO (001) is expected to favor growth anatase (001), owing to the small lattice mismatch ($< 1\%$) between the two materials. One study of pulsed laser deposited TiO_2 on LAO (001) reported epitaxial growth of anatase (001), where the epitaxial quality was fine-tuned by varying deposition parameters [48]. In general, substrate temperatures of ~ 680 °C, oxygen pressure of $\sim 5\times10^{-4}$ mbar, laser fluence ~ 44 mJ and laser pulse frequency ~ 5 Hz yielded epitaxial anatase (001) growth.

Several studies have reported epitaxial growth of TiO_2 on STO (001), LAO (001) and sapphire (0001) by PLD. One such study [49] found that growth on STO (001) and LAO (001) substrates resulted in anatase (001) films, while sapphire (0001) resulted in rutile (100) films. A similar study reported the similar results [50]. In both cases, the epitaxial growth was attributed to the low mismatch between deposited TiO_2 films and substrates.

3 Data Analysis

This section will present the methods used for the data analysis employed in this thesis.

3.1 Qualitative XRD Analysis

3.1.1 Phase Identification

XRD is a widely used technique for phase identification of materials [17][18]. The basis for this is the fact that a given crystalline substance always produces a characteristic diffraction pattern, regardless of whether the substance appears in pure form or as a mixture of substances [17]. By comparing the diffractogram of a sample to the powder XRD pattern (calculated or experimental) of a certain material, it can be assessed whether or not that material is found in the sample.

The technique is most effective when applied to powdered samples with randomly orientated grains. For such a sample, the XRD diffractogram from θ–2θ is expected to closely resemble the powder XRD pattern(s) of its constituent phase(s). Phase identification is then assessed by comparing the relative positions and relative intensities to the ideal powder XRD pattern of a candidate phase. A simulated example for a polycrystalline aggregate of rutile is shown in Figure 12.

As seen in Figure 12, there is a strong agreement between the positions and relative intensities of the diffractogram and rutile powder XRD pattern. This would indicate that the sample consists solely of randomly oriented rutile grains.

Note that the simulated θ–2θ pattern of Figure 12 would be nearly identical in the GIXRD configuration, as illustrated in Fig. 4 (b).

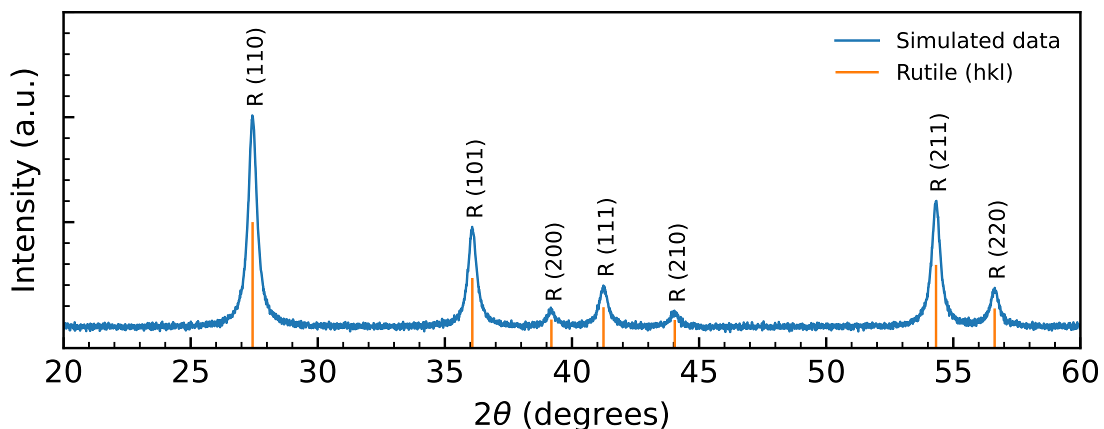

Figure 12: A simulated XRD diffractogram from a polycrystalline aggregate of rutile. The rutile peaks are modeled as Lorentzian functions, with Gaussian noise added to the entire data set. The rutile (hkl) lines corresond to the intensities of the calculated rutile powder XRD pattern of Figure 8 and Table 2.

While phase identification is simple for highly powder–like (samples resembling powder XRD patterns in XRD) samples, it can be more difficult for samples displaying only one or a few peaks. In a *textured* sample (to be defined quantitatively in Section 3.2.4), there can be many individual grains which are all oriented in a certain way with respect to the sample surface. It is then possible that only one peak is visible. However, one can make educated guesses based on what is expected from the sample (for instance, whether one expects to find only stoichiometric TiO_2). By comparing with relevant powder XRD patterns, phase identification can still be performed, as will be illustrated by the following example.

Consider the simulated θ–2θ scan of Figure 13. The figure simulates a TiO_2 thin film (unknown phase) on an STO (100) substrate. Although only one peak is visible, the film is known to consist of stoichiometric TiO_2, and so comparison between the scan and powder XRD patterns of rutile and anatase remains useful. The only good aggrement between the data and (hkl) lines, is with that of the anatase (004) reflection. The width of the peak suggests that the film consists of small crystallites. In such a scenario, it would be strongly suggested that the film is comprised of *textured* polycrystalline anatase with the (001) planes parallel to the substrate surface.

Note that in the GIXRD configuration, the results from the simulated sample in Figure 13 would be completely different. Based on what trajectory is traced in reciprocal space (refer to Figure 4), the data might not show anything at all.

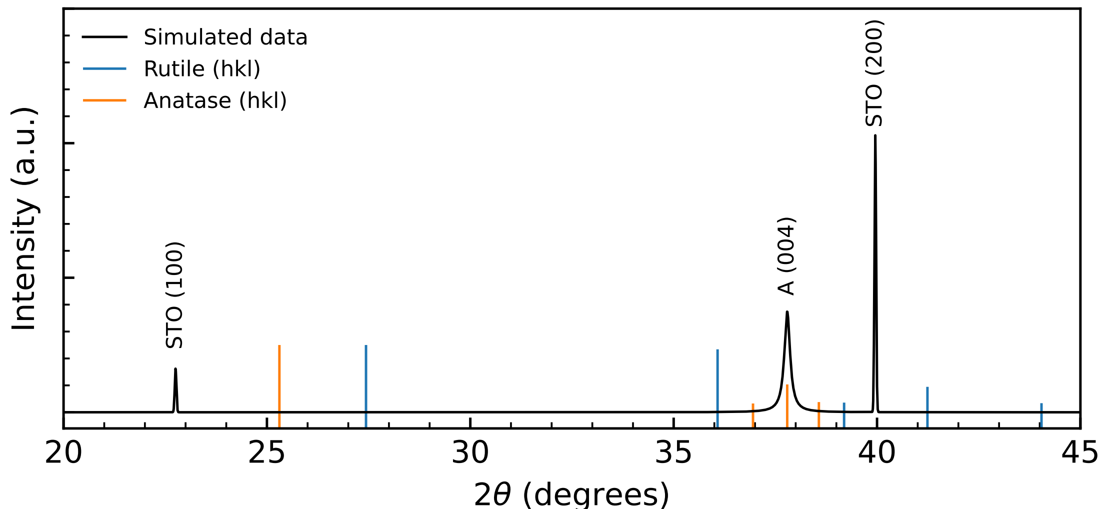

Figure 13: Simulated θ–2θ scan of a textured, polycrystalline (001)-oriented anatase film (Lorentzian function), deposited on an STO substrate (Gaussian). The rutile and anatase (hkl) lines are also included, to demonstrate how one could do phase identification based on this data by comparing peaks to reference line positions.

3.2 Quantitative XRD Analysis

3.2.1 Peak Fitting

In order to properly assess peak properties such as intensity, position and width of XRD peaks, it is important to fit the peaks with appropriate functions. This is especially important when the individual peaks in an XRD scan overlap. While a perfect but finite crystal would give off a Gaussian profile in XRD, the peak shape can vary substantially based on sample properties such as strain, mosaicity and a distribution of grain sizes [51]. Because of this, a range of different peak profiles will be fitted to the various data of this thesis.

The peak fits will be performed using the DIFFRAC.EVA software, which employs the Levenberg-Marquardt optimization algorithm [52]. The various peak profiles available in EVA are given below:

Gaussian profile: The Gaussian profile, $G(x, x_0, \beta)$, is usually used for peak profiles resembling highly crystalline material signatures:

$$G(x, x_0, \beta) = \frac{g_1}{\beta} \exp \frac{-g_2(x - x_0)^2}{\beta^2} \tag{3}$$

where $g_1 = 2\sqrt{(\ln 2)/\pi}$, $g_1 = 4\ln 2$, x_0 is the peak center and β is the full-width-half-maximum (FWHM).

Lorentzian profile: The Lorentzian profile, $L(x, x_0, \beta)$:

$$L(x, x_0, \beta) = \frac{2}{\pi} \cdot \frac{\beta}{4(x - x_0)^2 + \beta^2} \tag{4}$$

where β and x_0 are defined as before. The Lorentzian profile is narrower than the Gaussian around its maximum, but extends further out on both sides. The Lorentzian is better at representing XRD peaks from a sample with a distribution of grain sizes [51]. For the most part, the Lorentzian will be the default profile used in the peak fitting.

PseudoVoigt profile: The PseudoVoigt profile, $PV(x, x_0, \beta)$, is a linear combination of a Gaussian and Lorentzian profile:

$$PV(x, x_0, \beta) = \eta L(x, x_0, \beta) + (1 - \eta) G(x, x_0, \beta) \tag{5}$$

where G, L are the Gaussian and Lorentzian functions, respectively, and η is the fraction of the Lorentzian contribution to the sample, $0 < \eta < 1$. This function may be used in some cases to obtain an optimal estimate of intensity and FWHM.

Split-PseudoVoigt: The Split-PseudoVoigt profile, $SPV(x, x_0, \beta_1, \beta_2)$, is an *asymmetric profile*:

$$SPV(x, x_0, \beta_1, \beta_2) = 2(PV_{left} + a \cdot PV_{right})/(1 + a) \tag{6}$$

where

$$\begin{aligned} PV_{left} &= PV(\beta_1, \eta_1), & x < x_0 \\ PV_{right} &= PV(\beta_2, \eta_2), & x > x_0 \\ a = PV_{left}(x = x_0)&/PV_{right}(x = x_0), & \\ \beta_1 = 2h_1&, \beta_2 = 2h_2 & \\ \beta &= h_1 + h_2 & \end{aligned}$$

The Split-PseudoVoigt profile will be used for peaks that are significantly asymmetric, but where representation by *one* peak (as opposed to two or more) is most appropriate.

3.2.2 Uniform and Non-Uniform Strain

XRD may be used to assess strain in a sample [17]. The strain may be in the form of *uniform strain*, as shown in Fig. 14 (a), wherein all d-spacings of a plane are compressed (compressive strain) or stretched (tensile strain) by a uniform amount. In that case, the strain may be observed as a shift in peak position with respect to the relaxed value of the peak position. In this work, all diffraction peak positions for rutile and anatase will be compared to the peak positions derived from the lattice parameters of Table 1.

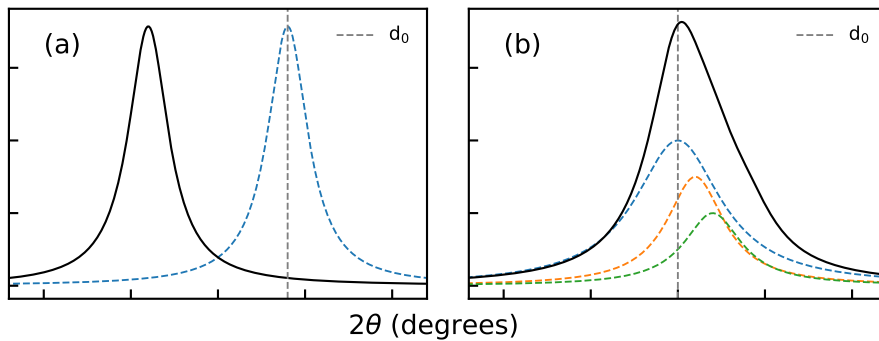

Figure 14: Examples of strain as measured by XRD: (a) Uniform strain, where a uniform stretching of d-spacings results in (black curve) a shift in measured peak position. d_0 is the relaxed/bulk d-spacing, which would give rise to the bulk peak (blue curve); (b) Non-uniform strain, where a distribution of d-spacings causes peak broadening and asymmetry. Colored curves are peaks resulting from different d-spacings.

Strain ϵ will be calculated as

$$\epsilon = \frac{d_n - d_0}{d_0} \cdot 100\% \tag{7}$$

where d_n is the d-spacing of the (hkl) reflection measured, and d_0 is the d-spacing for the same planes in the unstrained case [17].

In the case of non-uniform strain, (i.e. where crystallites are strained in varying directions and amounts), the strain will manifest itself as a broadening of the XRD peaks. An example of this is shown in Fig. 14 (b).

Asymmetry as a Result of Strain

In order to discuss asymmetry which may arise from strain, as in Fig. 14 (b), the following quantity will be used:

$$h/l = PV_{left}/PV_{right} \tag{8}$$

This quantity will be referred to as the *asymmetry parameter*, and is naturally only applied to peaks fit with the Split-PseudoVoigt function. PV_{left} and PV_{right} are defined in Eq. (6).

3.2.3 Crystallite Size Estimation

Polycrystalline, nanostructured thin films may be comprised of a distribution of grain sizes. A commmon way to estimate the mean grain size, or *crystallite size*, is to take advantage of the fact that the breadth of a diffraction peak profile is determined by the average crystallite size, as well as the lattice imperfections (strain, mosaicity, etc.) [18]. An appropriate analysis of the peak width may therefore yield an estimate of the mean crystallite size.

A common quantitative measure for mean crystallite size is achieved by the *Scherrer equation* [19]:

$$D = \frac{K\lambda}{\beta_{hkl}\cos\theta} \tag{9}$$

Where D is the average crystallite size, λ is the wavelength of the difracted X-rays, β_{hkl} is the full width at half maximum (FWHM) of the reflection peak located at angle 2θ. K is frequently called the Scherrer constant or crystallite shape factor.

In the vast literature that has employed the Scherrer equation through the last century, the value of K has been found to depend on the crystallite shape and crystallite size distribution [53]. It also depends on the definition of peak width, but throughout this thesis the FWHM will be used. As for the crystallite shape, K

will vary based on whether the crystallites are spherical, cubic, tetrahedral and so on. For all but the spherical case, K will also vary with the Miller indices of the selected peaks. The size distribution—even if all crystallites have the same shape—will affect the width of diffraction peaks, and therefore affect K as well. When crystallite shapes and size distribution are unknown, $K = 0.89$ is often taken as an estimate.

The accuracy of Eq. (9) is limited. Depending on the instrument, sample and signal-to-noise ratio, the Scherrer equation may become increasingly inaccurate when average crystallite sizes exceed 100–200 nm [54].

It should be clear that the Scherrer equation is more appropriate for *qualitative* comparisons rather than precise quantitative analysis. In this thesis, calculated crystallite sizes will be presented up to a certain significant number, but the values presented will be used for qualitative discussions rather than true estimations of crystallite sizes.

3.2.4 Preferred Orientation and Texture Coefficient

XRD may be used as a powerful tool to investigate preferred orientations and texture in a sample. For single crystals measured in the $\theta/2\theta$ configuration, only one (hkl)-family signature may be visible, indicating that only these planes lie parallel to the sample surface. The observed peak will therefore indicate which orientation lies parallel to the measured sample surface.

When samples are polycrystalline, quantitative analysis of texture and preferred orientations may be utilized. A quantity was proposed by Barret [55] (based on Harris [56]) and later termed the *texture coefficient*, γ_{hkl}:

$$\gamma_{hkl} = \frac{I_{hkl}/I_{r,hkl}}{\frac{1}{n}\sum I_{hkl}/I_{r,hkl}} \tag{10}$$

where I_{hkl} is the measured intensity from diffraction peak corresponding to plane (hkl). $I_{r,hkl}$ is the measured intensity from the same peak given that the sample grains are *completely random*. n is the number of peaks that are summed over. Note that the sum is carried out over each hkl-combination.

Originally, Eq. (10) was derived for wires or rolled metals. However, the texture coefficient has since been applied by many authors to thin films [19]. Its credibility when applied to thin films, however, is debatable. The author of the present work has not found any justification for its applicability in thin film analysis, and so an argument for its usage will be made here.

In an ideal, randomly oriented polycrystalline sample, the intensity of the strongest peak I_0 may be arbitrarily assigned the value $I_0 = 100$. All other peak intensities $I_{r,hkl}$ will be some fraction of this value. For concreteness, refer to the value $I_0 = I_{r,110} = 100$ for powdered rutile, in relation to which $I_{r,101} = 46.8$ (revisit Table 2).

If one considers a set of XRD data where the strongest peak intensity is normalized

to $I_0 = 100$, then for truly randomly oriented grains, all ratios $I_{hkl}/I_{r,hkl}$ will be unity. This means that $\gamma_{hkl} = 1$ for all families of planes, and the data is said to stem from an *untextured* sample. If a certain peak intensity I_{mno} is stronger than what would be expected from randomly oriented grains, $\gamma_{mno} > 1$ for this peak and likewise $\gamma_{hkl} < 1$ for all other peaks. Any sample for which a significant number of γ_{hkl} deviate significantly from unity will be said to be a *textured* sample. A sample for which only *one* family of planes is visible (so that, in principle, γ_{hkl} is infinite) will be said to be *highly textured*.

As an example, consider the simulated XRD diffractogram of Figure 15. In the figure, a simulated rutile powder pattern is displayed which is identical to that of Figure 3, except that the R (200) peak has increased intensity. The calculated texture coefficients are also shown. With $\gamma_{hkl} = 4.25 > 1$, it is clear that (100) orientation is a preferred orientation. Furthermore, since all other γ_{hkl} are equal and < 1, the other orientations are all *equally* not-preferred. This reflects the fact that *only* the R (200) peak has been altered with respect to the ideal powder pattern in the simulation. In a real sample, the intensities would usually be more scrambled, so that there could be two or more peaks with $\gamma_{hkl} > 1$, and so on.

The term *preferred orientation* is not meaningful when applied to GIXRD, as one probes over several orientation angles in **k**-space, as was seen in Figure 4. In this work, *preferred orientation* will refer to the dominating family of planes when measuring in the $\theta/2\theta$ configuration.

If *few* peaks from a phase are available (2 or 3), a substitute for γ_{hkl} will be used: I/I_0, where I_0 is the strongest peak in the phase's powder XRD pattern. This is in order to see if the peak is stronger or weaker than what would be expected from an untextured sample.

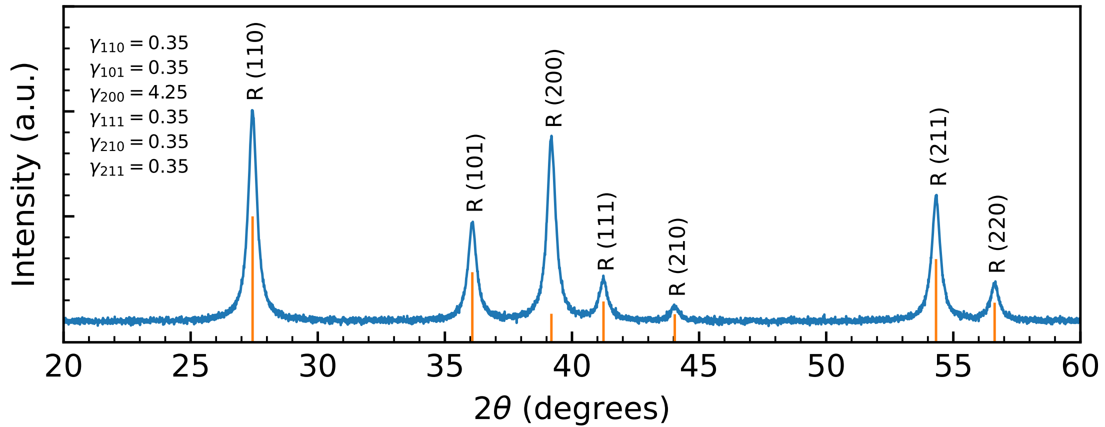

Figure 15: Simulated XRD diffractogram showing a rutile powder pattern with (100) preferred orientation. The relative peak intensities of all peaks agree with the rutile powder XRD pattern, except for the R (200) peak which is stronger relative to the powder pattern. The calculated γ_{hkl} quantify the degree of preferred orientation for the various planes.

3.2.5 Phase Quantification of Rutile and Anatase Mixtures

Alexander and Klug developed simple relations between the diffracted intensities and weight fractions of constituents in a powder mixture [18]. The underlying assumption in powder diffraction is that orientations of the crystal grains are random, and that a statistically relevant amount of grains ensures that the XRD pattern is reproducible. Consequently, the relative peak intensities from one constituent are a fixed property of the powder diffraction pattern.

Alexander and Klug postulated a relation between $(I_n)_i$, the intensity of the n-th diffraction peak from component i, the component's weight fraction in the sample, x_i, mass absorption coefficient μ_i and density ρ_i:

$$(I_n)_i = \frac{(K_n)_i x_i}{\rho_i \mu_i} \tag{11}$$

where $(K_n)_i$ depends upon the nature of component i and the geometry of the apparatus.

Spurr and Myers further developed the discussed relation specifically for powder diffraction of rutile-anatase mixtures [57]. For a powder rutile-anatase mixture, Spurr and Myers effectively set the ratio of $(K_0)_A/(K_0)_R$, the ratio of $(K_n)_i$ for the strongest anatase and rutile peaks in powder XRD, respectively, to be a constant K. This gave:

$$\frac{x_A}{x_R} = K\frac{I_A}{I_R}, \tag{12}$$

where I_A and I_R are the integrated intensities of the anatase (101) and rutile (110) peaks, respectively. Spurr and Myers used the physical weights (w_A and w_R) of anatase and rutile in the sample, but their relation is equivalent with (12) by assuming a mixture of pure rutile and anatase.

By assuming powder or polycrystalline samples with a statistically relevant number of crystal grains, it is reasonable to expect K to be reproducible across samples and measurements. The relative intensities of I_A and I_R are thus assumed to only depend on the weight fractions of rutile and anatase in the sample.

Assuming K to be constant, Spurr and Myers further developed a relation for the weight fraction of anatase in the sample:

$$x_A = \frac{1}{1 + \frac{1}{K}\frac{I_R}{I_A}} \tag{13}$$

By doing linear regression based on I_A/I_R from a range of sample with known x_A values, Spurr and Myers proposed the approximation $1/K = 1.26$, giving:

$$f = \frac{1}{1 + 1.26\frac{I_R}{I_A}} \tag{14}$$

where f is now an approximation of the weight fraction of anatase in the sample. Equation (14) is frequently called the Spurr equation.

Eq. (14) now provides a simple method of quantifying the rutile-antase ratio of a TiO_2 sample through XRD. The underlying premise for its use is, as mentioned, that the sample is powdered or polycrystalline with random orientations of crystal grains (so that $\gamma_{hkl} = 1$ for all peaks).

However, in this thesis, none of the samples are seen to be fully un-textured, as they all display some significant texture. Because of this, quantitative analysis by Eq. (14) will not be performed. However, *qualitative* analysis will be made by noting that from Eqs. (12) and (14), anatase peak intensities are generally expected to be only slightly higher than for rutile peaks ($I_R = I_A$ would give $f = 0.44$). Based on this, qualitative phase quantification will be made based on the XRD data.

3.2.6 Estimation of Uncertainties

In the XRD measurements presented in this thesis, there is a degree of uncertainty for all the estimated parameters presented in sections 3.2.1–3.2.5. Sources of uncertainty and how they will be accounted for is presented here.

Uncertainty in peak position

There will be an uncertainty in peak positions 2θ as a result of the finite resolution of the XRD measurements:

$$\Delta 2\theta = \frac{R}{2} \tag{15}$$

where R is the angular step size (in degrees).

There will also be an uncertainty in 2θ as a result of calibration or misalignment of the samples. This could lead to a systematic shift in peak positions. However, substrate peaks with known 2θ values will be available for all measurements. The data will therefore be adjusted to fit the substrate peak positions.

There will also be a peak shift because of the asymmetry of the X-ray source wavelengths. The CuKα X-ray sources relevant for this thesis, when used without monochromators, generally produce *two* spectral lines, the CuKα_1 line, which has wavelength $\lambda = 1.5406$ Å, and the CuKα_2 line with wavelength $\lambda = 1.5444$ Å [17]. The Kα_2 line will generally only be visible for peaks arising from highly crystalline components (like the substrate peaks). For film peaks, the Kα_2 line may still cause

some asymmetric peak broadening towards higher angles, which may shift the apparent peak position. During peak fitting, DIFFRAC.EVA calculates the Kα_2 line, and accounts for this shift. The possibility of Kα_2 shifting will thus be ignored.

Given the above reasoning, with respect to misalignment and the CuKα doublet, the uncertainty in 2θ will still be as in Eq. (15).

Uncertainty in uniform strain calculations

The uncertainty in calculations for uniform strain, $\Delta\epsilon$, by Eq. (7), mainly depends on $\Delta\theta$ and Δd_0, the latter being the uncertainty in reference d-spacings. Reports for the lattice constants for rutile and anatase vary in literature, but an estimation of this variation is beyond the scope of this thesis. Uncertainties in d_0 of Eq. (7) will therefore not be assessed. However, there could be a systematic error in the discussed results, as a consequence of the d_0 values used being different from the actual d_0-values.

$\Delta\epsilon$ will therefore depend only on uncertainties in calculated d-spacings, d_n. These values in turn depend on $\Delta\theta$. Simple error propagation of Eq. (1) for Δd_n and Eq. (7) for $\Delta\epsilon$ gives an estimate $\Delta\epsilon \approx 0.9\%$ for θ–2θ and GIXRD measurements. The value increases for increasing angles. For HRXRD, the estimate is $\Delta\epsilon \approx 0.7\%$.

Uncertainties in strain calculations will generally not be discussed, as the results are mostly interpreted in a qualitative manner. The errors are expected to be systematic for all measurements. Note that the the uncertainties in ϵ are large as a result of d_n varying as $1/\sin\theta$. The uncertainties in 2θ, however, are sufficiently small.

Peak broadening and uncertainties in crystallite size estimates

The width of the peaks (effectively the FWHM, β) are important for the estimation of crystallite sizes through Eq. (9). An evaluation of peak broadening will therefore be given.

In addition to Kα_2 broadening, there are several other potential sources of peak broadening. One of these is divergence of the diffracted X-ray beam, which applies to all XRD measurements. For GIXRD, there will be a broadening of peaks as a result of the **k**–vector crossing the diffraction rings at an angle (see Fig. 4). There could also arise peak broadening from non-uniform strain (see Fig. 14 (b)).

The peak broadening in the observed FWHM, β_{exp}, can be described in terms of the *instrumental* broadening β_{inst}, broadening from strain β_{strain}, and broadening from finite crystallite size β_{size} [17].

For Gaussian peaks,

$$\beta_{exp}^2 = \beta_{size}^2 + \beta_{strain}^2 + \beta_{inst}^2 \tag{16}$$

and for Lorentzian peaks,

$$\beta_{exp} = \beta_{size} + \beta_{strain} + \beta_{inst} \tag{17}$$

In the θ–2θ and GIXRD measurements, broadening of β_{exp} when using Eq. (9) will generally be ignored, as the analysis of these results will be mainly qualitative. The point of applying the Scherrer equation in these cases will be comparisons between different peaks, between different phases within a sample, and between samples.

For the HRXRD measurements, an estimate for $\Delta\beta$ will be made. The instrument used (to be presented in Section 4) was found to give FWHMs $< 0.01°$ for the substrate peaks. Because of this, β_{inst} is set to 0.01° in calculations. Furthermore, based on the distance between the most shifted and least shifted peaks in the HRXRD measurements (the A (004) peak from B5 and A2 on LAO, respectively, to be presented in Section 5.2.4), an estimate of 0.2° will be set for the uncertainty in β, in order to account for uncertainty in both β_{inst} and β_{strain}. Lorentzian peaks will be assumed.

The uncertainty in estimated mean crystallite size, ΔD, depends on the uncertainty in θ, β, as well as K, the Scherrer constant. $K = 0.89$ will be used in calculations, but K may in reality vary from 0.6 to 2.0 based on the sample [53]. Because of this, ΔK is set to 0.7.

The uncertainty in mean crystallite sizes will thus be estimated through propagation of uncertainty:

$$\Delta D = \sqrt{\left(\frac{\partial D}{\partial K}\right)^2 (\Delta K)^2 + \left(\frac{\partial D}{\partial \beta}\right)^2 (\Delta \beta)^2 + \left(\frac{\partial D}{\partial \theta}\right)^2 (\Delta \theta)^2} \tag{18}$$

where D is given from Eq. (9).

Uncertainty in peak fitting

The peak profiles used in peak fitting may not always match the raw data peak shapes exactly. There is therefore an intrinsic uncertainty in the quantitative data based on the peak fitting. However, the fits are mainly used to extract the peak position x_0 and FWHM β, and variations in these values are not expected to be significant for most of the peak fitting. Uncertainties from peak fitting will therefore generally not be discussed, unless the fits appear significantly poor.

The validity of the peak fits will be assessed qualitatively by visual examination of the fits. Curve fits will always be plotted for the reader to assess.

3.3 Raman Spectroscopy Analysis

Raman spectroscopy will in this thesis only be used as a supplementary method to XRD. The Raman spectra will be compared to the rutile and anatase reference spectra of Figure 9. Qualitative analysis will then be performed in the context of the XRD discussion. Some considerations of relative Raman peak intensities will be made, in relation to sample orientation considerations from XRD. Aside from this, no detailed analysis of the Raman spectra will generally be made.

4 Experimental Details

This section will describe the experimental details behind the results of this thesis. First, the sample preparation methods will be described. These are divided into "uniform undoped" samples, which is a series of samples deposited on four substrates simultaneously, using only a TiO_2 target. Next, the combinatorial PLD samples, termed the "Continuous Compositional Spread" (CCS) series, will be described. The doped CCS samples were deposited on 2×2 inch silicon wafers, and have a continuous, lateral gradient in (Cr,N) concentrations along the center line of the wafers. Note that the CCS series will contain both (Cr,N)-doped samples, as well as undoped "reference samples".

After the sample preparation, the setup and procedures for XRD and Raman spectroscopy are described.

4.1 Preparation of Uniform Undoped Samples

The uniform undoped samples described in this section were prepared by Marina Rodrigues Jorge and Thomas Brakstad as part of their PhD research at NTNU Trondheim. Measured film thickness was provided by Thomas Brakstad.

The uniform undoped samples were prepared through conventional PLD, using a KrF excimer laser (Lambda Physics COMPex Pro, 248 nm, 25 ns) at 5 Hz to ablate a titanium dioxide target (TiO_2 compressed ceramic powder). The target was pre-ablated with 1000 pulses before each deposition. For each deposition, four 10×10 mm^2 substrates were deposited on simultaneously: Si (100), LAO (001), STO (001) and sapphire (0001).

The samples are labelled based on the deposition parameters used during their synthesis. The labels along with deposition parameters are given in Table 5. The samples are categorized as "series A" and "series B" in accordance with previous work on the samples [58], where A and B denote samples deposited with laser fluence 0.8 and $2.0\,J/cm^2$, respectively.

Table 5: The deposition parameters for the uniform uniform samples. P_{dep} is the gas pressure in the vacuum chamber. O_2 and A_2 are the oxygen and argon gas flows. T_s is the nominal substrate temperature during deposition. The measured film thickness (nm) is also given. No good thickness model could be made for B1.

Sample label	O_2 (sccm)	Ar (sccm)	P_{dep} (mbar)	Laser fluence (J/cm^2)	T_s (°C)	Thickness (nm)
B1	0	100	1.1×10^{-2}	2.0	700	N/A
B2	1	99	1.1×10^{-2}			686
B3	2	98	1.2×10^{-2}			667
B4	10	90	1.2×10^{-2}			686
B5	100	0	1.7×10^{-2}			687
A2	50	0	2.7×10^{-2}	0.8	700	229

The uniform undoped samples will be referred to using their label and substrate, e.g. "B3 on STO" will refer to the sample deposited on an STO substrate with the "B3" deposition parameters from Table 5. The "A series" or "B series" will refer to all samples of series A or B, when appropriate.

4.2 Continuous Compositional Spread (CCS) Samples

The samples described in this chapter were synthezied by Hogne Lysne and Thomas Brakstad as part of their PhD work.

This thesis will investigate three (Cr,N)-codoped TiO_2 films, and two undoped reference CCS samples. The CCS films were all deposited with a laser fluence of 1.5 J/cm^2 and similar pressures as for B5 in Table 5. The films were deposited using combinatorial PLD (revisit Section 2.4.1), where plumes were deposited on two positions for each sample: "Plume center one" ("first plume center") and "plume center two" ("second plume center"). For the undoped reference samples, a TiO_2 target was used for both plume centers. For the doped samples, only a TiO_2 target was used for the first plume center, while both a TiO_2 target and a chromium nitride (CrN) were used at the second plume center. An overview is provided in Table 6.

Table 6: Overview of the CCS samples described in this section. The table gives the substrate that the film was deposited on, whether the film was (Cr,N)-doped, whether it was cycled to N_2 gas ("capping"), and the nominal substrate temperature T_s.

Sample	Substrate	(Cr,N)-doping	Cycling to N_2 gas	T_s
CCS-Si-NoCap-Ref	Si (100)	No	No	700 °C
CCS-Si-NoCap	Si (100)	Yes	No	700 °C
CCS-Si-Cap-Ref	Si (100)	No	Yes	550 °C
CCS-Si-Cap	Si (100)	Yes	Yes	550 °C
CCS-LAO-Cap	LAO (001)	Yes	Yes	550 °C

Initial (previous to this work) studies of the combinatorial deposition had revealed that the ablated CrN target would form Cr_2O_3 under deposition of O_2 flow, while CrN would be formed if deposited under N_2 flow. However, it was also desirable to ablate the TiO_2 target under pure O_2 flow, because the TiO_2 crystal quality was much improved when deposited in oxygen. Because of this, a method termed "capping" was used for two of the films. This involved ablating the CrN target using an N_2 background gas, and further ablate a few pulses of TiO_2 while *maintaining* the N_2 gas flow, before the gas was switched back to O_2. This ensured that the CrN was "capped" before introduction of O_2 gas into the chamber, so as to hinder oxidation of chromium in the film, which would form the undesired Cr_2O_3. The chamber thus alternated between N_2 and O_2 during the deposition.

One doped sample was deposited using only O_2 gas. This will be referred to as "un-capped". The reference sample for this un-capped sample was also deposited using only O_2, but was not (Cr,N)-doped, and therefore the term "un-capped" does not apply to this sample.

Because of the switching between gas flows during capping, additional pauses were introduced in the deposition to allow the gas chamber to settle. After switching from O_2 to N_2 gas, a 30 second pause was introduced. Then, the TiO_2 target was ablated, followed by a 20 second pause. The chamber then switched to O_2 gas, followed by another 30 second pause, after which the cycle was repeated.

Tables 7 and 8 summarize the procedures for *one* deposition sequence for the un-capped and capped films, respectively. The sequences were repeated 400 times for the samples on silicon, and 600 times for the sample on LAO.

Table 7: CCS film deposition sequence for samples CCS-Si-NoCap and reference sample. For the sample without doping (CCS-Si-ref) the 90 laser pulses of step 3 is replaced with a 9 seconds wait.

Step no	Target material	Plume location	Number of pulses	Background gas
1	TiO_2	-1.3 cm	26	O_2
2	TiO_2	1.3 cm	22	O_2
3	CrN	1.3 cm	45	O_2

Table 8: CCS film deposition sequence for samples CCS-Si-Cap, CCS-LAO-Cap and reference sample without doping. For the sample without doping (CCS-Si-Cap-Ref), the 90 laser pulses of step 3 was replaced with a 9 seconds wait.

Step no	Target material	Plume location	Number of pulses	Background gas
1	TiO_2	-1.3 cm	26	O_2
2	TiO_2	1.3 cm	12	O_2
3	CrN	1.3 cm	90	N_2
4	TiO_2	1.3 cm	10	N_2

4.2.1 CCS–Si–NoCap and CCS–Si–NoCap–Ref

Samples CCS-Si-NoCap and CCS-Si-NoCap-Ref were deposited on a Si (100) wafer using the CCS sequence described in Table 7. A schematic of the simulated thickness from each deposition sequence, showing the individual steps, is displayed in Figure 16. For the reference sample, step no. 3 (ablation of CrN target) was replaced by a 9 second pause. The sequence was repeated 400 times for both the doped and reference samples. Note that the background gas was 100% O_2 for all steps, meaning that there was no capping of the (Cr,N)-doping.

A measured thickness map (provided by Thomas Brakstad and Hogne Lysne) for CCS-Si-NoCap is shown in Figure 17. The sample was cut into four areas, indicated by Fig. 17, all of which were measured by XRD and Raman spectroscopy. The figure indicates average simulated at% Cr doping within each area, and the size of each area in cm. Similar thickness maps will be provided for the other samples in Section 5.6, but are omitted in this section for brevity.

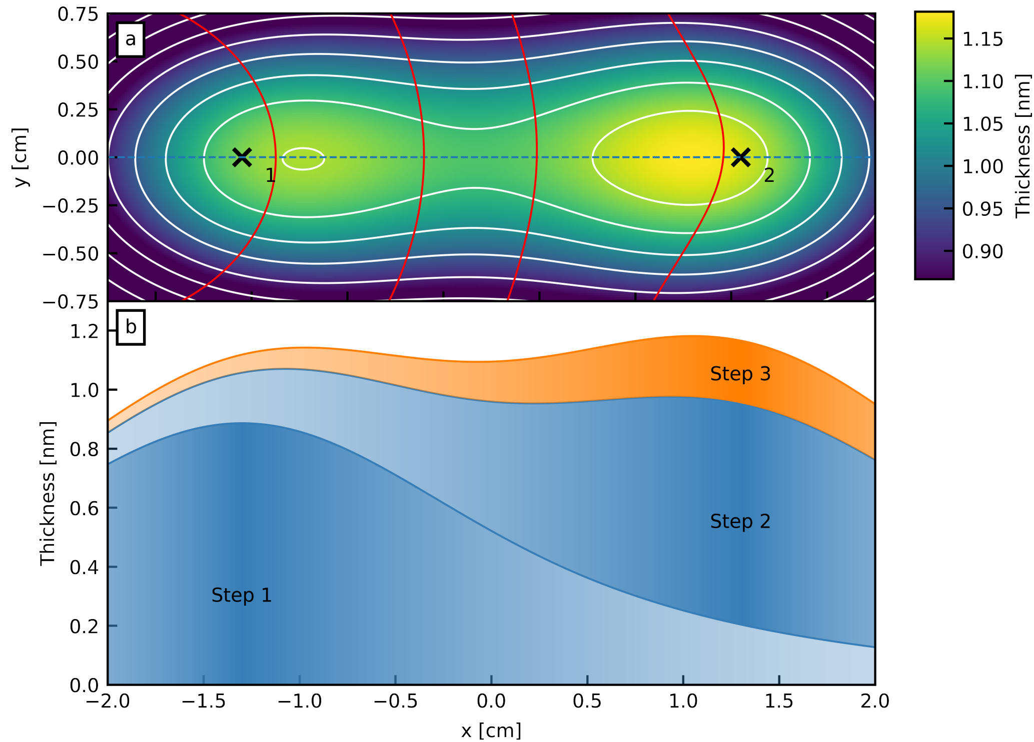

Figure 16: Schematic of simulated film thickness from one deposition sequence, for sample CCS-Si-NoCap, based on Table 8; (a) Thickness map resulting from one deposition cycle. x_1 and x_2 are the first and second plume center, respectively. Red curves show at% for Cr, from left to right: 3 at%, 5 at%, 7 at% and 9 at%. (b) Cross-section of the wafer center line (dashed line in (a). Blue areas denote TiO_2 deposited under O_2, orange denotes CrN deposited under N_2.

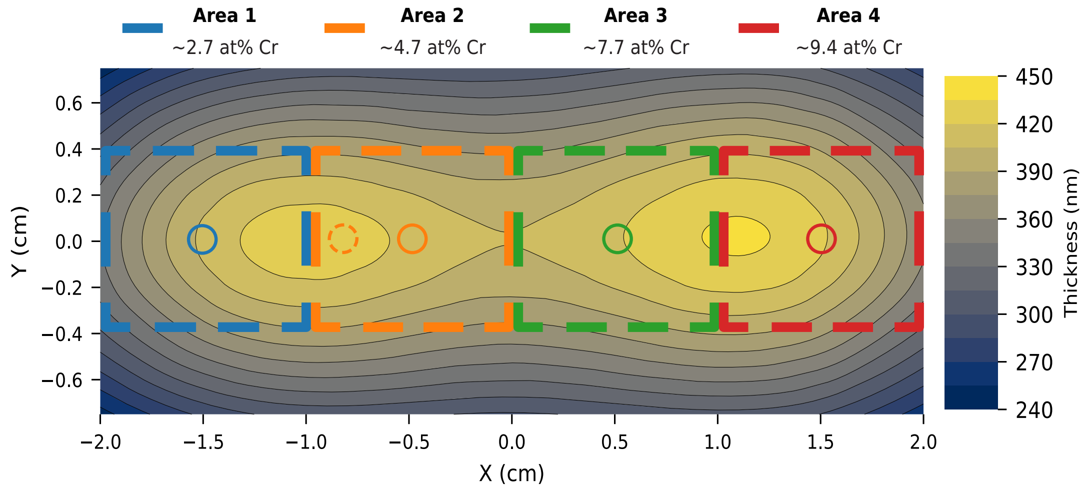

Figure 17: Measured thickness map of sample CCS-Si-NoCap, based on ellipsometry data. Dashed boxes indicate the different areas which were cut into separate pieces. The average simulated at% Cr levels are given for each area. The colored circles (including dashed, orange circle) indicate the approximate positions where Raman spectra were acquired.

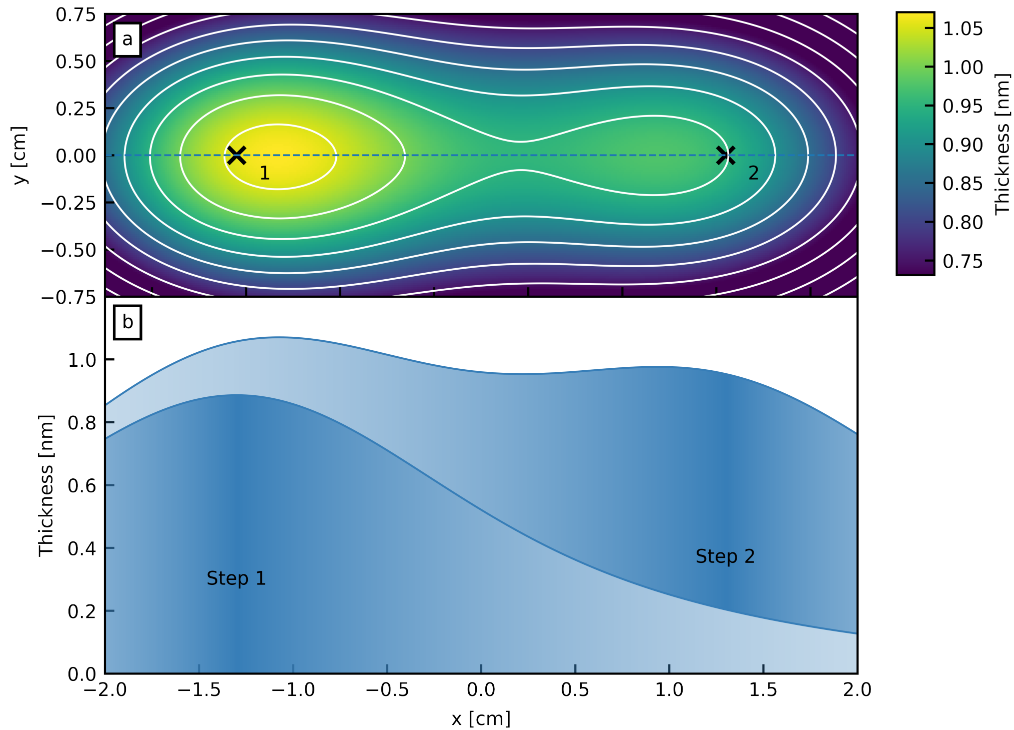

Figure 18: Schematic of the the deposition cycle for sample CCS-Si-NoCap-Ref, based on Table 7. Note that this does not have any CrN doping, in contrast to CCS-Si-NoCap in Fig. 17. See Figure 16 for explanation.

4.2.2 CCS-Si-Cap, CCS-Si-Cap-Ref and CCS-LAO-Cap

Samples CCS-Si-Cap and CCS-Si-Cap-Ref were deposited in a similar manner as the samples in Section 4.2.1, but with cycling to N_2 at the second plume center (*capping* of the (Cr,N)-doping). The CCS sequence was described in Table 8. The gas was thus cycled to N_2 during steps 3 and 4. For the reference sample, step no. 3 in Table 8 (ablation of CrN target) was replaced by a 9 second pause. The sequence was repeated 400 times for both the doped and reference samples.

CCS-LAO-Cap was deposited simlarly to CCS-Si-Cap, but with a LAO substrate, and 600 repetitions of the cycle in Fig. 20.

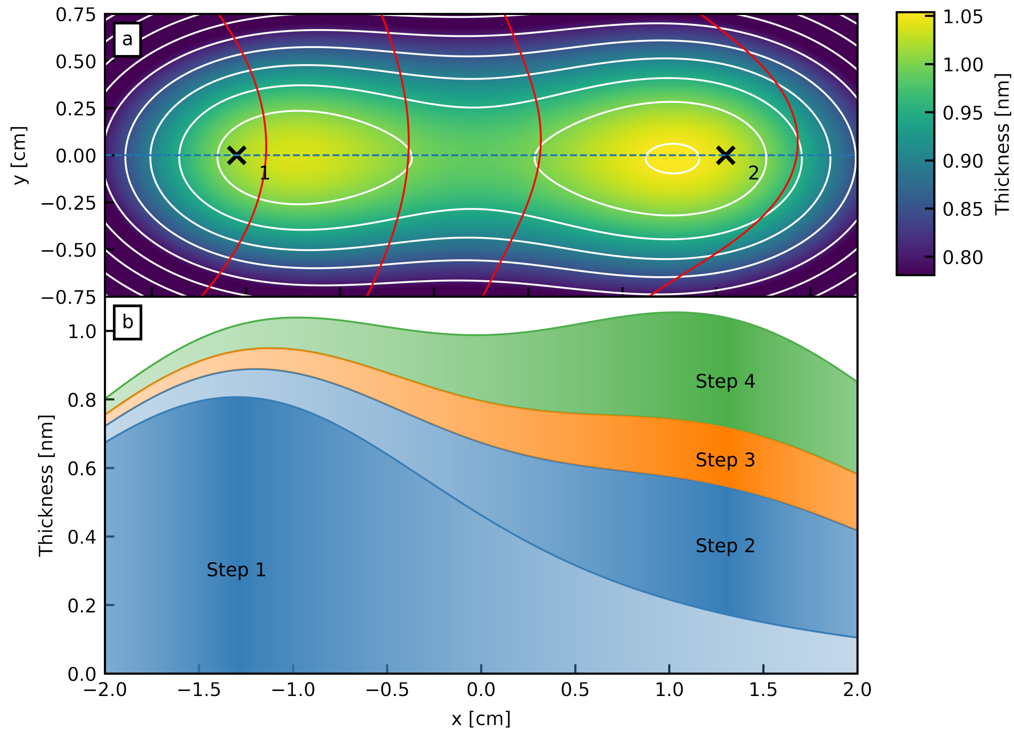

Figure 19: Schematic of the deposition cycle for sample CCS-Si-Cap, based on Table 8. Green area in (b) denotes TiO_2 deposited under N_2, which is absent for CCS-Si-NoCap in Fig. 16. Otherwise, see Fig. 16 for explanation.

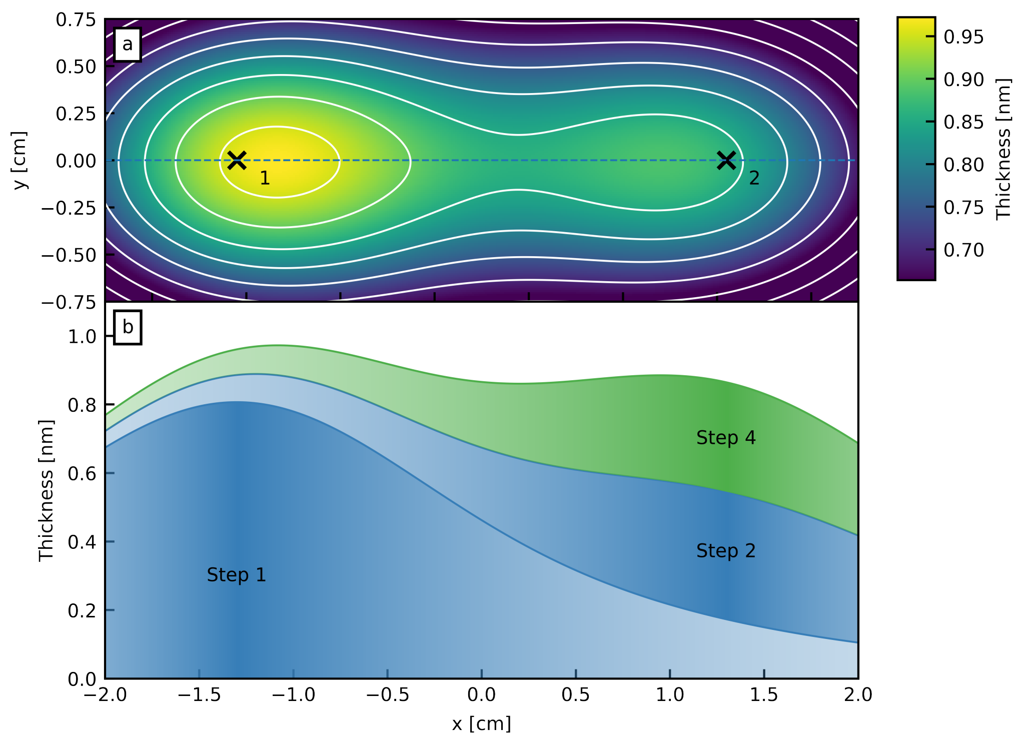

Figure 20: Schematic of the deposition cycle for sample CCS-Si-Cap-Ref, based on Table 8. See Figure 16 for explanation.

4.3 X-ray Diffraction Setup

Uniform undoped samples

***θ–2θ* scan**: The θ–2θ XRD measurements were made using a Bruker D8 A25 DaVinci X-ray Diffractometer with CuKα radiation. The measured 2θ range was 10° to 80°, with a 0.013° step size and a step time of 2 seconds/step. During the measurement, the samples were mounted on a rotating stage, which spun the sample a full rotation per step. A divergence slit with 0.3 mm opening was used in front of the X-ray source.

The instrument did not have a monochromator. The X-ray source was also known to have contaminated radiation resulting in a large number of substrate artifacts in the data. The artifacts are, however, predictable, and are easy to separate from the film peaks. Artifacts will be marked when it is appropriate.

GIXRD: The GIXRD measurements were, similar to the θ–2θ scans, made using a Bruker D8 A25 DaVinci X-ray Diffractometer with CuKα radiation. The samples were not mounted on a rotating stage. All samples except B5 on Si were measured at an angle of incidence $\theta_i = 2.0°$ in the 2θ range 15 to 70°. The step size was 0.02° with 3.5 s time per step. A Göbel mirror was used in front of the source with a 0.2 mm divergence slit. Soller slits were mounted in front of the detector.

For B5 on Si, the angle of incidence was chosen as $\theta_i = 1.0°$ because of a problematic substrate signal. The 2θ range was 15° to 60°.

HRXRD: HRXRD measurements were made using a Bruker AXS D8 Discover HRXRD diffractometer with a half circle geometry (θ between 0° and 180°). Incident beam optics included a Göbel mirror and a V-groove beam compressor, giving CuKα_1 radiation and a full width at half maximum for Si (111) of less than 0.01°.

Only samples B3–B5 and A2 on LAO, STO and Sapphire were measured using HRXRD. Prior to deposition, the samples were expected to be influenced by the substrates due to low lattice mismatch, which could give highly textured films. In the θ–2θ scans, these samples showed strong, single film peaks, and HRXRD was used to study strain and mosaicity using $\omega/2\theta$ and rocking curve scans for these peaks.

For each measurement, the sample was aligned in order to maximize the intensity of the substrate peak that was closest to the measured film peak. This effectively meant correcting for substrate miscut, so that $\theta = 0$ corresponded to the beam being parallel to the actual substrate planes, and not just parallel to the film surface. Note however that not even the substrates are without defects, and so there are is some small mosaic spread in the substrate planes.

For the films on LAO and sapphire, the ω–2θ scans were performed using a 0.6 mm receiving slit, 0.005 ω (angle of incidence) step size and 3 second/step scan speed. Rocking curves were performed on the maximum of the detected film peaks with 0.6 mm receiving slit, 0.01 ω step size and 1 second/step scan speed.

The films on STO were measured in a similar manner, except that the scan speed was reduced to 1 second/step. This was in order to save time, based on the observation that the samples on STO gave off much higher intensity in the θ–2θ scans compared with the other samples.

CCS Samples

The CCS films were measured in the θ–2θ configuration in the same manner as the Uniform Undoped samples. Two exceptions were CCS-Si-Cap-Ref, for which the 2θ range was reduced to $(15°, 60°)$, and CCS-Si-NoCap-Ref, where the step time was decreased to 1 sec/step because of time constraints.

4.4 Raman Spectroscopy Setup

Raman spectroscopy was performed through a Renishaw InVia Refex Spectrometer System, using a VIS excitation laser at 532 nm (100 mW), with 2400 mm^{-1} grating and 100× objective lens. Each measurement was made by doing 50 accumulations of 0.5 s exposure at 50% laser intensity. For the undoped samples, the measurements were performed approximately at the center of each sample. For the CCS samples, measurements were performed at approximately at the center of each *area* (as defined in the previous section), except where specified.

The laser spot size was expected to be approximately 1 µm.

5 Results and Discussion

The results and discussion for all measured samples are presented in this section. First, the results and discussion of the undoped uniform samples are presented. The samples are grouped according to their substrates: First the films on silicon, then LAO, STO and sapphire. This is followed by an overall discussion of the uniform undoped films.

The results from the continuous compositional spread (CCS) samples will be presented next. All samples were investigated by θ–2θ measurements, but note that Raman spectroscopy was not performed on the reference samples. Results and discussion for CCS-Si-NoCap-Ref (pure O_2 gas, no doping) will be presented first, followed by CCS-Si-Cap (pure O_2 gas, *with* (Cr,N)-doping). Afterwards, a short summary based on the results from these samples will follow. Next, CCS-Si-Cap-Ref (periodic cycling to N_2 gas, no doping) will be presented, followed by CCS-Si-Cap ((Cr,N)-doping and capping with N_2 gas) and a summary. CCS-LAO-Cap will be presented last.

Finally, an overall discussion of the results from the CCS samples will be presented.

See Section 3.2.6 for discussion of uncertainties and sources of errors.

5.1 Uniform Undoped Samples on Si (100)

5.1.1 Theta-2Theta Measurements

The results of the θ–2θ scan for B1–B5 and A2 on Si substrates are shown in Figure 21, with the same data plotted in logarithmic scale in Figure 22. The calculated powder XRD patterns (meaning peak positions and relative powder XRD intensities) for rutile and anatase are also shown when approriate. As stated in Section 4, the angular resolution in 2θ was 0.013°, so there is an uncertainty $\Delta 2\theta = \pm 0.007°$ in the presented peak values. The discussed peak values are based on peak fitting, to be presented later in the section.

In Figure 21, the sharp Si (200) substrate peak at $2\theta = 32.98°$, in addition to two other substrate artifacts at 54.57° and 56.34°, can be seen for all samples. These are marked by red asterisks. Apart from these, broader peaks are seen for all samples, which indicate crystalline materials in the films. Some peaks align with the displayed rutile or anatase powder XRD patterns, indicating that these peaks may come from one of the two TiO_2 phases. Other peaks, however, do not align with either of the phase (hkl) references, suggesting the existence of other phases.

In sample B1, only one peak may *possibly* be attributed to rutile: the peak located at $2\theta \approx 39.19°$, the calculated R (200) location. If this peak indeed comes from rutile, then it is suggested that all detected rutile grains in this sample are oriented with the (100) planes parallel to the film surface. However, since a full rutile pattern is not observed, the assessment of this peak will rely on complimentary methods, to be presented in sections 5.1.1 and 5.1.3. Several other peaks can be seen for sample B1 in figures 21 and 22, but these do not align with either rutile or anatase peak positions, suggesting the existence other phases in the film.

For sample B2 several peaks are seen to align with the rutile powder pattern in figures 21 and 22. The peaks are broad, suggesting small crystallite sizes, and seem to be somewhat shifted from the calculated rutile pattern when studying Figure 22, indicating strain in the film. Sample B2 also shows a peak at $2\theta \approx 26.39°$, which may be of the same origin as the one observed at $\approx 26.55°$ in B1. This finding indicates that there is some polycrystalline rutile in the sample, along with a phase that is neither rutile or anatase.

Samples B3 and B4 both show a clear rutile pattern, as film peaks may be seen at all rutile powder XRD reference locations in figures 21 and 22. Note however that the peaks at $2\theta \approx 39.19°$, the rutile (200) peak location, are considerably more pronounced than the other peaks. In particular, their relative intensity to the other peaks far exceed what is expected from the powder XRD pattern (which assumes randomly oriented grains). This indicates a (100) preferred orientation for the rutile phase in samples B3 and B4.

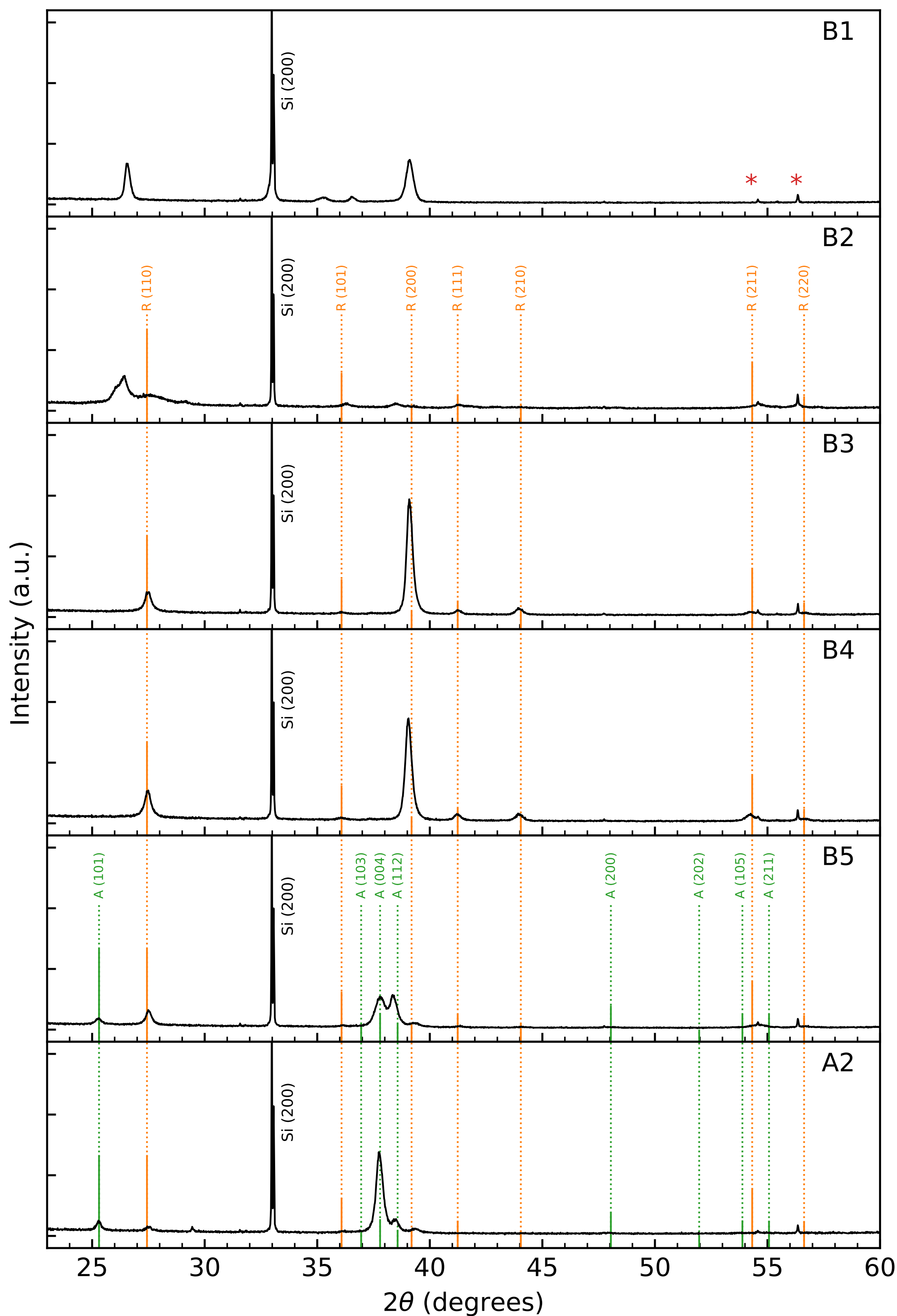

Figure 21: θ–2θ data for B1–B5 and A2 on silicon. The peak locations and relative powder XRD intensities for rutile and anatase are shown in solid lines, with dashed lines to guide the eyes. In the topmost plot, substrate artifacts are marked by red asterisks.

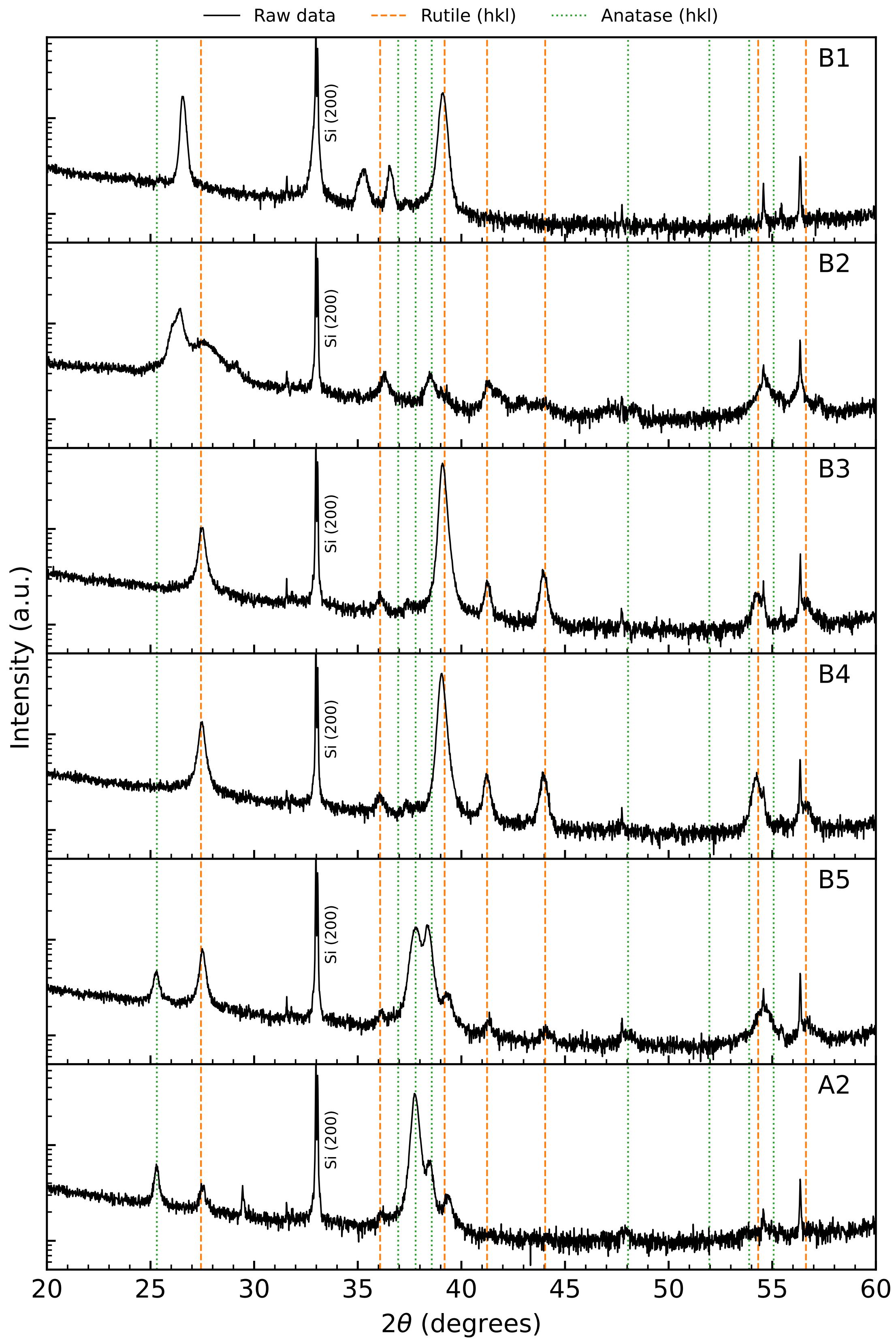

Figure 22: Logarithmic plot of the θ–2θ data for the films on Si substrates. Rutile and anatase reference peak positions are indicated by dashed and dotted lines.

From sample B5, several peaks can be seen in figures 21 and 22 that were not observed in samples B1–B4. All of these peaks may be attributed to the anatase phase, which is apparent when comparing the peak locations with the anatase powder pattern in Figure 22. The existence of anatase is particularly indicated by the appearance of the "characteristic" A (101) peak at $2\theta = 25.31°$. However, the intensities of the at A (004) and A (112) peaks far exceed the expected intensity from the powder pattern. This indicates a preferred orientations for the (001) and (112) planes.

Several rutile peaks can also be seen in figures 21 and 22 for sample B5, similar to samples B3 and B4. This implies that rutile exists in B5, in addition to the anatase phase. However, anatase seems to dominate, as the intensities are far stronger than the rutile peak intensities. Note also that the R (200) peak appears to be stronger than all other rutile peaks except for R (101), which indicates that the (100) preferred orientation also holds for sample B5. This may also come from an anatase–to–rutile transformation at anatase (112) twin boundaries [22].

For sample A2, not as many rutile peaks can be seen in figures 21 and 22, and the anatase peaks seem to dominate the XRD pattern. The A (004) and A (112) peaks are the most pronounced of the anatase peaks. It is therefore suggested that this film has a strong (001) preferred orientation in the anatase phase, in addition to a minor preferred orientation for the (112)-direction. Note that although only the R (101) and R (200) rutile peaks are visible, the result suggests that there is a (100) preferred orientation in the rutile phase, as the R (200) peak is far stronger than what one would expect from randomly oriented grains.

Quantitative data analysis

Curve fits were performed on the θ–2θ data from all of the films on silicon substrates. The resulting fitted curves are displayed in Figure 23 together with the raw data. Referring to Section 3.2.1, the main extracted values from the curve fits are the peak positions x_0 and FWHMs β in Eqs. (3)–(6). From x_0, the mean d-spacing for each reflection is calculated from Bragg's law (Eq. (1)). The integrated intensities are also calculated.

The extracted quantitative data are displayed in bar plots in Figure 24. The figure shows (a) the integrated intensity I_{hkl} for each peak, (b) the calculated strain using Eq. (7), (c) the FWHM given by Eqs. (3)–(6), (d) the estimated mean crystallite size from Eq. (9), and (e) the calculated texture coefficient using Eq. (10). Only peaks that were attributed to either rutile or anatase are shown. Note that sample B1 is omitted, because a statistically sufficient number of TiO_2 peaks could not be confidently identified.

The data from Figure 24 confirms some of the trends that were qualitatively seen from the difractograms. As seen in Fig. 24 (a), the rutile peak intensities were generally strongest for samples B3 and B4, particularly for the R (200) peak. Anatase peaks were only measured in samples B5 and A2.

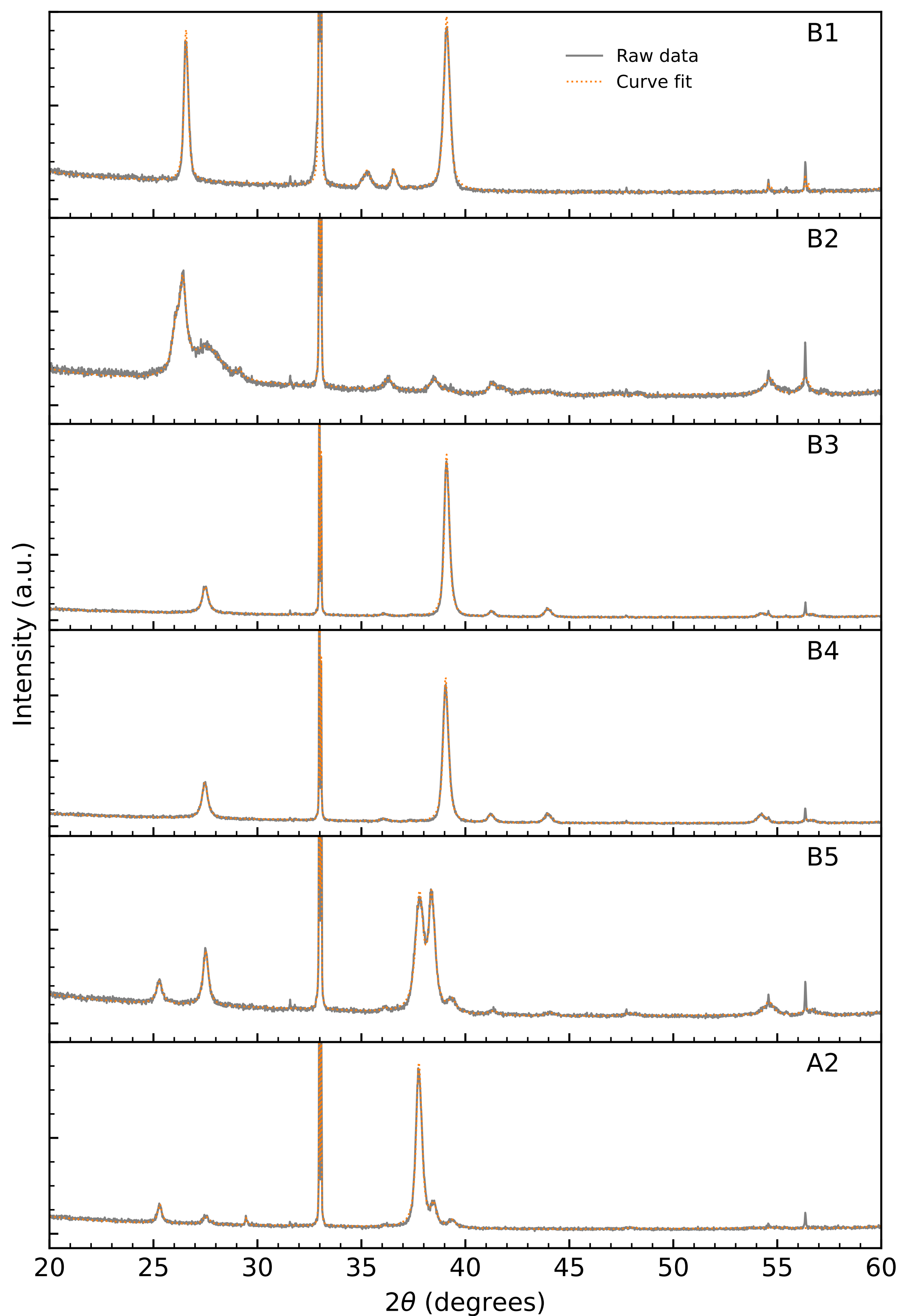

Figure 23: The curve fits, along with the raw data, performed for the samples on silicon substrates. The figure is only intended to display the agreement between fits and data. Revisit Fig. 21 for more details of the raw data.

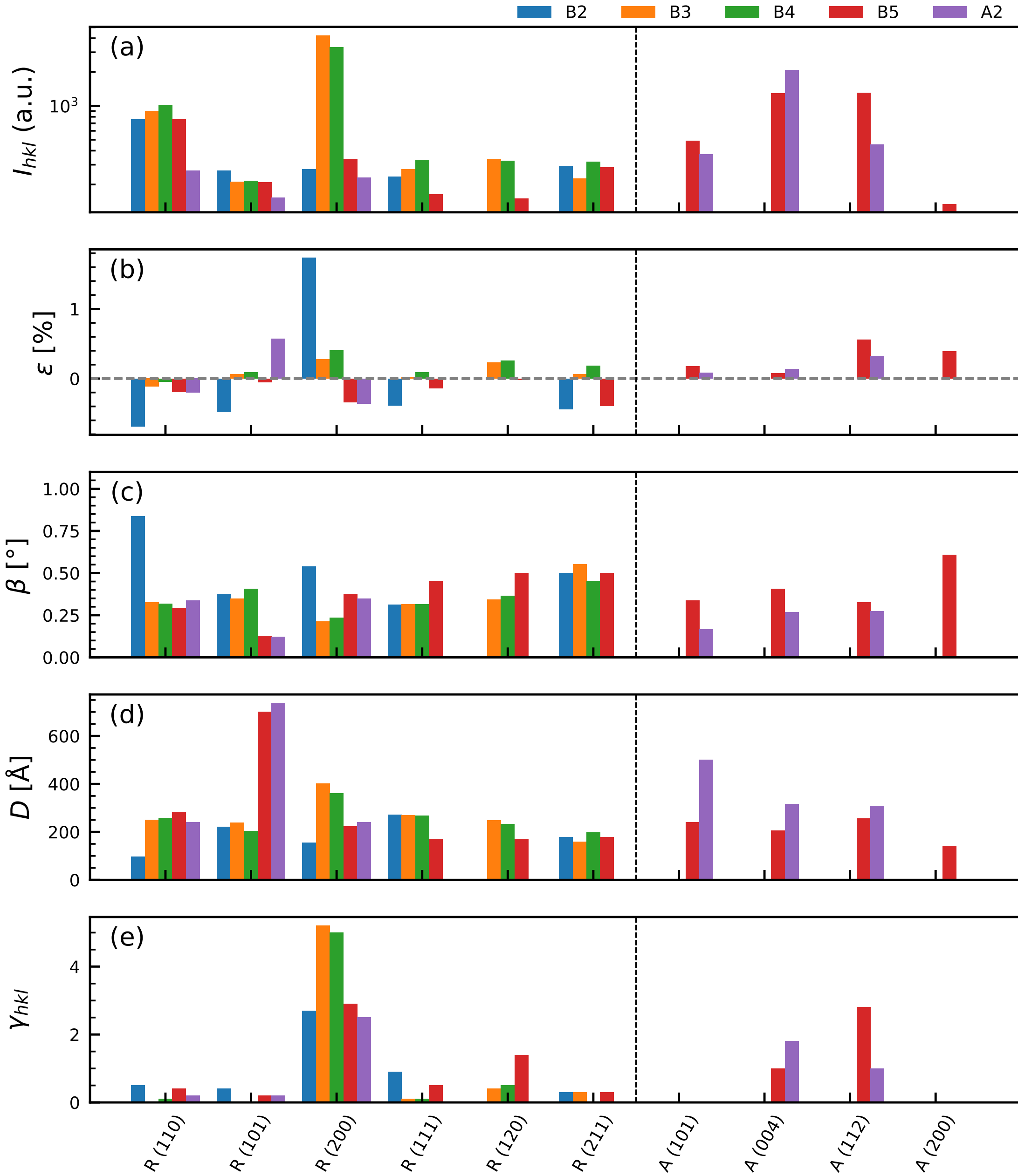

Figure 24: Quantitative θ–2θ data from the curve fits on the samples on Si substrates: (a) integrated intensity $\mathrm{I_{hkl}}$; (b) measured strain ϵ, (c) full-width-half-maximum β; (d) estimated crystallite size D; (e) texture coefficient γ_{hkl}. The black, dashed line separates rutile and anatase planes.

The samples were generally calculated to show little strain, with only the R (200) planes in sample B2 exceeding 1% tensile strain. B2 was calculated to have more strain than the other samples in general. Apart from this, it is difficult to assess whether a trend exists for strain in the rutile phase. The anatase phase on the other hand consistently displays tensile strain, although the strain values are all less than 1%.

The data of Figure 24 indicates some trends in terms of the estimated crystallite sizes. As seen for the rutile phase in Fig. 24 (d), the (200) planes gave the largest

estimate for samples B3 and B4. However, this trend did not translate into the other samples. As for the anatase phase, sample A2 consistently yielded larger mean crystallite size estimates for all registered peaks compared to sample B5.

As Fig. 24 (e) shows, the samples displayed a strong (100) preferred orientation for the rutile phase, as γ_{200} is considerably larger than the other rutile γ_{hkl}, for all samples. This is the case even for samples B5 and A2, where the rutile signal generally was weaker, although the γ_{200} for B5 and A2 (and B2) are not as large as for B3 and B4.

Although only a few anatase peaks were available, γ_{hkl} was also calculated for the anatase phase in samples B5 and A2, as shown in Figure 24 (e). The figure shows the strong preferred orientation for the anatase (004) and (112) planes. This demonstrates the usefulness of the texture coefficient in quantifying the degree of preferred orientation in a sample, as such an analysis would be difficult based on e.g. the intensities of Fig. 24 (a) alone. Note also that the figure shows how sample A2 is more strongly (001) textured than (112) textured, compared to sample B5.

5.1.2 GIXRD Measurements

A compilation of the GIXRD data along with curve fits for the films on Si substrates is shown in Figure 25. The data are plotted in a similar manner to the θ–2θ data, except for the inclusion of the curve fits. All samples were measured at an angle of incidence $\theta_i = 2.0°$ from $2\theta = 15°$ to $70°$, except for sample B5 which was measured at $\theta_i = 1.0°$ because of a problematic substrate signal.

Figure 25 displays patterns which in many ways resemble the patterns observed from the θ–2θ data of section 5.1.1. A clear difference is that all samples have considerably strong peaks in the 52°–56° range. Most of the activity in this range is attributed to the substrate, and so the peaks in this range will generally not be discussed. Note also that the rutile and anatase signatures generally resemble the powder diffraction pattern, missing the textures observed in Section 5.1.1. This is expected, as GIXRD measures orientations along a curve in reciprocal space, as was shown in Figure 4, and not parallel to the sample surface as in a θ–2θ measurement.

For samples B3, B4, B5 and A2, the results confirm that polycrystalline rutile with all orientations exist in the sample. This has implications for the discussion of growth mechanisms during deposition, as well as the texture observed in the θ–2θ measurements. This will be discussed in Section 5.5. For sample B2 the results further confirm that polycrystalline rutile indeed has grown in in the film, as all rutile (hkl) peaks below $2\theta = 60°$ are present.

The grazing incidence data also provide some insight into the unknown phases of sample B1. A peak can be seen at $2\theta \approx 39.5°$, and it is natural to attribute this to the same reflection that was observed at a similar 2θ angle in the θ–2θ measurements. This strongly suggests that the peak does *not* come from rutile (200), because if it did, one would not see this peak in grazing incidence without also seeing other rutile peaks. It is therefore attributed to substoichiometric TiO_2

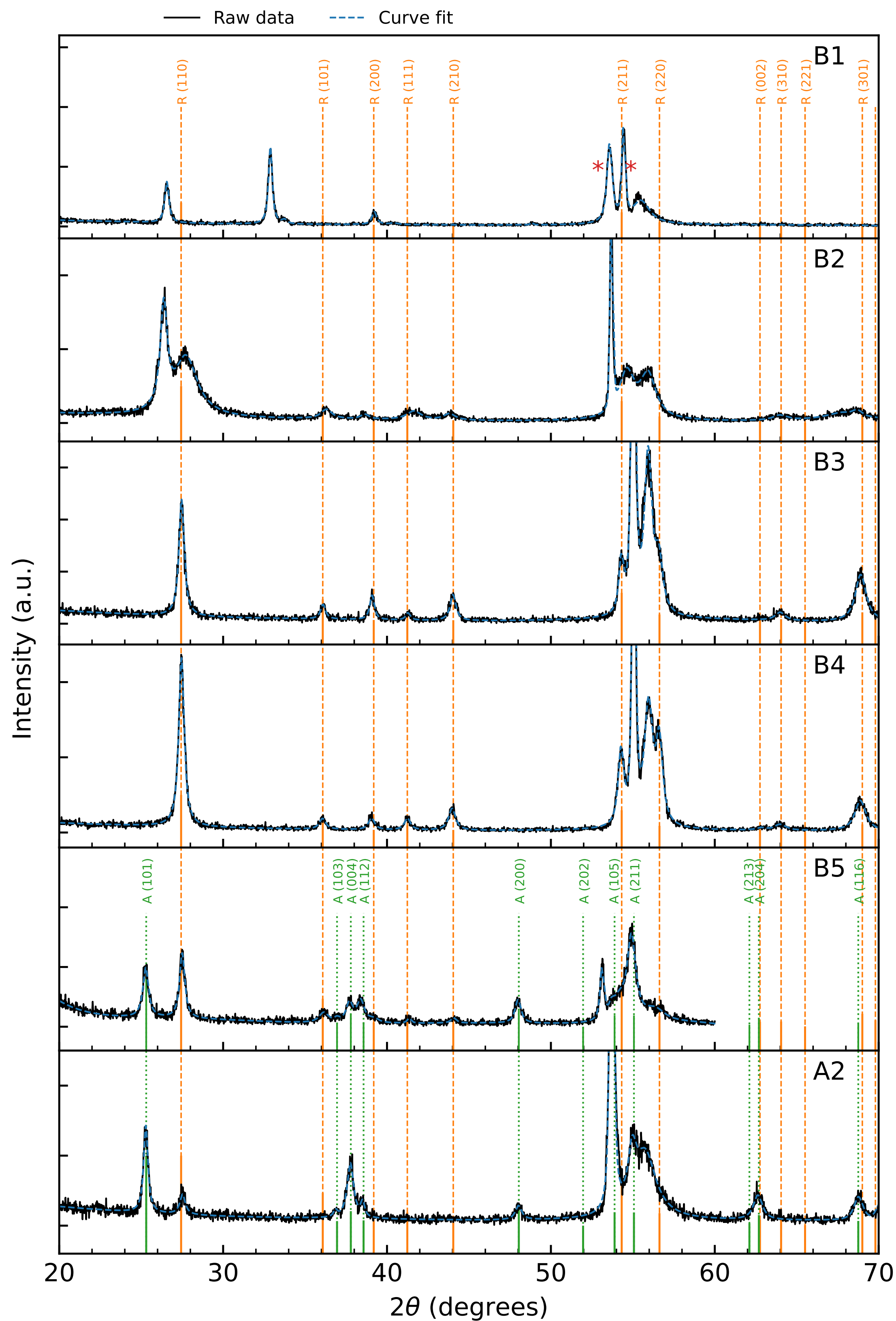

Figure 25: A compilation of GIXRD data and curve fits for the films on Si substrates. Substrate artifacts are denoted by red asterisks in the topmost plot. Reference peak locations and relative powder XRD intensities for rutile and anatase are shown in solid lines, with dashed lines to guide the eyes.

As for the peak at $2\theta \approx 26.3°$, which is seen for B1 and B2 in both figures 21 and 25, it seems that this is a characteristic peak for whatever phase it comes from. A similar argument can be made for the peak at $2\theta \approx 32.9°$, which also appears to have been present in the θ–2θ data, causing a broadening of the Si (200) substrate peak for sample B1 in Figure 21. It seems natural to attribute these peaks to substoichiometric TiO_2, as they do not fit with either the rutile or anatase XRD patterns.

Quantitative data analysis

The quantitative data extracted from the GIXRD curve fits for the films on Si substrates are displayed in Figure 26. The data are calculated and plotted in the samme manner as in Section 5.1.1. Note that γ_{hkl} was not included, as this parameter is not entirely meaningful when applied to GI data.

The data show some similarities with the θ–2θ results (Figure 24). As seen in Fig. 26 (b), sample B2 was calculated to display considerably more strain than the other samples, although the strain signs (+/-) vary between orientations. As for the other samples, strain for both rutile and anatase were calculated to be less than 1% for all peaks. Similar to the θ–2θ data, all anatase peaks indicated tensile stain in the anatase phase.

The mean crystallite size estimates seen in Fig. 26 (d) underline many of the previously discussed qualitative observations. The estimates for sample B2 are lower, being generally below 100 Å than for the other samples, indicating that the rutile quality is poor in sample B2. The estimates for B3, being in the 200–300 Å range, are generally larger than for B4.

The difference between D for the rutile (200) peak and the other peaks is not as large as it was for the θ–2θ data. This has implications for the growth mechanisms of rutile in these samples, and will be discussed in Section 5.5.

The estimates from the GI results are also similar to the θ–2θ results in that A2 generally gave larger crystallite size estimates for the anatase phase compared to B5.

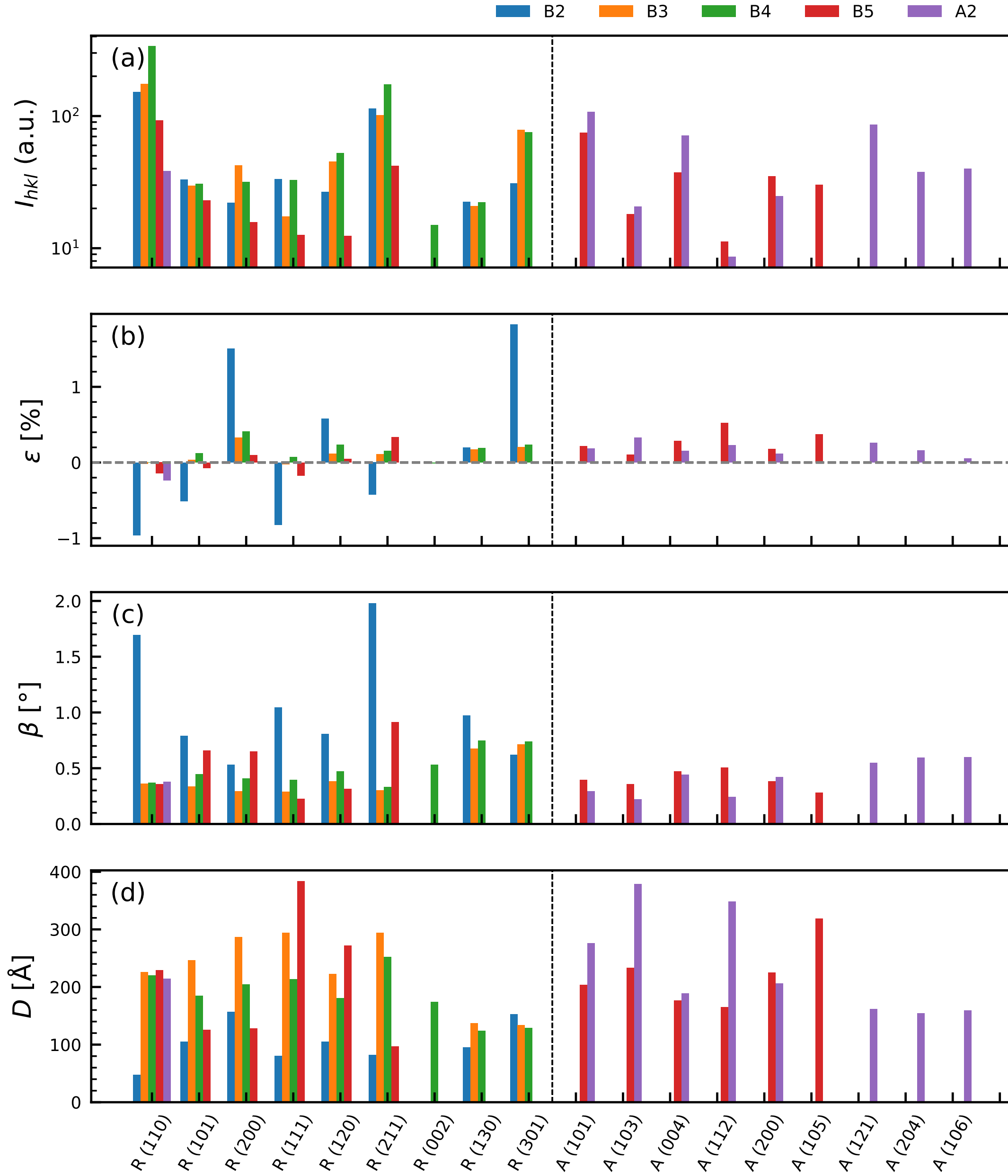

Figure 26: Quantitative GIXRD data from the curve fits on the samples on Si substrates: (a) integrated intensity I_{hkl}; (b) measured strain ϵ, (c) full-width-half-maximum β; (d) estimated crystallite size D. The black, dashed line separates rutile and anatase planes.

5.1.3 Raman Spectroscopy

The acquired Raman spectra for the samples on silicon substrates are shown in Figure 27. The data are plotted together with reference lines for the rutile and anatase spectra, as well as the silicon substrate signature, and are normalized to the strongest peak. Note that B5 on Si was damaged, and unavailable at the time the measurements were made. B5 is therefore missing from the data.

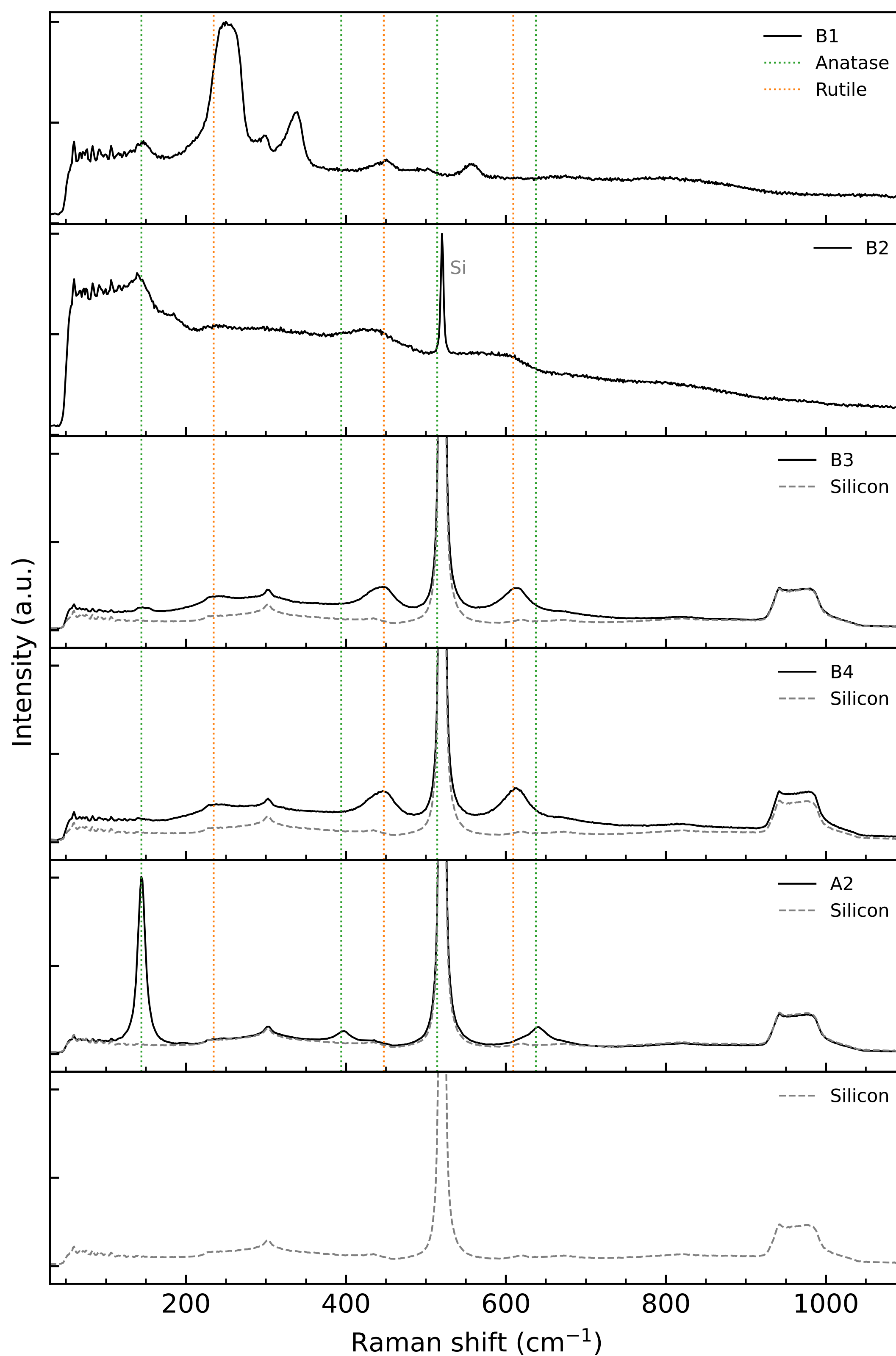

Figure 27: Raman spectra acquired for B1–B4 and A2 on Si substrates. Note that B5 is missing. Reference lines for the rutile (orange) and anatase (green) Raman spectra are shown. The substrate spectrum is also included where it is appropriate. A silicon peak is marked in the B2 plot.

In the figure, several peaks that differ from the substrate signature can be seen for each sample, indicating that they are signals from the film components. Some of these peaks align with either the rutile or anatase reference lines, suggesting that these peaks come from one of these two TiO_2 polymorphs. Furthermore, the peak locations and intensities are seen to vary between samples, indicating that the samples consist of different phases or structural compositions. The analysis will first focus on samples B3, B4, and A2, as these show the most clear traces of stoichiometric TiO_2.

Samples B3 and B4 display similar signatures in the Raman data. As indicated by the rutile reference lines in Figure 27, B3 and B4 both have peaks that agree well with the rutile reference peak locations, indicating existence of rutile in agreement with the XRD data discussion for these samples. In sample B3, a small peak can be seen at the anatase $144.3\,\mathrm{cm}^{-1}$ reference location, and a smaller peak still may be seen at the same location for sample B4. No anatase signal was detected in the XRD analysis for either sample, and so it is unclear whether or not this peak indeed stems from anatase.

Sample A2 displays a signature clearly resembling the anatase spectrum from Figure 9, which is also apparent when comparing with the reference lines in Figure 27. The ratio of these peaks also appear to agree well with the reference spectrum of Figure 9, where the $144.3\,\mathrm{cm}^{-1}$ peak is most intense, followed by the peaks at 637.5 and $394.1\,\mathrm{cm}^{-1}$. This underlines the indications from the XRD data of figures 21 and 25, which displayed polycrystalline anatase patterns for this sample.

Recall that rutile peaks were also found in the XRD data of sample A2 on Si. Based on the Raman spectrum in Figure 27 alone, it is difficult to distinguish any rutile peaks, but the XRD analysis was sufficiently conclusive in this regard.

The Raman spectra from samples B1 and B2 differ significantly from the other samples. The most obvious difference is the severe quenching of the silicon peaks, attributed to higher absorption (fewer photons scattered from substrate) in the films. Several peaks, particularly for sample B1, can be seen in Figure 27 which do not align with either rutile or anatase. When compared to the XRD data, it seems natural to attribute these to substoichiometric TiO_2. For B2, subtle traces of rutile at 447 and $609\,\mathrm{cm}^{-1}$ can be seen in Figure 27. This is in agreement with the XRD data from B2 on Si, where polycrystalline rutile of low crystalline quality was reported. Note also the peak at $144\,\mathrm{cm}^{-1}$ for both sample B1 and B2, which could indicate anatase.

Generally, the Raman spectroscopy confirm the suggestions made based on the XRD difractograms in the previous sections.

5.2 Uniform Undoped Samples on LAO (001)

5.2.1 Theta–2Theta Measurements

The θ–2θ results for the samples B1–B5 and A2 on LAO substrates are shown in Figure 28. Logarithmic plots of the same data are seen in Figure 29. The data are plotted in a similar manner as the samples on silicon substrates, with anatase and rutile peak locations shown wherever it is appropriate. The uncertainty in 2θ values is $\Delta_{2\theta} = \pm 0.007°$ owing to the 0.013° step size. Substrate artifacts from the contaminated Cu source are marked with asterisks, but otherwise do not interfere with the film signal.

Figure 28 shows characteristics for the films on LAO substrates which are noticeably different from the data for the films on Si substrates. In contrast to the powder XRD–like patterns observed for the films on Si substrates, the XRD data of the films on LAO generally show only a few film peaks, with much higher signal to noise ratio. This indicates that the samples consist of crystalline materials which are far more textured than what was found in the films on Si, as only a few orientations are prominent, with considerably higher intensities. Most of the film peaks seen in figures 28 and 29 agree well with ether rutile or anatase peak locations.

For sample B1 on LAO, a peak can be seen at $2\theta \approx 39°$, similar to B1 on Si. For B1 on Si this was suggested to come from either substoichiometric TiO_2. However, for B1 on LAO the peak intensity is much stronger.

From B2, a somewhat pronounced peak is observed at $2\theta \approx 38.4°$. The closest match with this peak is the anatase (112) peak location, with reference value at 0.1° above the measured peak value. A peak was also measured close to the (224) anatase reflection (not shown). Whether this in fact could come from anatase will be discussed along with the Raman data, to be presented in Section 5.2.3.

Samples B3 and B4 on LAO show clear differences from the same samples on silicon. As seen in Figure 28, a prominent peak can be observed at the anatase (004) peak location for both samples, which was not observed for the films on silicon in Section 5.1. This indicates that textured, (001)-oriented anatase exists in the samples. It is therefore suggested that the LAO substrate has “forced” the growth of anatase, even during conditions that yielded rutile on an amorphous surface, as was seen in for the films on silicon substrates.

A small peak can also be seen in Figure 28 at the rutile (200) location for samples B3 and B4 on LAO. The logarithmic plot of Figure 29 also reveals a weak polycrystalline rutile pattern for these samples. This shows that polycrystalline rutile with a (100) preferred orientation, similar to what was described for B3 and B4 on Si, coexists with the textured (001)-oriented anatase in samples B3 and B4 on LAO.

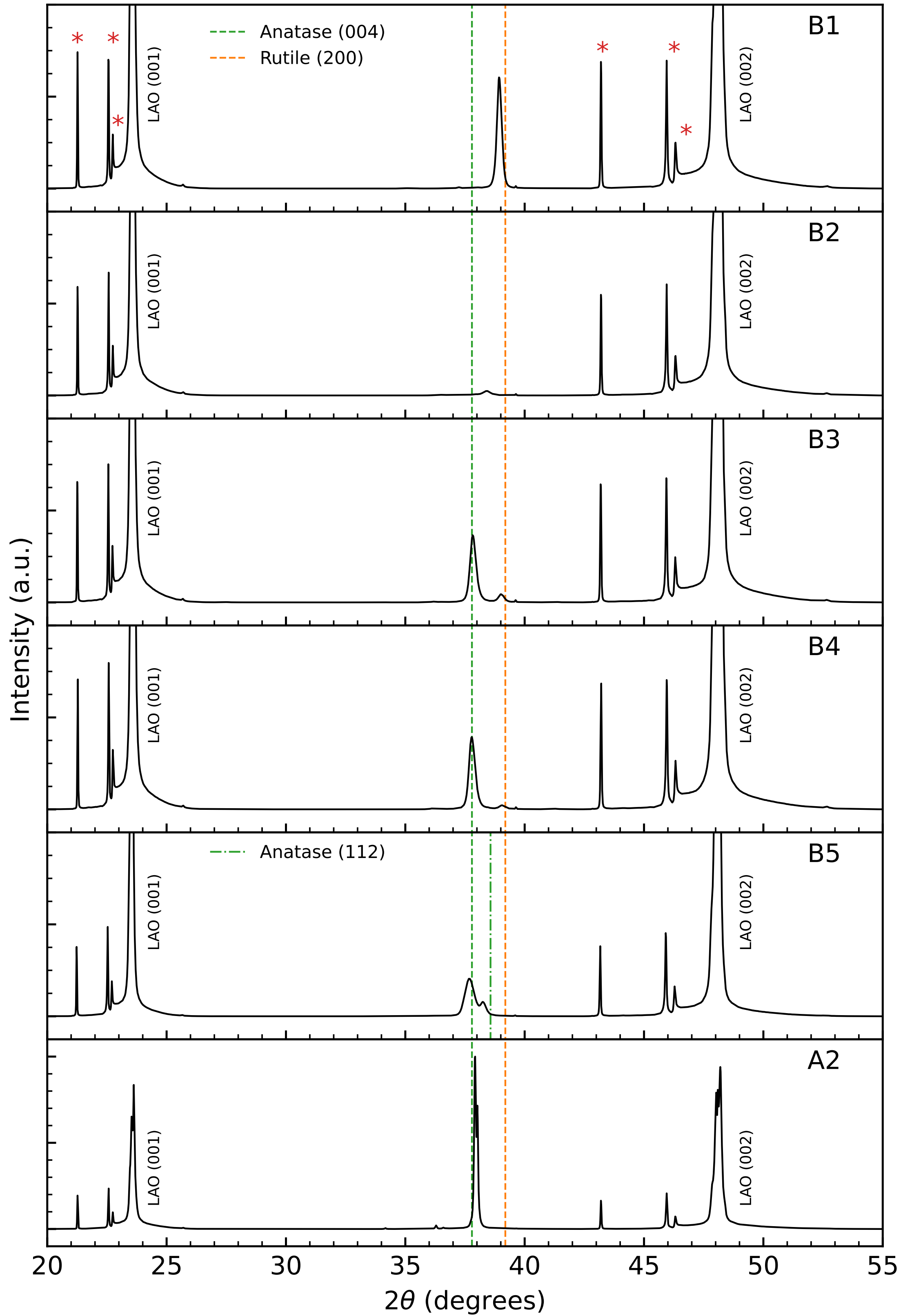

Figure 28: θ–2θ data for B1–B5 and A2 on LAO (001). The peak locations of anatase (004), anatase (112) and rutile (200) are shown where it is appropriate. In the topmost plot, substrate artifacts are marked by red asterisks.

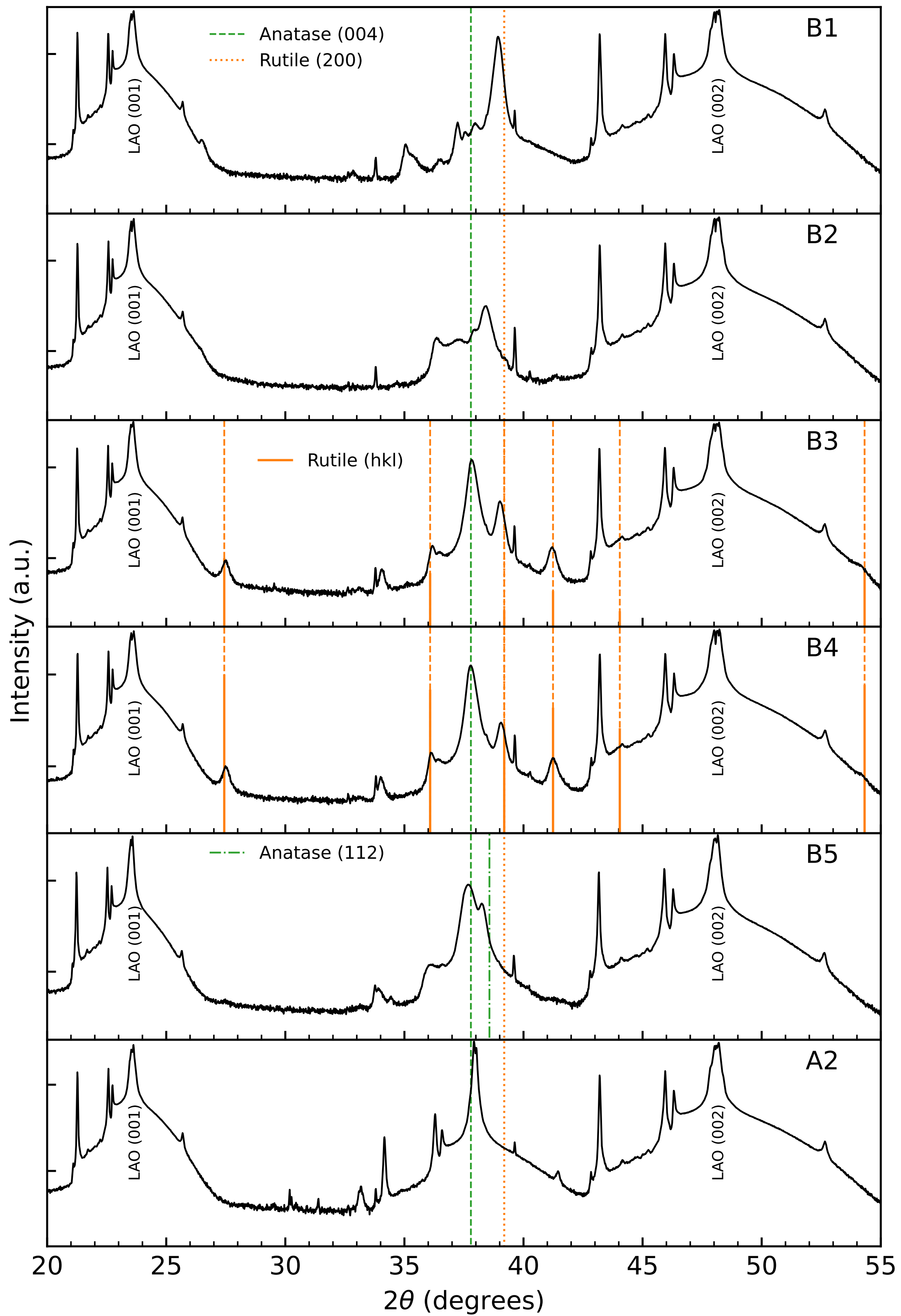

Figure 29: Logarithmic plot of the θ–2θ data for the films on LAO (001) substrates. Rutile and anatase reference peak positions are indicated by dashed and dotted lines. Note that a range of sharp substrate artifacts can be seen at several positions (see Fig. 28).

B5 on LAO displays two prominent peaks, similar to B5 on Si, attributed to A (004) and A (112). However, the signal is far stronger than what was measured from B5 on Si. As seen by comparing figures 21 and 28, the A (004) peak seems to dominate over the A (112) in the data from B5 on LAO, whereas in the data from B5 on Si, the peaks were more similar in intensity. Furthermore, no polycrystalline rutile pattern can be seen in the logarithmic plot of Fig. 29, in contrast to what was seen for B5 on Si.

Note also the absence of rutile (100) in B5 on LAO, which is not seen alongside the A (112) planes. Furthermore, the rutile (100) planes *are* seen in B3 and B4, where anatase (112) planes are not observed. It is suggested that the anatase–rutile transformation by nucleation of rutile (100) planes at anatase (112) twin boundaries [22] *has not* occured, and that a different growth mechanism has led to the observed (100) preferred orientation in rutile.

From sample A2, only one film peak is visible in figure 22, at the anatase (004) peak location. The intensity of this peak is seen to rival even the substrate peaks, and is in fact sufficiently sharp as to reproduce Kα_2 line. This suggests highly textured (001)-oriented anatase, with traits resembling that of epitaxial growth. Apart from this, no other TiO_2 peaks are seen. Recall that the data from A2 on Si indicated polycrystalline anatase with a strong (001) preferred orientation, in addition to polycrystalline rutile. It is suggested that the seemingly anatase (001)-favorable deposition parameters, in addition to the low lattice mismatch with anatase (001) and LAO, has led to pseudomorphic growth of anatase.

5.2.2 GIXRD Measurements

A compilation of the GIXRD scans for B1–B5 and A2 on LAO is shown in Figure 30, plotted in a similar manner as the films on silicon substrates in Section 5.1.1. Curve fits were only performed for samples B2–B5, as the remaining films did not have significant signal from other sources than the substrate. Calculated anatase or rutile powder XRD patterns are included wherever it is appropriate.

From the scan of B1 displayed in Figure 30, only a background and substrate signal is observed. Three peaks are observed between 2θ angles of 54° and 54°, and from comparison with the other samples, it is suggested that these peaks originate from the LAO substrate. The data constrasts with the data from B1 on Si, where several film peaks could be observed. It is suggested that the *crystalline* (i.e., not including amorphous) components in the film are highly textured, resulting in the prominent peak that was observed in the θ–2θ data of Figure 28. However, there could also be randomly oriented grains in the film, which may give off too weak signals to be detected.

The GIXRD data for samples B2, B3 and B4 on LAO all closely resemble the data from B2–4 on Si, and so the reader should revisit section 5.1.1 for discussion. Note however that although samples B3 and B4 on LAO displayed (001)-oriented anatase in Figure 28, no anatase peaks are seen in the GIXRD plot, where only a polycrystalline rutile pattern is present. This indicates that all of the anatase

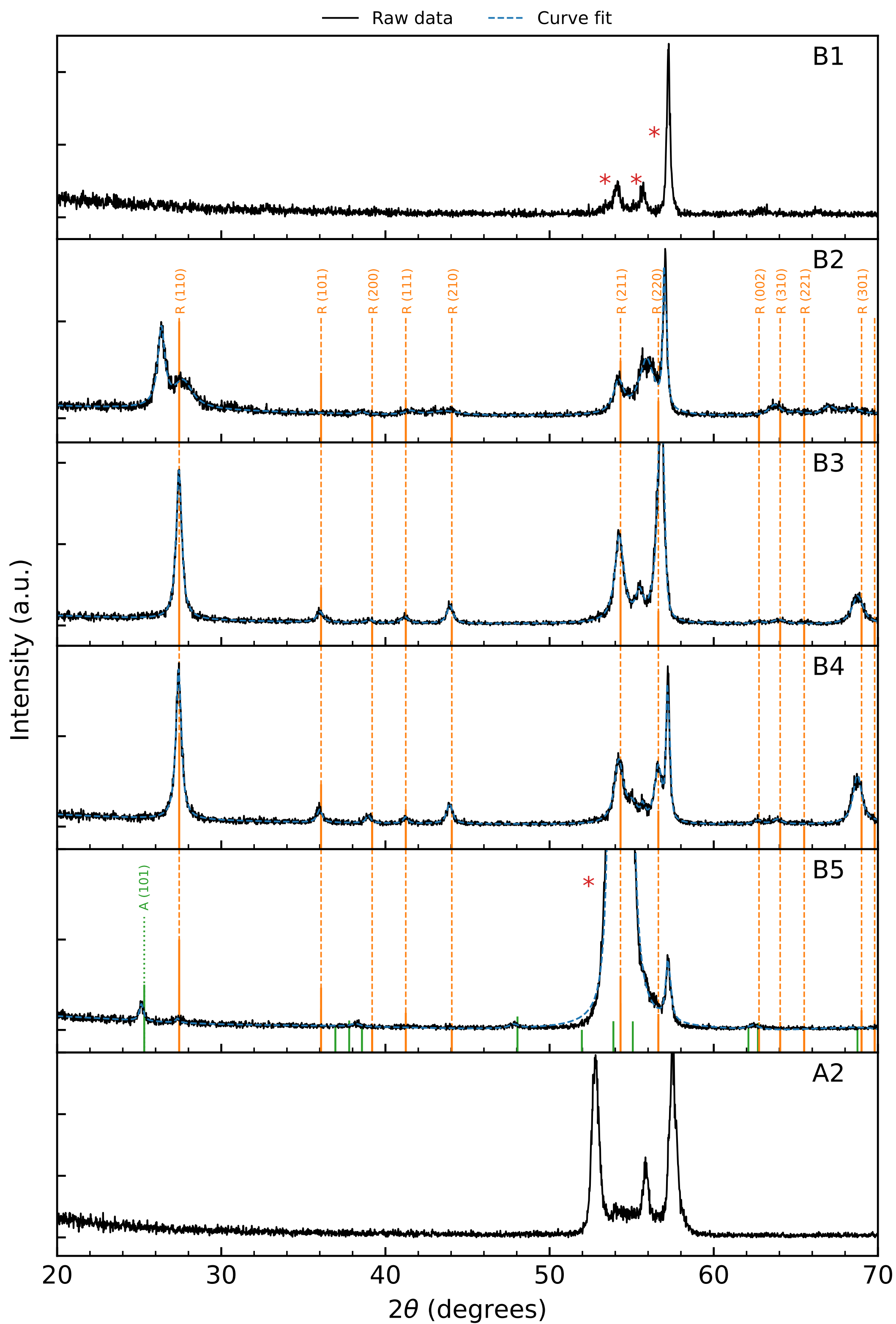

Figure 30: A compilation of GIXRD data and curve fits for the films on LAO (001) substrates. Substrate artifacts are denoted by red asterisks in the topmost plot, as well as in B5. Reference peak locations and relative powder XRD intensities for rutile and anatase are shown in solid lines, with dashed lines to guide the eyes.

so far observed from B3 and B4 on LAO is (001)-oriented, and that textured anatase coexists with polycrystalline, powder–like rutile.

The GIXRD data from sample B5 on LAO is somewhat different from B5 on Si. In contrast to B5 on Si where a clear polycrystalline rutile pattern could be seen (Figure 25), only a faint R (110) peak at $2\theta \approx 27.4°$ is visible from sample B5 on LAO in Figure 30.

Traces of polycrystalline anatase in B5 on LAO are also visible, most evidently from the A (101) peak at $2\theta \approx 25.3°$. The base of a large peak may also be seen at $2\theta \approx 54°$, and this is likely to be an artifact of the textured, (001)-oriented anatase in the film.

In sample A2, no polycrystalline pattern can be seen in 30. It is therefore suggested that all anatase observed in the sample is highly textured, which agrees with the high crystalline quality found for the anatase (004) peak in section 5.2.1.

Quantitative data analysis

The quantitative data extracted from the GIXRD curve fits of the LAO samples are shown in Figure 31. The data are plotted in the same manner as in figures 24 and 26 of Section 5.1.

The data somewhat resembles the data from the films on Si substrates. Note however from Fig. 31 (a) that, in genereal, fewer peaks are attributed to the anatase phase compared with the films on Si. An interpretation of this is that the anatase is less polycrystalline/powder–like in the films on LAO compared with the films on Si, where more anatase peaks were observed.

As seen in Fig. 31 (b), the strain values are generally small. For B2 on LAO, the strain values were calculated to be negligibly small, in stark contrast to what was found for B2 on Si. However, the rutile peak signals in B2 on LAO were considerably weak, so it is likely that this simply resulted in a poor fit which did not yield reasonable results. Apart from this, the strain trends appear similar to what was found for the films on Si.

The estimated mean crystallite sizes, seen in Fig. 31 (c), are generally smaller for B3 than for B4, in contrast to what was seen in Figure 26 for B3 and B4 on Si. Apart from this, the relative estimates follow a similar trend to the films on Si, but the estimates for the LAO samples are also generally lower than for the Si samples.

For sample B5, the anatase phase dominates, which can be observed qualitatively in Figure 30 and is also apparent from Fig. 31 (a). Note however that the crystalline quality of the anatase phase in B5 appears to be in the same range as the rutile phase in B3 and B4, with little strain and crystallite size estimates in the 100–300 Å range.

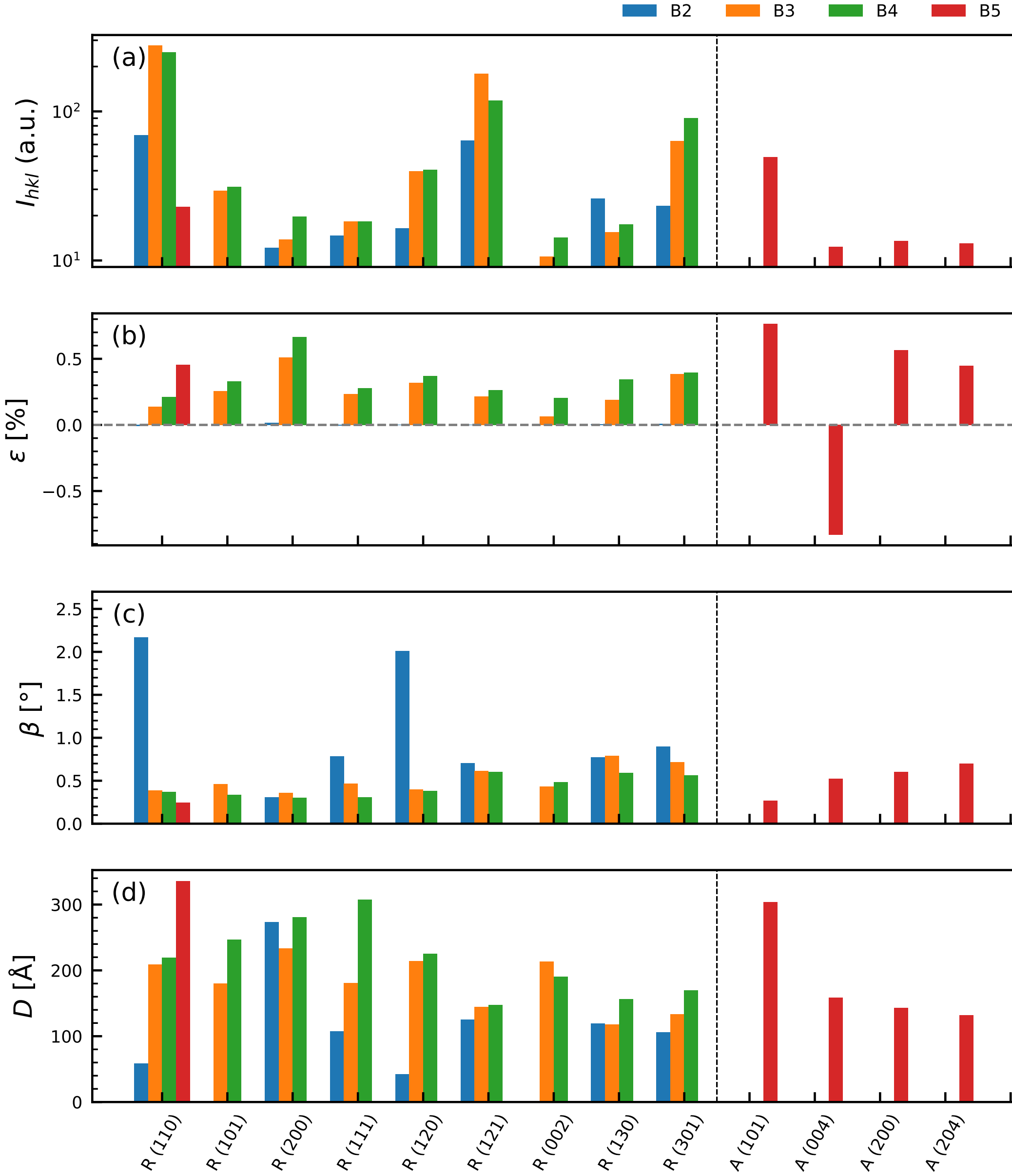

Figure 31: Quantitative GIXRD data from the curve fits on the samples on LAO substrates: (a) integrated intensity I_{hkl}; (b) calculated strain ϵ, (c) full-width-half-maximum β; (d) estimated crystallite size D. The black, dashed line separates rutile and anatase planes.

5.2.3 Raman Spectroscopy

The acquired Raman spectra for the samples on LAO substrates are shown in Figure 32. Similar to in Section 5.1.3, the data are plotted along with the substrate signature as well as reference lines for the rutile and anatase spectra, all normalized to the strongest peak.

Sample B1 on LAO appears similar to B1 on Si. The only noteworthy difference is that the peak at the rutile 234.6 cm^{-1} peak location is considerably sharper

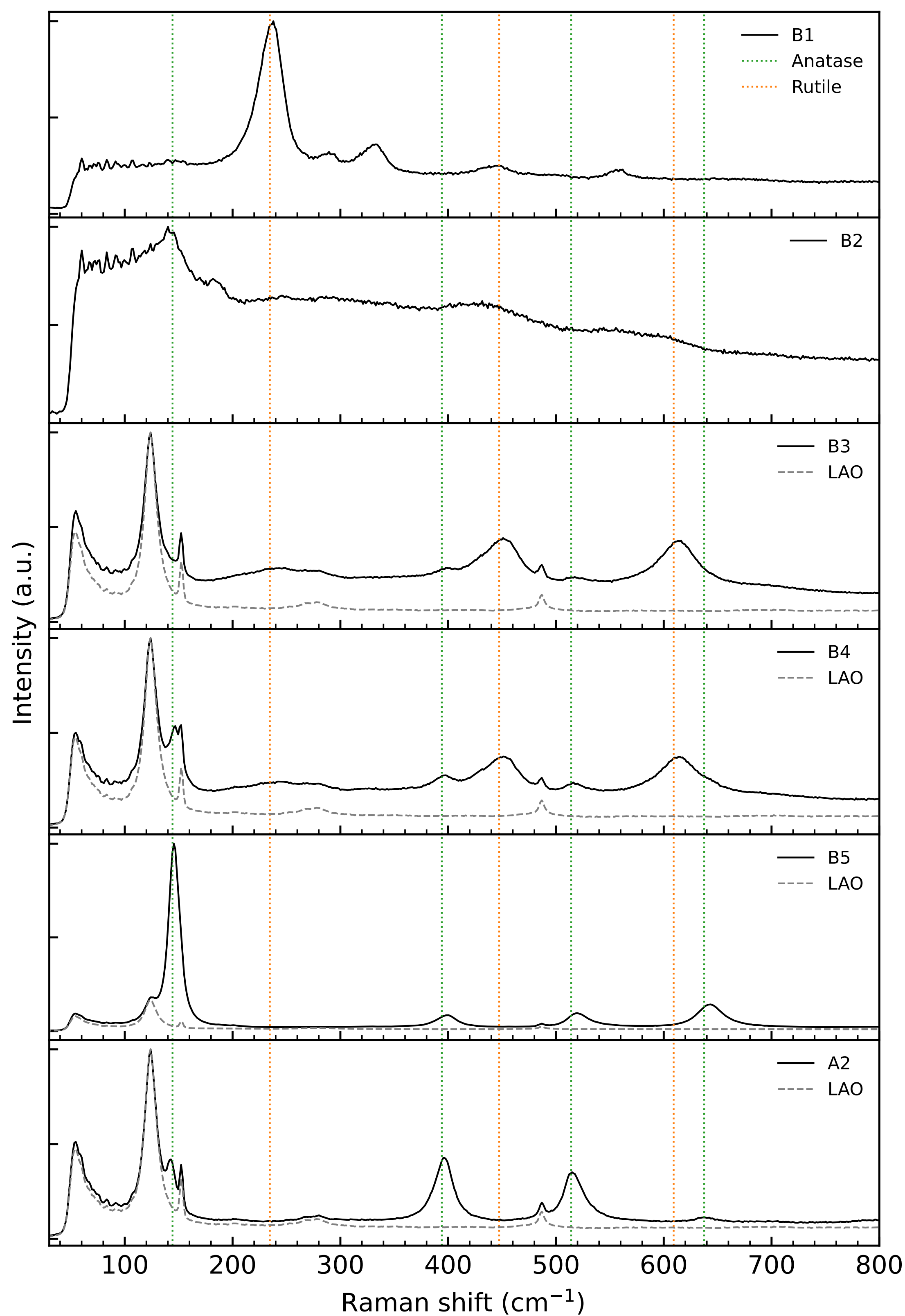

Figure 32: Raman spectra acquired for B1–B5 and A2 on LAO substrates. Reference lines for the rutile (orange) and anatase (green) Raman spectra are shown. The substrate Raman spectrum is also included where it is appropriate.

for B1 on LAO than B1 on Si, which is apparent when comparing figures 27 and 32. This could indicate that this Raman shift peak indeed comes from the same phase which gave the XRD peak at $2\theta \approx 39°$, and that this indeed comes from (100)-oriented rutile. However, the strongest peak of the rutile Raman spectrum, which would be found at $609.2\,\text{cm}^{-1}$, is not observed. It is therefore suggested that sample consists of a non–TiO_2 phase, similarly to B1 on Si.

For B2 on LAO, the Raman spectrum is hardly different from B2 on Si, similar to what was seen for the XRD data. Note the peak at the $144.3\,\text{cm}^{-1}$ anatase peak location, which could indicate anatase, as was also slightly indicated by the θ–2θ data. However, no other anatase peak can be seen, so no conclusion is drawn.

Samples B3 and B4 on LAO also resemble B3 and B4 on Si, in that a clear rutile signature can be seen in Figure 32. However, they differ from the films on Si in that peaks can also be seen at the anatase reference spectrum locations. A comparison of the Raman spectra for B3 and B4 is shown in Figure 33. For sample B3, two peaks at 394 and $514\,\text{cm}^{-1}$ anatase peak locations can be distinguished. For sample B4, the same peaks are even more pronounced, and a strong peak can be clearly distinguished from the substrate peaks at the $144.3\,\text{cm}^{-1}$ anatase peak location. The results for both samples support the suggestion of highly textured, (001)-oriented anatase based on the θ–2θ diffractometry. Furthermore, the anatase signature in B4 is generally more pronounced than in B3.

As seen in Figure 32, the Raman spectrum from sample B5 resembles the anatase reference spectrum from Figure 9. The film signal intensity is also substantially stronger than the substrate signal. The results indicate a large presence of anatase, in good agreement with what was suggested from the XRD discussion in sections 5.2.1 and 5.2.2.

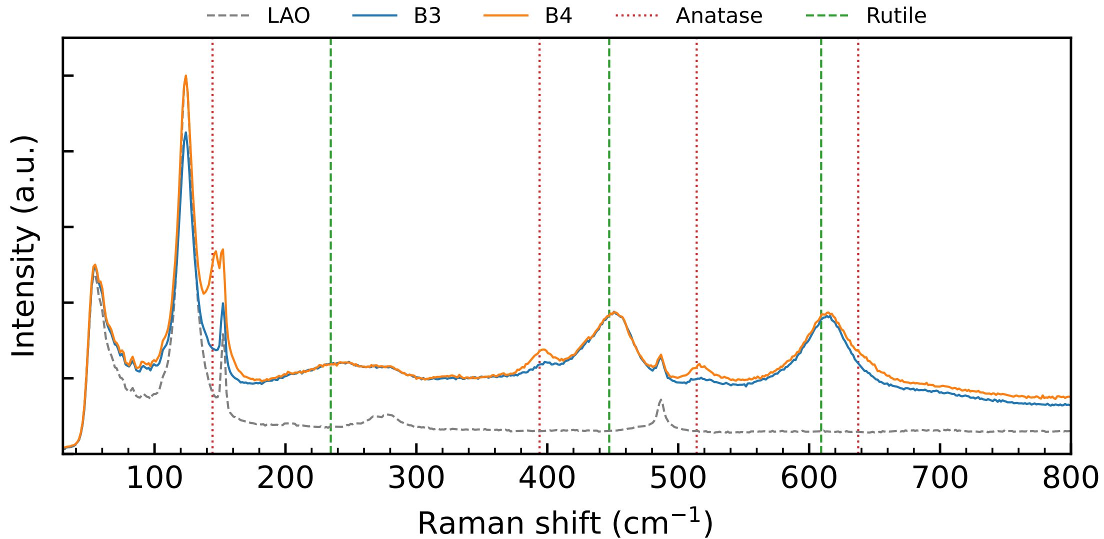

Figure 33: Compilation of the Raman spectra acquired for B3 and B4 on LAO. References for the rutile and anatase spectra, as well as the LAO spectrum, are included.

Sample A2 also shows peaks aligning with the anatase reference spectrum. Compared to sample B5, the signal does not dominate over the substrate signature, but this may simply be explained by the fact that sample A2 is significantly thinner than B5 (229 nm compared to 687 nm, as in Table 5). A more noteworthy observation is that the peak intensity ratios for A2 on LAO qualitatively differ from both B5 on LAO, as well as from A2 on silicon, which was displayed in Fig. 27. Note that the latter two samples closely resembled the reference anatase spectrum of Figure 9, where the peak at 144.3 cm^{-1} dominates. However, in Figure 32 the peak at 394 cm^{-1} dominates the A2 anatase spectrum.

It is suggested that the difference in Raman peak intesity ratios between A2 on LAO and A2 on Si, as well as B5 on LAO, is due to the fact that A2 on LAO *only* shows the (001) orientation, whereas for B5 on LAO and A2 on silicon, polycrystalline anatase with various orientations was observed.

5.2.4 HRXRD Measurements

The results of the high resolution X-ray diffraction for B3–B5 and A2 on LAO are shown from top to bottom in Figure 34. The left subfigure displays the ω–2θ scan of the anatase (004) peaks, while the right subfigure displays the rocking curve scans of the same peak. The bulk A (004) 2θ value is also shown.

The peaks were all fitted using split pseudo-Voigt functions (Eq. (6)) in order to represent the asymmetry of the peaks. The curve fits for the ω–2θ scans are included with the raw data. The quantitative data results from the curve fits are given in Table 9. See the table text for explanations of the parameters.

All peaks from the ω–2θ scan in Figure 34 are seen to be shifted to lower angles. This indicates tensile strain, which is represented as ϵ in Table 9. The strain increases from sample B3 to B4 and B5. Referring to the deposition parameters of the B-series, recall that B3, B4 and B5 had increasing levels of oxygen pressure. It is suggested that there is a correlation between the oxygen pressure during deposition, and the resulting strain of the film. In this case, it would suggest that increasing oxygen pressure leads to increased tensile strain of the anatase (001) planes. Notice also from both Table 9 that A2 was calculated to show considerably less strain than the B–samples. Although A2 was deposited with a higher oxygen pressure than the B–samples, it was also deposited using a lower laser fluence, in addition to being a thinner film. It is therefore difficult to separate which parameters lead to lower strain for the A2 sample.

Table 9: Quantitative data from the curve fits on the A (004) peaks, for the films on LAO substrates: peak value 2θ; calculated d-spacing d; calculated strain ϵ, FWHM β; estimated mean crystallite size D; asymmetry parameter h/l; Lorentzian fraction η.

Sample	2θ	d [Å]	ϵ [%]	β (°)	D [nm]	h/l	η
B3	37.67	2.386	0.312	0.129	62 ±2	1.133	0.36
B4	37.60	2.391	0.522	0.101	73 ±3	1.0	0.53
B5	37.37	2.404	1.069	0.175	46 ±1	2.826	0.22
A2	37.73	2.382	0.144	0.054	149 ±10	1.5	0.15

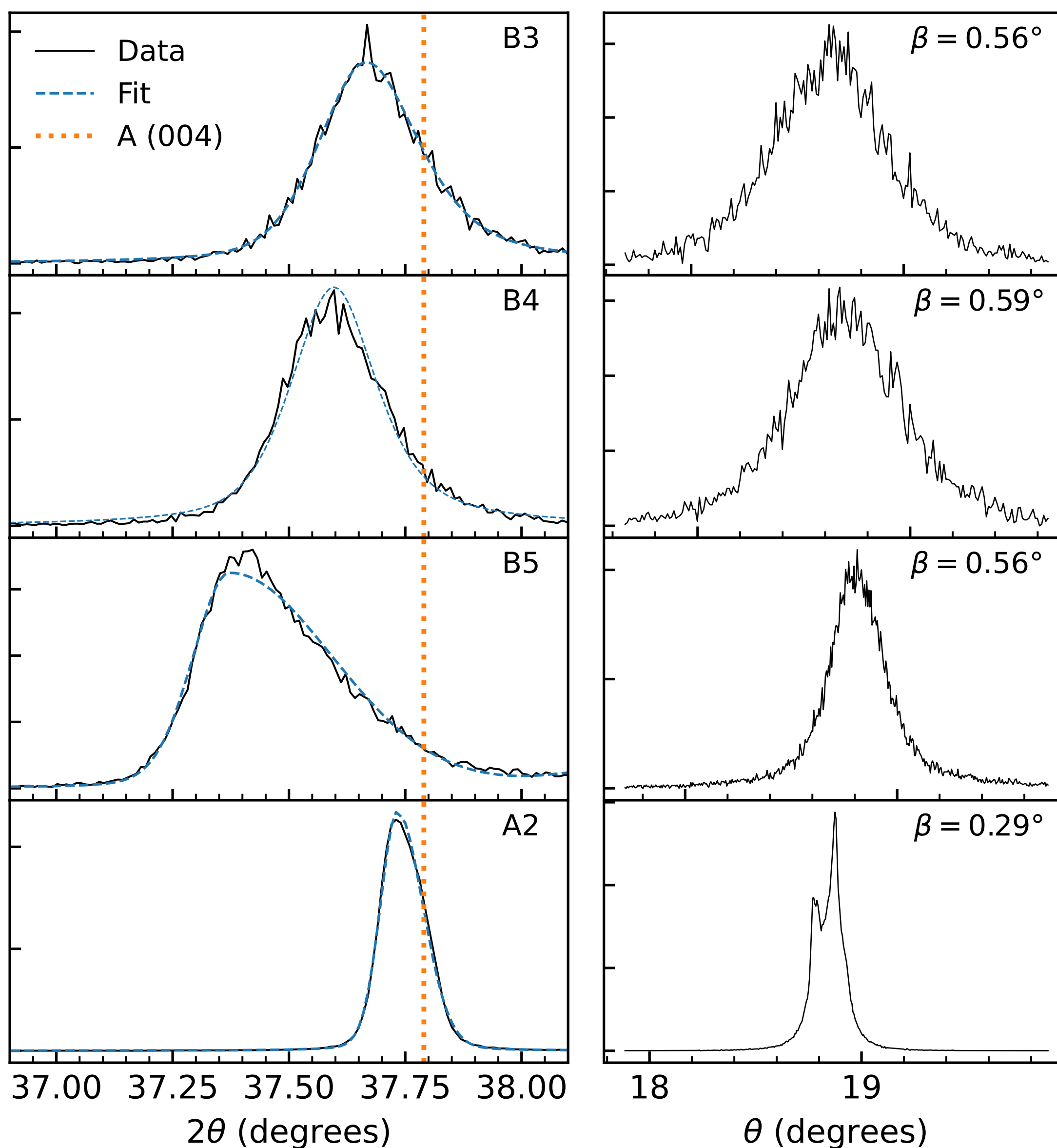

Figure 34: HRXRD diffractograms for B3–B5 and A2 on LAO (001): (left) ω–2θ scans of the anatase (004) peaks, with curve fits. The bulk anatase (004) peak location is shown; (right) rocking curves of the anatase (004) peaks.

In addition to the ω–2θ peaks being shifted, they are also noticeably asymmetric. The asymmetry parameters h/l (PV_{high}/PV_{low} from Eq. (6)) are 1.13, 1.00, and 2.28 for B3, B4 and B5, respectively. Although B4 was fitted with *no* asymmetry, this might be the result of a poor fit, as B4 can be seen to show some asymmetry from qualitative inspection of Figure 34. The asymmetry is most prominent in B5, which also displays the highest peak shift. Notice also that A2 is considerably less asymmetric than B5.

The exact nature of the strain is unknown. The fact that the peaks are skewed *towards* the bulk 2θ value could indicate that strain relaxation occurs in the film. It could also be that the planes are initially relaxed and are subsequently more strained further from the substrate. In any case, the peak shapes are consistent with there being a distribution of anatase (001) d–spacing values, resembling the example from Fig. 14.

The mean estimated crystallite size for B5 was lower than for B3 and B4. This is somewhat unexpected, as the deposition parameters of B5 were found in Section 5.1 to favor anatase growth, while B3 and B4 favored rutile. However, peak broadening from strain was *not* accounted when Eq. 9 was used (only instrumental broadening was accounted for). Since B5 appears to be more strained and less symmetric, it is plausible that D is considerably underestimated, as β_{size} from Eq. (17) might in reality be much smaller.

The mean crystallite size estimate for A2 was 149 ± 10 nm. Recall that the thickness of A2 was measured to 229 nm. This indicates that a substantial fraction of the film height is comprised of uninterrupted crystallites (without grain boundaries). It is therefore suggested that the low lattice mismatch between LAO and anatase has indeed yielded pseudomorphic/epitaxial–like growth.

Some trends can be seen from the rocking curves of Figure 34. The rocking curves of B3 and B4 on LAO are similar, both in intensity and FWHM (β). B5 displays a similar FWHM but higher intensity (which is observed through the lower signal–noise ratio). The FWHM of A2 is substantially lower than the others, indicating a high crystalline quality of the anatase phase in A2. This is despite the fact that the rocking curve of A2 shows several distinct peaks, which are suggested to be effects of the planes growing parallel to the twin domains of the LAO substrates. This further indicates that uninterrupted (no grain boundaries) crystal growth has occurred in A2 on LAO.

5.3 Uniform Undoped Samples on STO (001)

5.3.1 Theta–2Theta Measurements

The results of the θ–2θ scans for B1–B5 and A2 on STO substrates are shown in Figure 35, with a logarithmic-scale plot of the same data appearing in Figure 36. Calculated anatase and rutile peak locations are included wherever it is appropriate.

Similar to the LAO data, Figure 35 displays several substrate artifacts for each sample, which are marked with asterisks. In addition to this, prominent, single peaks are visible from B3–B5 and A2, resembling the characteristics of highly textured materials.

From sample B1 in Figure 36, two peaks can be seen at approximately 40.3° and 42.3°. Neither of these can be assigned to rutile or anatase, suggesting that a different phase exists in the film. The deposition parameters for B1 are known from the discussions in sections 5.1 and 5.2 to not favor stoichiometric TiO_2.

However, from B1 on STO in Figure 36, a peak can *also* be seen at the anatase (004) peak location, indicating that the STO substrate might have been able to “force” anatase (001) growth, in agreement with ref. [47]. This also applies for sample B2 on STO, for which a peak at the anatase (004) location can be seen, but otherwise the data resembles the B1 films on Si on LAO substrates.

For B3–B4 and A2, the data qualitatively resemble the data from the films on LAO in Section 5.2. That is: polycrystalline rutile along with textured anatase is suggested to exist in the mentioned samples on STO. A difference from the films on LAO is that a prominent A (112) peak is *not* observed on sample B5 on STO, and that the A (004) peak on A2 on STO is broader than for A2 on LAO (which results in the $K\alpha_2$ line not being visible).

The results are generally in somewhat agreement with ref. [47], where anatase (001) films were grown on STO in O_2 ambience almost regardless of substrate temperature and O_2 pressure. This was attributed to the low lattice mismatch of approximately 3%.

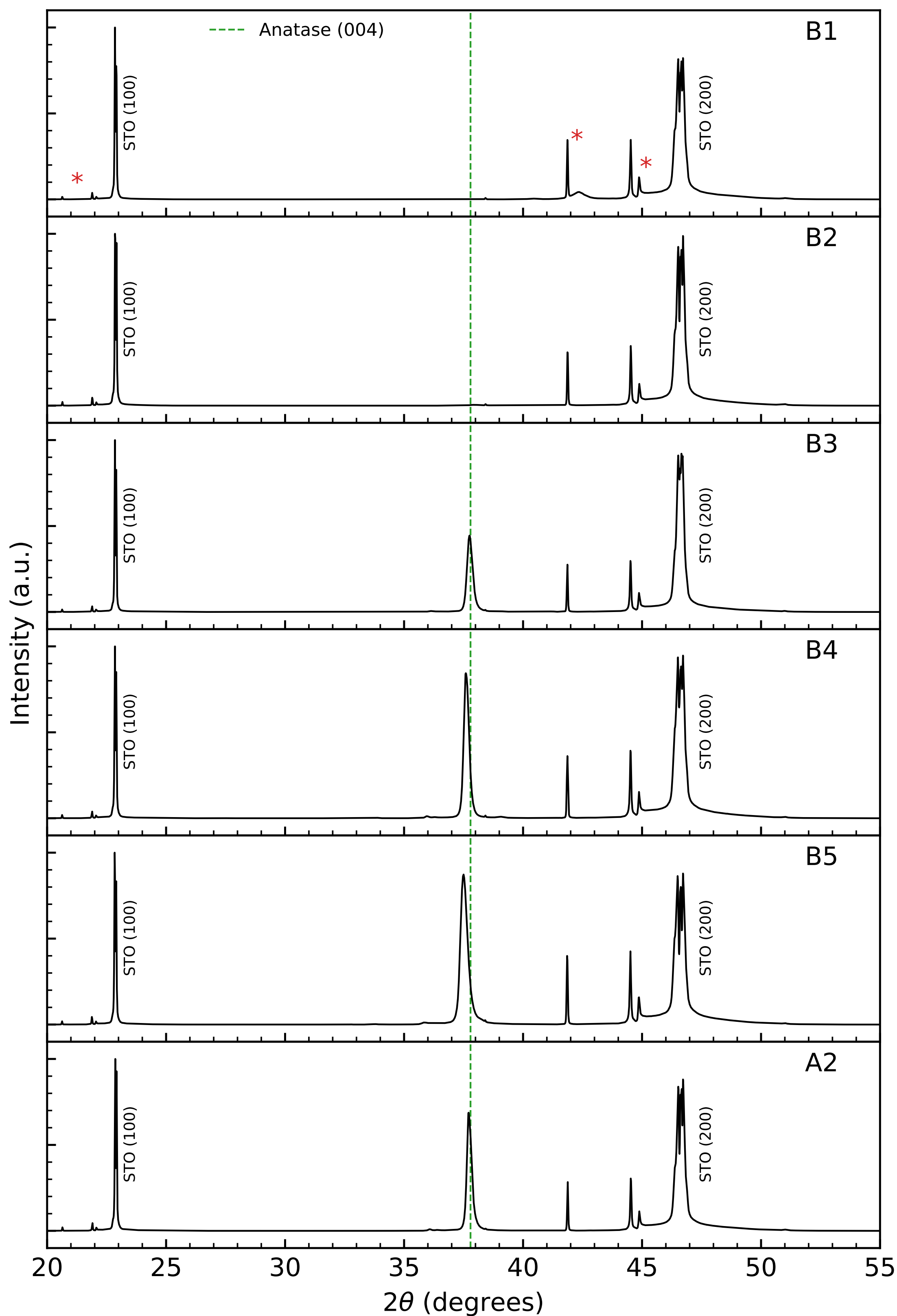

Figure 35: θ–2θ data for B1–B5 and A2 on STO (001). The peak locations and relative powder XRD intensities for rutile and anatase are shown in solid lines, with dashed lines to guide the eyes. In the topmost plot, substrate artifacts are marked by red asterisks.

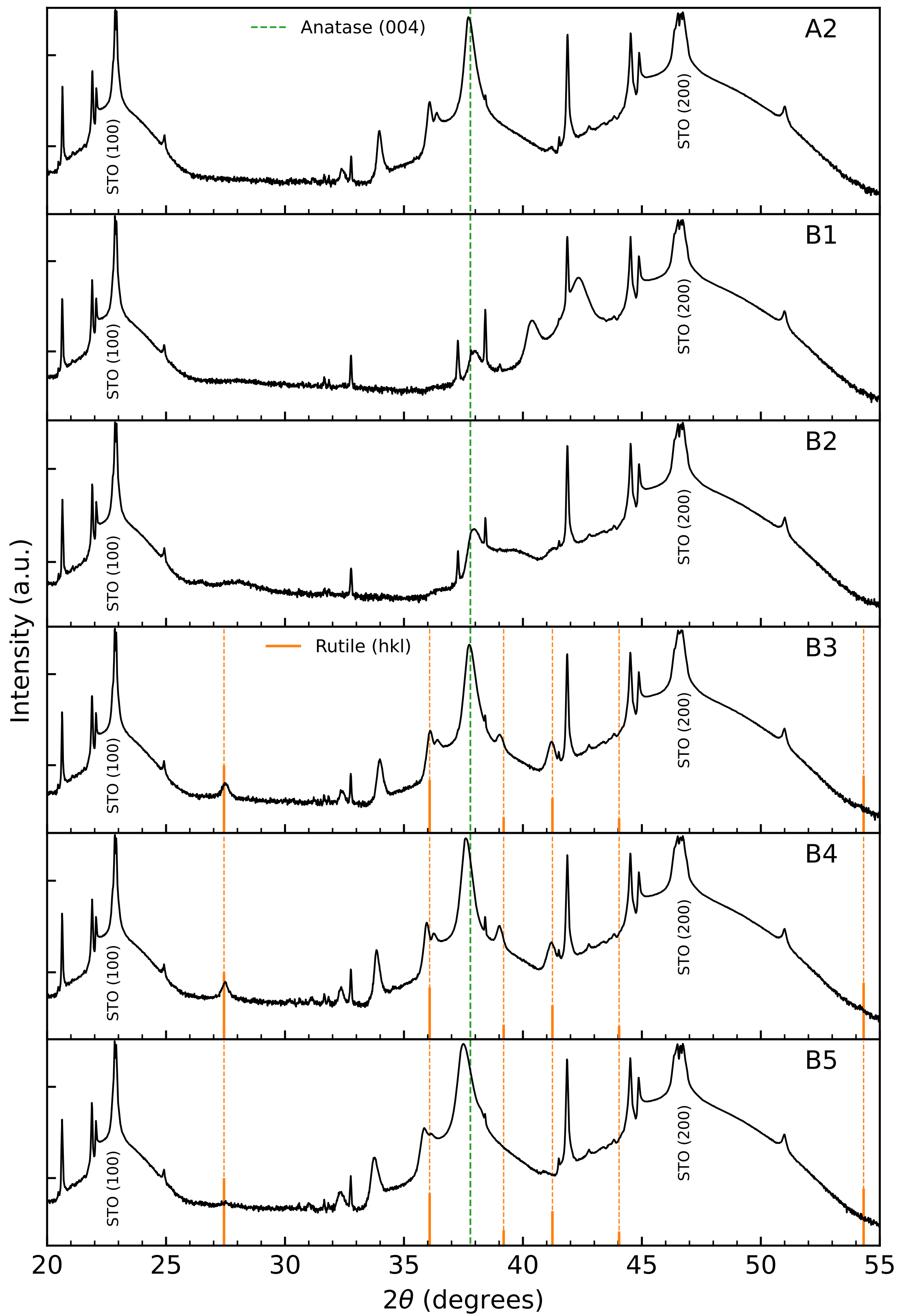

Figure 36: Logarithmic scale plot of the θ–2θ data for B1–B5 and A2 on STO (001). See Fig. 35 for indication of substrate artifacts.

5.3.2 GIXRD Measurements

A compilation of the GIXRD data for B1–B5 and A2 on STO is shown in Figure 37, plotted in a similar manner as in previous sections. All samples were curve fitted except for A2, which only showed a peak assumed to be an artifact of either the substrate or the highly textured component of the film.

Apart from the substrate artifacts, samples B2–B5 and A2 appear almost identical to the same films on LAO. The reader should therefore revisit Section 5.2.2 for discussion of these samples.

A clear difference between B1 on STO and B1 on LAO, however, is that B1 on STO features several peaks. The pattern does not resemble either the rutile or anatase powder diffraction patterns. It is also different from the pattern observed on B1 on Si. This indicates that a different phase from stoichiometric TiO_2 exists in the film, but no further attention will be devoted to this.

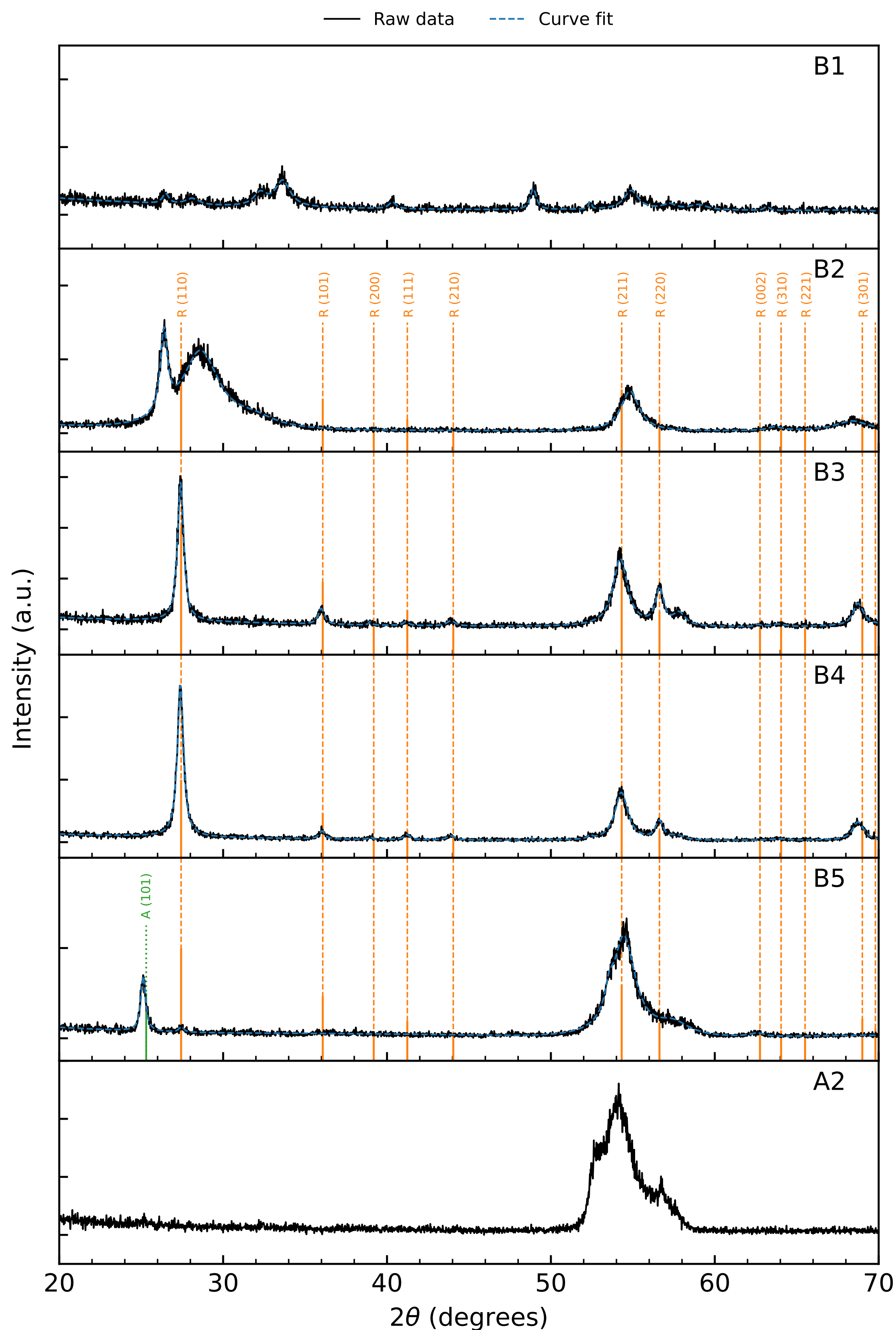

Figure 37: A compilation of GIXRD data and curve fits for the films on STO substrates. Reference peak locations and relative powder XRD intensities for rutile and anatase are shown in solid lines, with dashed lines to guide the eyes.

Quantitative data analysis

The quantitative data resulting from the curve fits are displayed in Figure 38. The results are generally similar to the quantitative data from films the on LAO. A clear difference, however, is that only one anatase peak was identified for sample B5 on STO, whereas several were identified for B5 on LAO. A possible explanation is that the anatase signal in B5 on STO is simply weaker than for B5 on LAO.

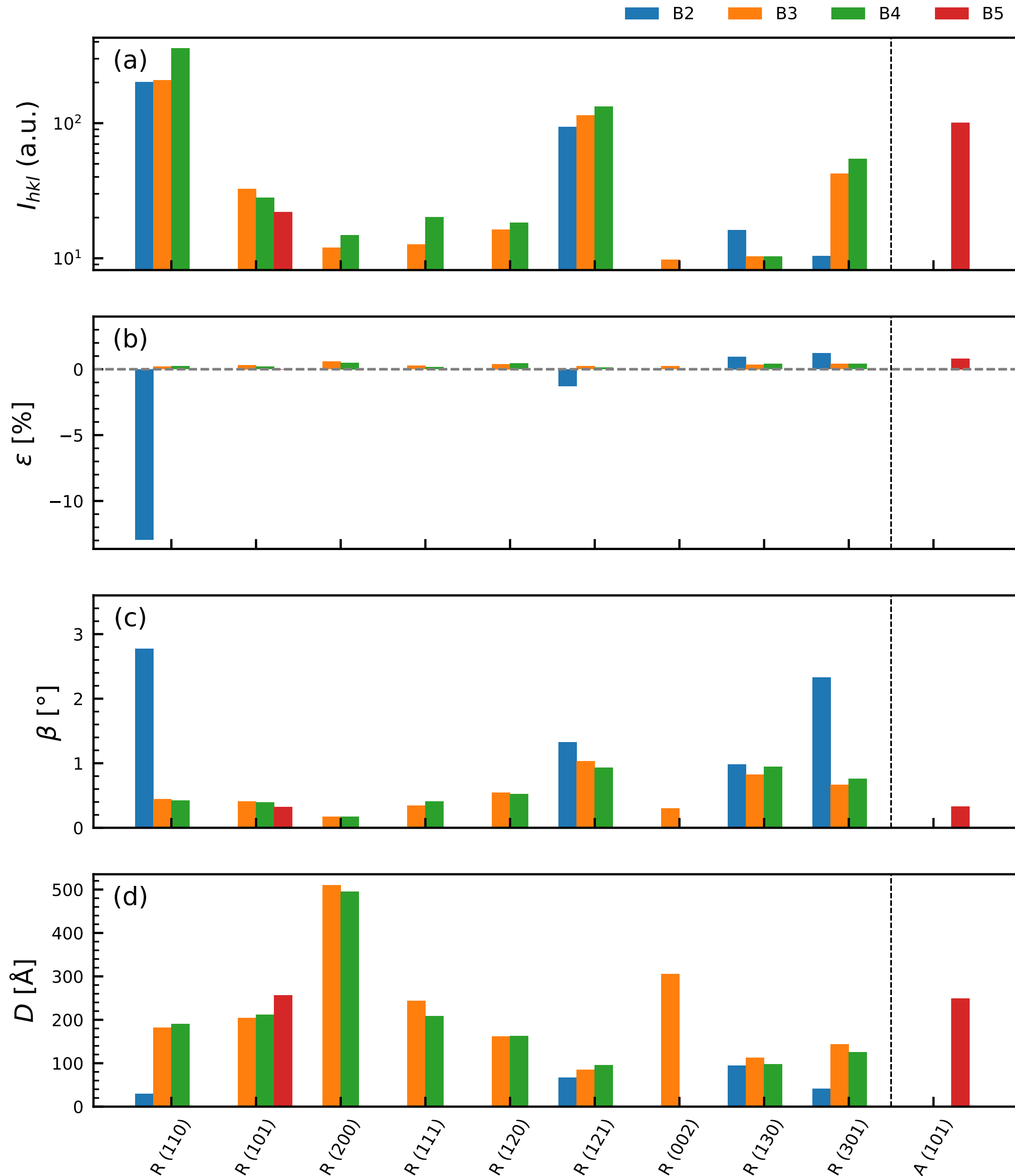

Figure 38: Quantitative GIXRD data from the curve fits on the samples on STO substrates: (a) integrated intensity I_{hkl}; (b) calculated strain ϵ, (c) full-width-half-maximum β; (d) estimated crystallite size D. The black, dashed line separates rutile and anatase planes.

As seen in Fig. 38 (b) for B2, the calculated strain for the R (110) peak is considerably large, at -12.9%. There may be several reasons for this. It could be that a different phase from rutile or anatase contributes to the diffractogram, which shifts the peak towards higher angles, which would mean that the current fit is not a good representation of the peak.

Apart from the mentioned observations, the reader should revisit Section 5.2.2 for explanations, as the results are similar to the results from the films on LAO.

5.3.3 Raman Spectroscopy

The Raman spectra acquired from B1–B5 and A2 on STO are shown in Figure 39. The data are plotted in a similar manner to the samples on Si and LAO substrates, and the following discussion will focus on differences between the STO samples and previously discussed samples.

Samples B1 on STO and B2 on STO display similar characteristics to B1 on LAO and B2 on LAO. However, in Figure 39, peaks can be seen from both samples at the $144.3\,\mathrm{cm}^{-1}$ anatase reference peak location. The same signature was not observed from B1 and B2 on LAO. This could indicate that the XRD peaks seen at $\sim 38°$ from B1 and B2 in Figure 36 indeed come from anatase (004). This would further imply that STO was able to force growth of (001)-oriented anatase, even during growth conditions which seemed highly unfavorable for the anatase phase, in agreement with ref. [47].

Samples B3 and B4 on STO are in general similar to B3 and B4 on LAO, and show peaks at the anatase reference locations. The same trend of B4 showing stronger anatase signal than B3, which was seen for the LAO samples, is also observed for the STO samples, as is evident from Figure 40. However, whereas B3 and B4 on LAO showed clear rutile traces, the only indication of rutile from the STO samples is a small difference between the substrate and film signatures in areas close to the rutile spectrum lines. This is a similar trend to what was seen in the XRD data, where the rutile peaks (particularly the R (200) peaks) where not as prominent from B3 and B4 on STO compared with B3 and B4 on LAO.

Samples B5 and A2 on STO also resemble their LAO substrate siblings (B5 and A2 on LAO). By studying the difference between the film and substrate signatures in Figure 39, the relative anatase intensity ratios for sample B5 resemble the reference spectrum of Figure 9 to a greater extent than sample A2, although the difference is not as strong as was seen from the films on LAO substrates. This supports the suggestion that the departure of the A2 spectrum from the reference anatase Raman spectrum is a consequence of higher texture, since A2 on LAO appeared more strongly textured than A2 on STO.

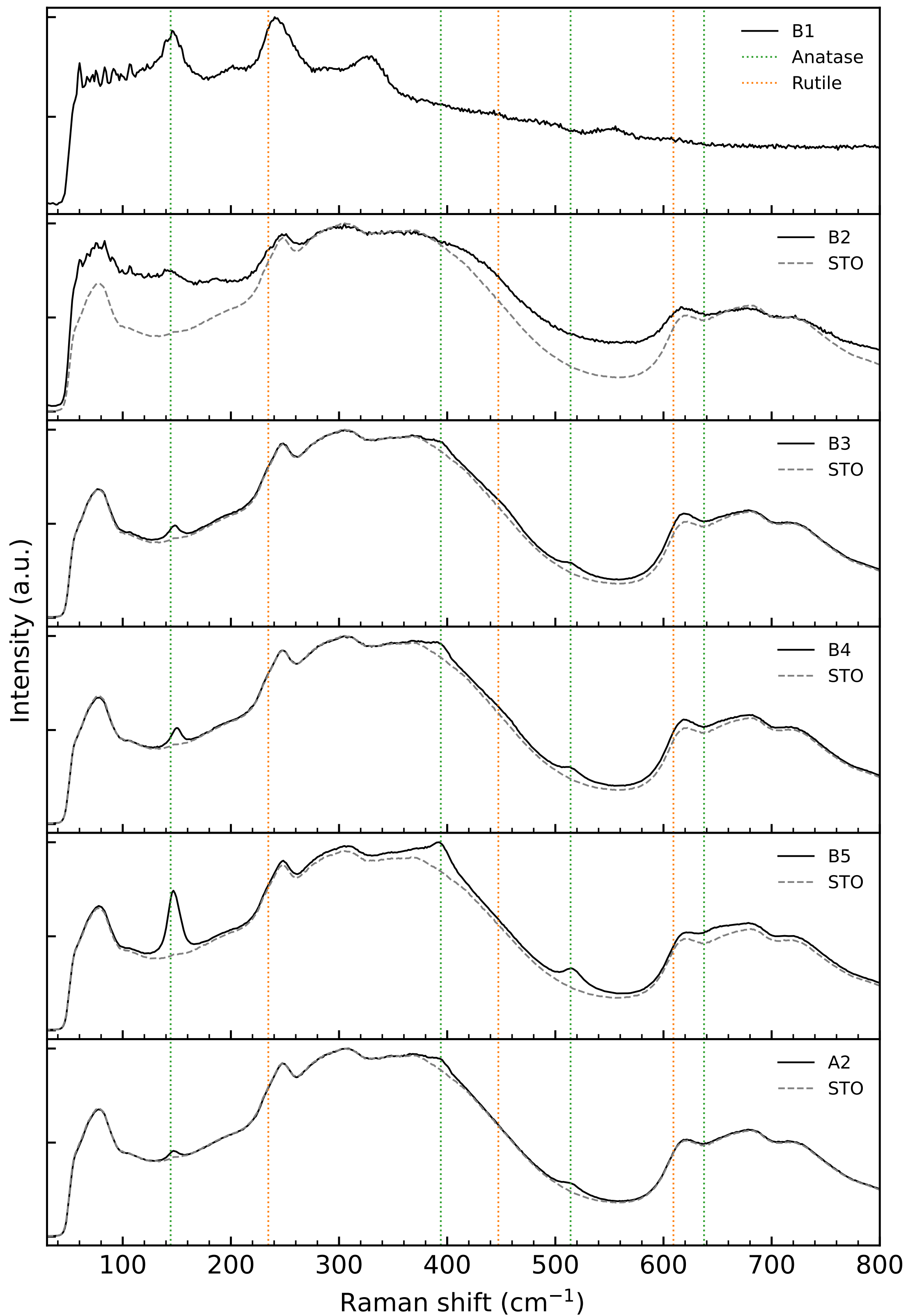

Figure 39: Raman spectra acquired for B1–B5 and A2 on STO substrates. Reference lines for the rutile (orange) and anatase (green) Raman spectra are shown. The STO substrate Raman spectrum is also included where it is appropriate.

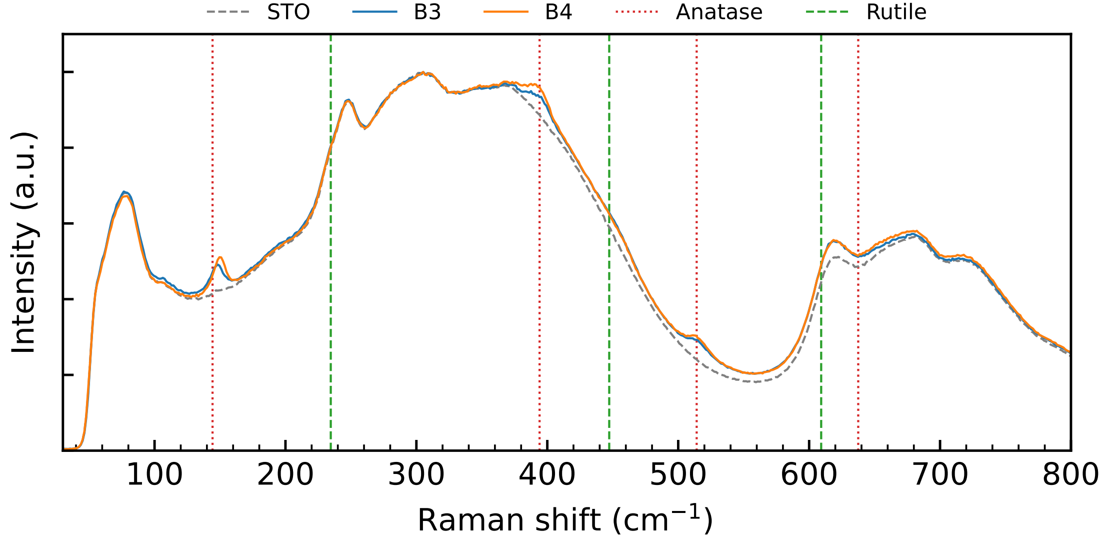

Figure 40: Compilation of the Raman spectra acquired for B3 and B4 on STO. References for the rutile and anatase spectra, as well as the STO spectrum, are included.

5.3.4 HRXRD Measurements

The high resolution X-ray diffraction results for B3–B5 and A2 on STO are shown in Figure 41. The results are plotted in a similar manner as the LAO samples, with the left subfigure showing the ω–2θ scans of the anatase (004) peaks, and the right subfigure showing the rocking curves of said peaks. The curve fits as well as reference A (004) peak locations are also displayed. The data from the curve fits are displayed in Table 10. Note that the films on STO were measured using a lower scan time per step, but this is expected to affect only the signal-to-noise ratio.

The results are similar to what was seen for the films on LAO. The B–samples show increasing strain for films deposited with increasing oxygen pressures. Furthermore, there seems to be a pattern where the most strained films are more heavily skewed towards the bulk 2θ value, suggesting strain relaxation. The peak from A2 on STO is, similar to the films on LAO, the least strained and most symmetric, as is evident from Table 10.

Notice however that there does not appear to be a big of a difference between the rocking curves, as was seen for the LAO samples. This is especially the case for A2 on STO. Recall that A2 on LAO had a significantly sharper rocking curve than the other LAO samples. Here, it seems that the crystalline quality of A2 on STO does not differ significantly from the other samples, similar to what was observed from the θ–2θ data of Section 5.3.1.

The films on STO generally display higher strain than their counterparts on LAO for the anatase (004) peaks. This agrees with the higher lattice mismatch of STO and anatase (001) compared to LAO (3.18% compared to 0.15%). However, it is difficult to confidently assign this to be the cause of the strain differences.

Table 10: Quantitative data from the curve fits on the A (004) peaks, for the films on STO substrates: peak value 2θ; calculated d-spacing d; calculated strain ϵ, FWHM β; estimated mean crystallite size D; asymmetry parameter h/l; Lorentzian fraction η.

Sample	2θ	d [Å]	ϵ [%]	β (°)	D [nm]	h/l	η
B3	37.60	2.390	0.480	0.115	69 ±2	1.636	0.08
B4	37.49	2.397	0.774	0.114	70 ±2	1.28	0.04
B5	37.33	2.407	1.195	0.151	53 ±2	1.576	0.11
A2	37.66	2.387	0.354	0.097	83 ±3	1.156	0.13

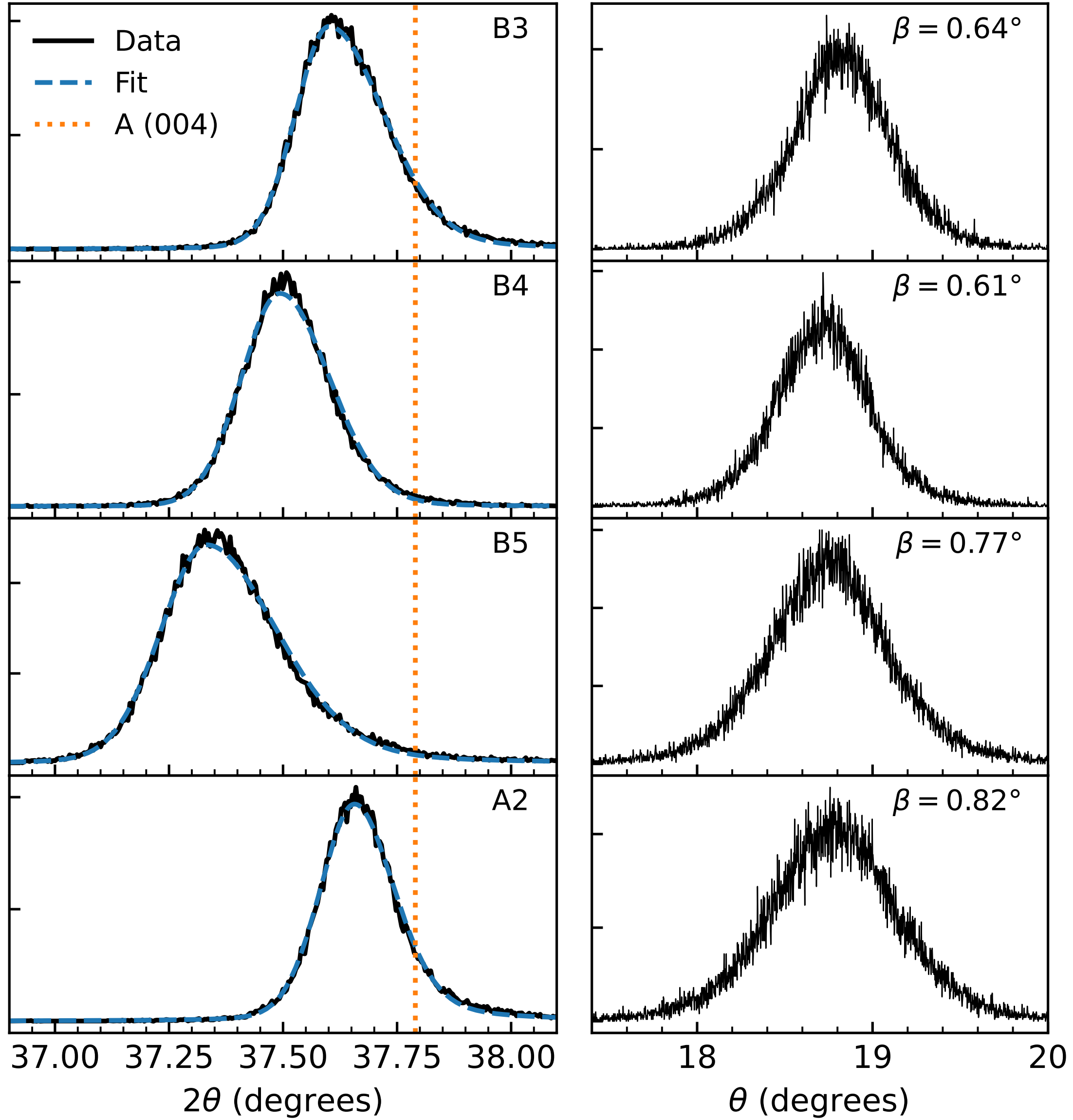

Figure 41: HRXRD diffractograms for B3–B5 and A2 on STO (001): (left) ω–2θ scans of the anatase (004) peaks, with curve fits. The bulk anatase (004) peak location is shown; (right) rocking curves of the anatase (004) peaks.

5.4 Uniform Undoped Samples on Sapphire (0001)

5.4.1 Theta–2Theta Measurements

The results of the θ–2θ scans from the films on sapphire substrates are shown in Figure 42, with a logarithmic-scale plot of the same data appearing in Figure 43. Reference lines for the rutile and anatase peak locations are included where it is appropriate.

Qualitatively, the data in Figure 42 are similar to the data from the samples on LAO and STO of figures 28 and 35. This is because they mostly display only one, sharp film peak, in addition to the substrate peak. They do not display the powder–like traits observed for the films on silicon susbstrates. It is therefore suggested that the films are in general made up of highly textured, crystalline materials. However, compared with the films on LAO and STO, the peaks appear at significantly different angles.

For B1, a pronounced peak can be seen in figure 42 around 38.8°. In sections 5.1.1 and 5.2.1, a similar peak for B1 (on LAO and Si) was also observed, and attributed to a non-TiO_2 phase. The same applies to the peak observed at $2\theta \approx 38.5°$ for B2 on sapphire in figures 42 and 43.

From Figure 42, samples B3 and B4 both show peaks at $2\theta \approx 39.5°$, close to the R (200) peak location, although the peak is somewhat shifted from B3 to B4. Note that although there appears to be two peaks for each sample, this is in fact likely to be the Kα doublet (confirmed by HRXRD, to be presented in Section 47), indicating highly crystalline materials. It is therefore suggested that the deposition parameters for B3 and B4—which in sections 5.1, 5.2 and 5.3 were found to favor (100)-oriented rutile—combined with the low lattice mismatch (3.58%) between sapphire (001) and rutile (100) surfaces, has yielded rutile of considerably high crystalline quality. The apparent strain from these peaks will be discussed in the HRXRD section below.

For samples B5 and A2, rutile (200) peaks are also suggested to appear. Recall from previous sections that the deposition parameters for these samples were suggested to favor the anatase phase. However, it seems that the sapphire substrate has been able to force rutile (100) growth, although the crystalline quality seems fairly diminished in sample B5, where the peak is broad and the Kα doublet is indistinguishable. For sample A2 the Kα doublet is clearly visible, suggesting that the rutile crystalline quality is high, although the intensity is low compared to samples B3 and B4 (likely because of a thinner film thickness).

Note from the logarithmic plot in Figure 43 that traces of polycrystalline anatase do seem to be present between 36.8° and 39° in sample B5. This is in agreement with what was expected for B5 based on the previous sections. The peaks display little shift when qualitatively compared to the anatase reference lines. Furthermore, this strengthens the notion that the prominent peak observed at $2\theta \sim 39.7°$ is indeed not from anatase, but rather from rutile (200).

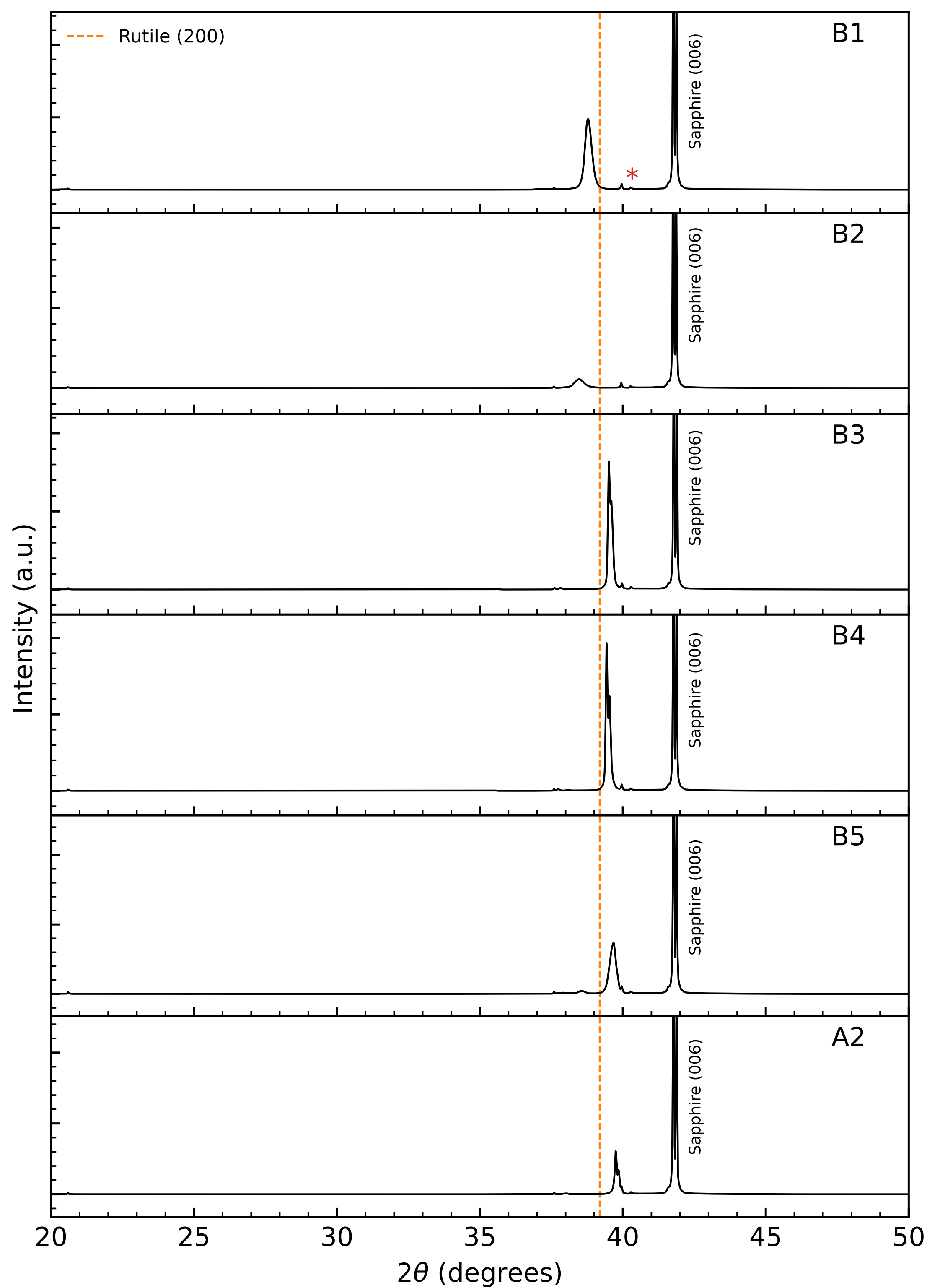

Figure 42: θ–2θ data for B1–B5 and A2 on sapphire (0001). The rutile (200) peak location is included for reference. In the topmost plot, substrate artifacts are marked by red asterisks.

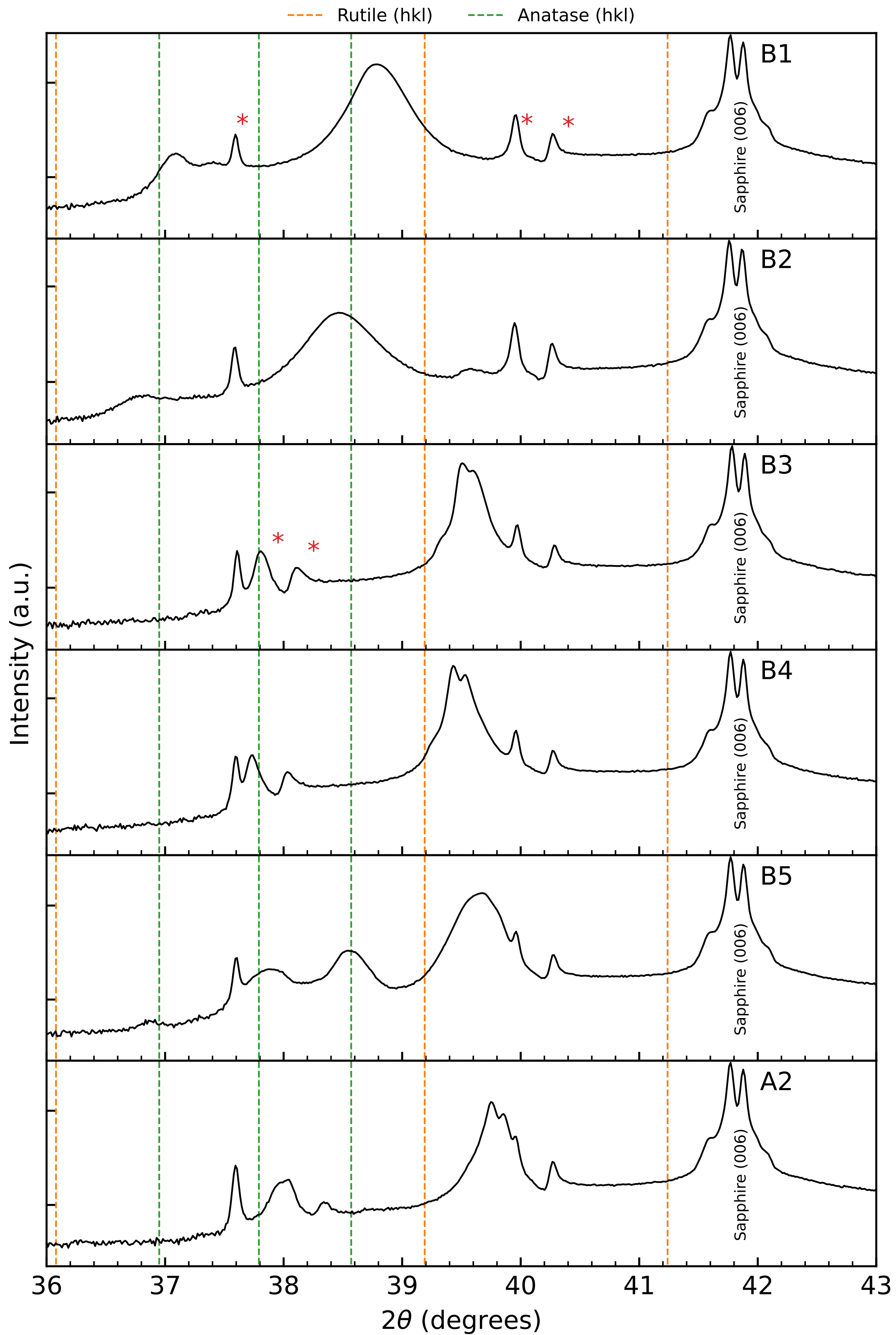

Figure 43: Logarithmic-scale plot of the θ–2θ data for B1–B5 and A2 on sapphire (0001). Substrate artifacts, as well as artifacts coming from the rutile peaks, are marked by red asterisks the first time they appear, from top to bottom.

5.4.2 GIXRD Measurements

GIXRD was performed on B2–B5 on sapphire (B1 and A2 were omitted because of time constraints). The results are shown in Figure 44. As can be seen in the figure, none of the samples gave any film signal in GIXRD. The only exception was for B5, which gave a small peak believed to be an artifact. The results confirm that the films on sapphire are highly textured, or perhaps single crystal–like. The GIXRD scan thus "misses" the reciprocal lattice points (revisit figures 3 and 4 for illustrations).

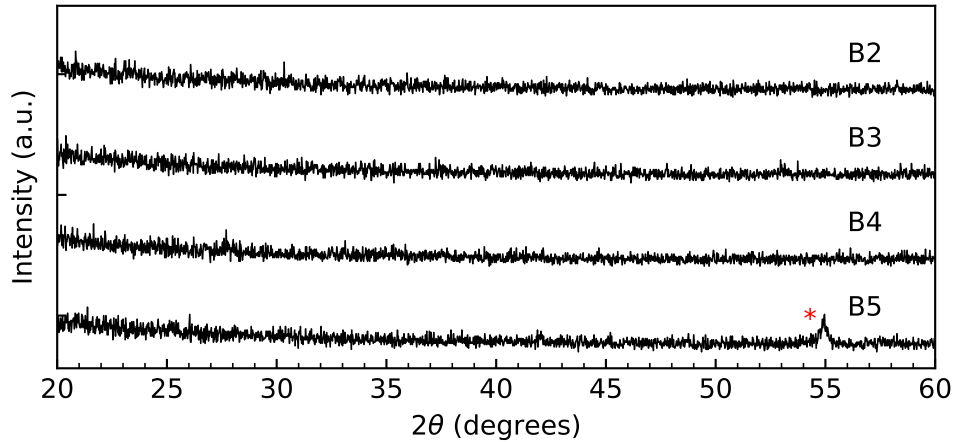

Figure 44: GIXRD data from B2–B5 on sapphire substrates. A signal from B5 believed to be an artifact of either the substrate, or a highly textured film component, is marked by a red asterisk.

5.4.3 Raman Spectroscopy

The acquired Raman spectra from the films on sapphire substrates are shown in Figure 45, and are plotted in the same manner as the previously presented Raman spectroscopy data.

The trends for the sapphire samples generally follow the same trends as the other substrate series. For instance, the rutile signal from B4 is stronger than for B3, as displayed in Figure 46. A clear difference is that the rutile signatures are significantly more pronounced than what was observed for the STO and LAO samples. This is in agreement with the XRD discussion, where the films were suggested to be comprised primarily of textured, (100)-oriented rutile.

Samples B5 and A2 on STO differ significantly from their STO, LAO and Si analogues in that pronounced peaks can be seen at the rutile reference locations. This is apparent when comparing the film and substrate signals in Figure 45. This further underlines the θ–2θ discussion from section 5.4, where there two samples were suggested to be mainly comprised of highly textured, (100)-oriented rutile.

A surprising result from the Raman acquisition of B5 is the pronounced anatase signature, noted by comparison with the anatase reference lines in Figure 45. This indicates that the anatase-like XRD signal observed in Figure 43 indeed stems from the anatase phase. However, it is surprising that the peaks should be so dominant in the Raman acquisition, even surpassing the rutile intensities, especially when the GIXRD did not show any traces of anatase.

Several, unidentified peaks (those which neither agree with TiO_2 nor with the sapphire signature) can be seen for all samples. Identification of these is beyond the scope of this thesis, but it could be suggested that non-TiO_2 phases exist in the films.

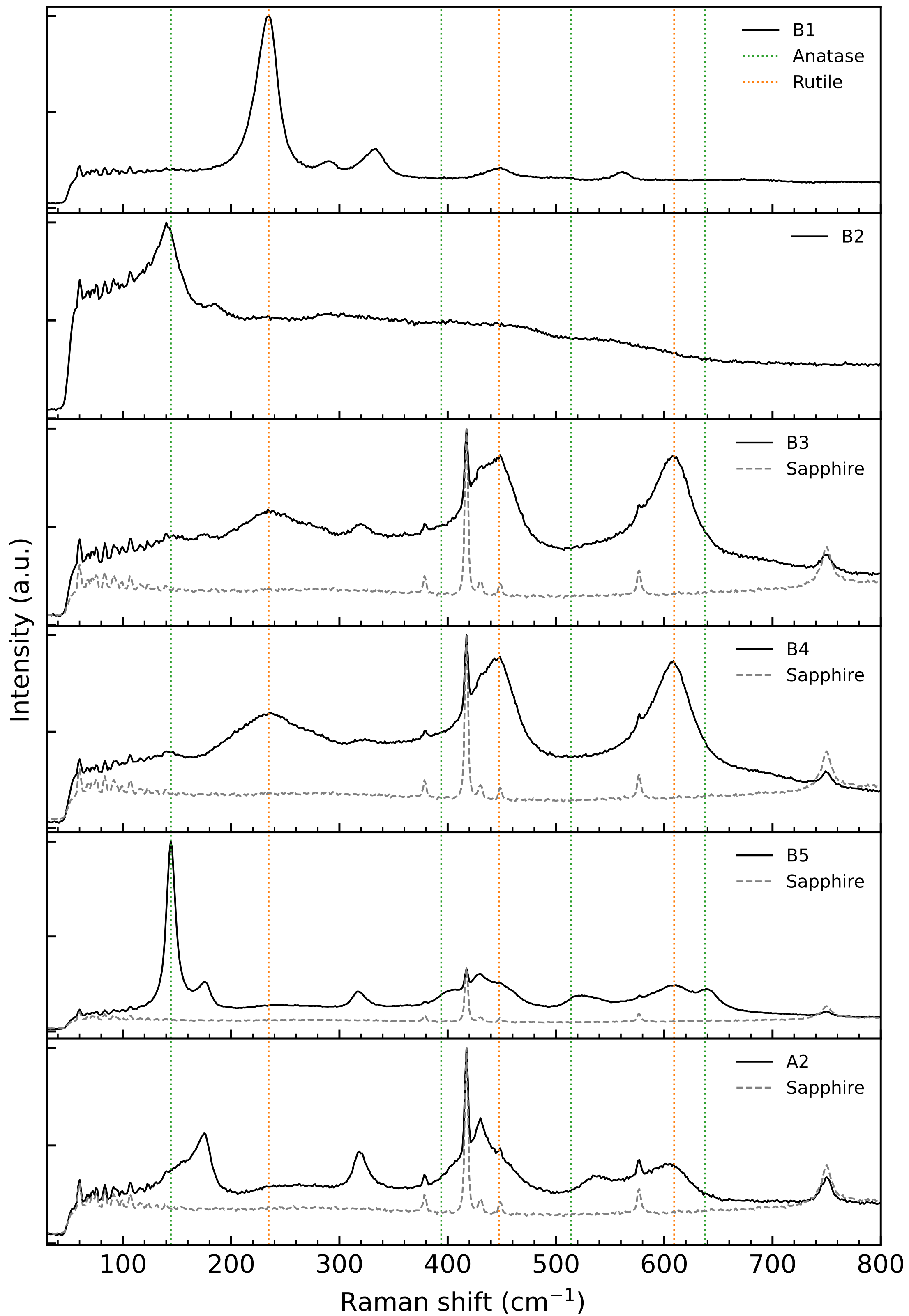

Figure 45: Raman spectra acquired for B1–B5 and A2 on sapphire substrates. Reference lines for the rutile (orange) and anatase (green) Raman spectra are shown. The substrate Raman spectrum is also included where it is appropriate.

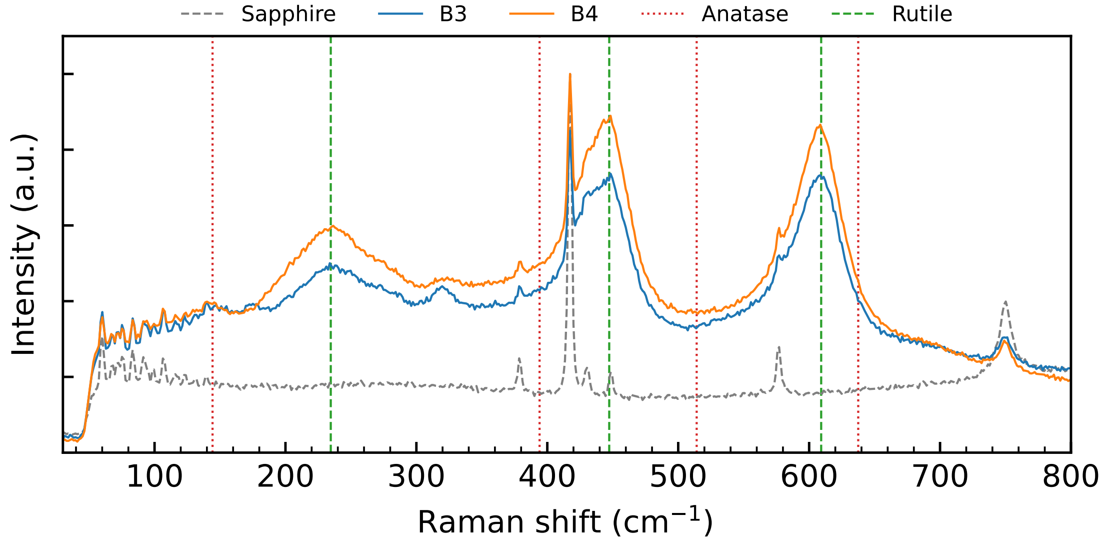

Figure 46: Compilation of the Raman spectra acquired for B3 and B4 on sapphire. References for the rutile and anatase spectra, as well as the sapphire spectrum, are included.

5.4.4 HRXRD Measurements

The high resolution X-ray diffraction results for the films on sapphire substrates are shown in Figure 47. The results are plotted in the same manner as the films on LAO and STO in sections 5.2.4 and 5.3.4. The only difference is the ω–2θ range, being focused on the rutile (200) peak location. Hence, the rutile (200) bulk 2θ value is shown. The parameters extracted from the curve fits are shown in Table 11. Note the poor fit for A2; this is, however, not expected to alter the 2θ and β values, and is thus ignored.

The trends seen in Figure 47 are quite different from those observed in figures 34 and 41 for films on LAO and STO (which were similar to each other). However, it is important to note that the θ–2θ and Raman results were sufficiently indicative of textured, (100)-oriented rutile existing in the samples, in contrast to the films on LAO and STO, which showed (001)-oriented anatase. The difference in trends are therefore not surprising.

As seen in Figure 47, the R (200) peaks are all shifted towards *higher* 2θ values, compared with the bulk value. This results in negative ϵ values (compressive strain) in Table 11. Furthermore, the measurements do not show strictly increasing (in terms of magnitude) strain for samples deposited with strictly increasing oxygen pressures. This contrasts to what was reported in sections 5.2.4 and 5.3.4. A specific contrast is that B3 on sapphire displays more shift than B4. It could be that B3 and B4 on sapphire were mistakenly interchanged, which would explain the difference in trends compared with the films on LAO and STO. However, the peak from A2 on sapphire is even more shifted from the bulk value than the other samples, which is also a change in trends from the LAO and STO analogues.

Table 11: Quantitative data from the curve fits on the ω–2θ scans of the R (200) peaks, for the films on sapphire substrates: peak value 2θ; calculated d-spacing d; calculated strain ϵ, FWHM β; estimated mean crystallite size D; asymmetry parameter h/l; Lorentzian fraction η.

Sample	2θ	d [Å]	ϵ [%]	β (°)	D [nm]	h/l	η
B3	39.42	2.284	-0.559	0.059	136±9	1.458	0.0
B4	39.35	2.288	-0.385	0.063	128±8	1.423	0.1
B5	39.54	2.277	-0.864	0.125	64±2	0.736	0.09
A2	39.67	2.270	-1.169	0.043	192±16	0.792	0.31

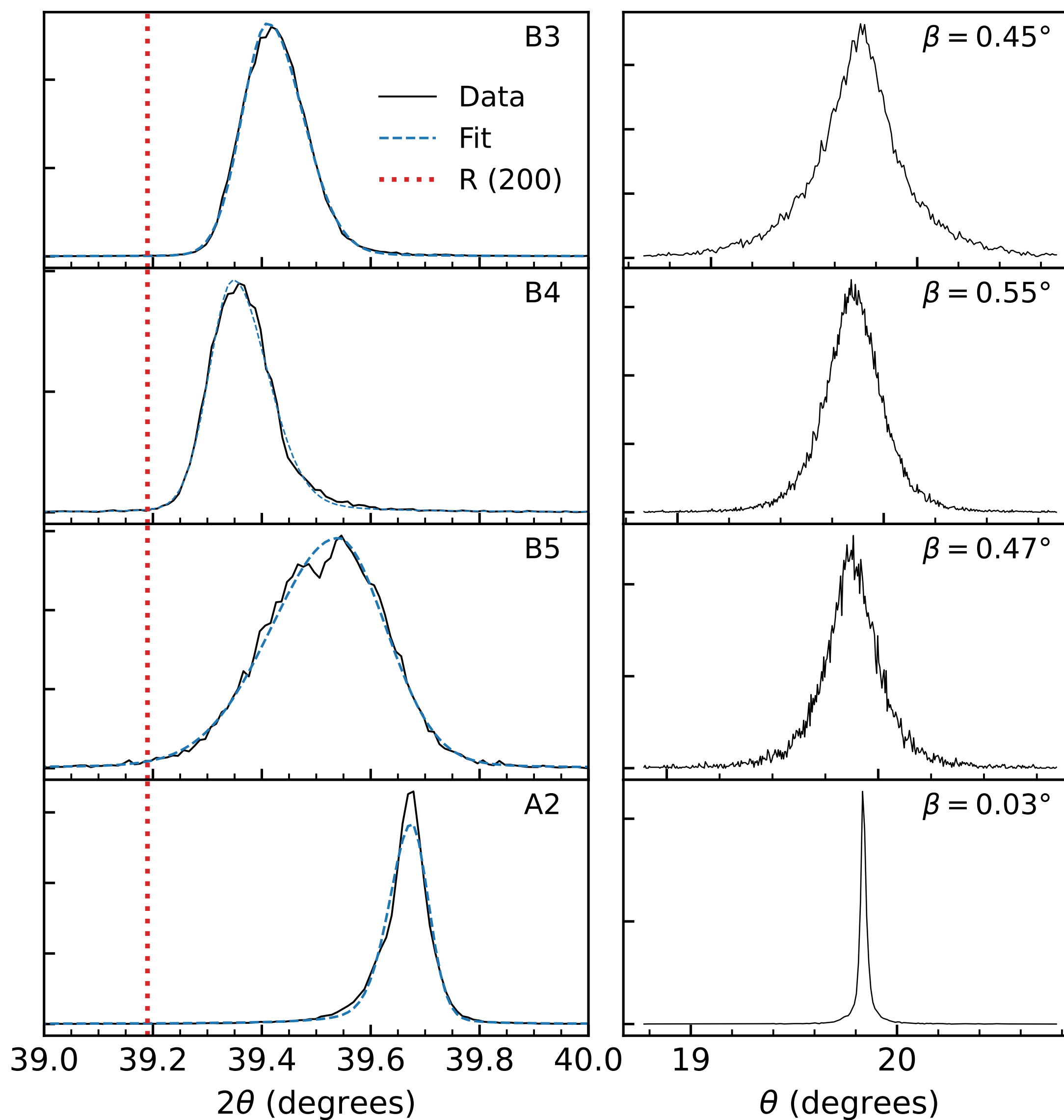

Figure 47: HRXRD diffractograms for B3–B5 and A2 on sapphire: (left) ω–2θ scans of the rutile (200) peaks, with curve fits. The bulk rutile (200) peak location is shown; (right) rocking curves of the rutile (200) peaks.

From Figure 47, there appears to be some strain relaxation in all the samples, but the nature of this differs from the LAO and STO samples. Recall that in sections 5.2.4 and 5.3.4, the peaks were all skewed *towards* the bulk 2θ value. In figure 47, B5 and A2 mirror this behavior, but B3 and B4 are in fact skewed away from the bulk value. However, this need not be surprising, as the deposition parameters for B3 and B4 were, in Section 5.1, found to favor growth of the crystalline phase, during deposition on an amorphous SiO_2 surface. Samples B5 and A2, however, were suggested to favor the anatase phase.

It could therefore be that differences in growth defects cause the differences in strain relaxation behaviour between samples B3/B4, and B5/A2. The fact that the prominent rutile (200) peak only appears on the sapphire substrates for the B5 and A2 samples strongly indicates that this is caused by the substrate “forcing” rutile (100) growth (i.e., leading to rutile growth in unfavorable conditions).

Since the B5 and A2 parameters where suggested to naturally favor the anatase phase, it could be that completely different defects are present for the rutile phase in these films, compared with samples B3 and B4 which seemed to favor rutile with a preference for exactly the observed (100) orientation.

A noteworthy observation from Figure 47 is that the quality of the rutile peak from A2 is significantly higher than the other samples. This is evident from D in Table 11, as well as the rocking curve FWHM of A2, which is an entire order of magnitude narrower than for the other samples, suggesting a much lower mosaic spread of the crystal grains. A more noteworthy observation still is that the crystallite size estimate for A2 on Sapphire is higher than for both A2 on LAO and A2 on STO (149 ± 10 and 83 ± 3 nm, respectively).

5.5 Summary of Discussion from Characterization of Uniform Undoped Samples

5.5.1 Discussion of Deposition Parameters

Having characterized the undoped uniform samples with several XRD techniques, as well as Raman spectroscopy, a discussion is in order for the overall interpretation of the results.

From Section 5.1, it was seen that the various deposition parameters favored growth of different TiO_2 phases, when deposited on an amorphous (SiO_2) surface. B1 on Si was characterized as consisting of substoichiometric TiO_2, whereas B2 on Si was characterized as consisting of both substoichiometric TiO_2, in addition to low quality, polycrystalline rutile. It would seem that these characteristics arose from lack of O_2 flow (0 sccm and 1 sccm for B1 and B2, respectively), as this is all that separates B1–B2 from B3–B5. This trend continued for B1–2 on LAO, STO and sapphire. This could mean that stoichiometric transfer of TiO_2 is significantly limited for deposition with low O_2 flow and total pressure.

B3–B4 on Si were in Section 5.1 characterized as powder–like rutile with (100)

preferred orientation (indicated by the θ–2θ data). It is therefore suggested that the growth parameters of B3 and B4 favor (100) oriented rutile.

However, it was seen that the XRD and Raman characteristics for films deposited with B3 and B4 parameters were significantly influenced by their respective substrates. On LAO and STO substrates, the films were characterized as highly textured, (001)-oriented anatase. This was attributed to the low lattice mismatch between the substrates and anatase (001), 0.15% and 3.18% for LAO and STO, respectively. In agreement with literature [47][48][50][49], this indicates that the substrates are indeed able to procure textured anatase growth. In this work, this is seen to occur even for deposition parameters which seem to favor rutile. Based on the asymmetry of the A (004) peaks in HRXRD (see tables 9 and 10), it is suggested that some strain relaxation occurs for the films on LAO and STO, but the nature of this strain is not known.

In GIXRD, the characteristics of B3–4 on LAO and STO were significantly different from θ–2θ. In the GI configuration, both samples showed polycrystalline rutile, resembling the GI results for B3–4 on Si. Note that this does not contradict the appearance of anatase in θ–2θ, as GIXRD is prone to "missing" diffraction spots coming from textured materials (see Fig. 4).

A possible explanation for the characteristics of B3–4 on LAO and STO could be that initially, as a cause of low lattice mismatch, textured anatase grows. After growing to a certain film thickness, rutile grains start forming, which then start to dominate owing to the rutile–favorable growth conditions.

It should also be noted that the samples were all deposited with a nominal substrate temperature $T_s = 700\,^{\circ}\mathrm{C}$. This temperature is above the temperature for an anatase-to-rutile transformation [22]. It is also experimentally reported that TiO_2 nanoparticles "prefer" the anatase structure for diameters up to about 10 nm owing to lower surface energies [29]. It could therefore be that, initially, primarily anatase grains grew even for B3 and B4 on Si, but that the an anatase–rutile transformation occured owing to the high substrate temperature.

If this is the case, then the LAO and STO substrates would have "maintained" anatase rather than "forced" it. In other words, it could be that the LAO and STO susbtrates were able to *stop* the anatase-rutile transformation from occurring. If, on the other hand, the first nucleations on B3 and B4 on Si consisted of primarily *rutile* grains, then LAO and STO would have "forced" anatase growth.

However, although high substrate temeratures were speculated to favor growth of rutile, it should be stated that higher substrate temperatures have been seen to favor anatase (001) growth when depositing on Si (100) for sufficiently high pressures (5×10^{-2} mbar) [43].

No correlation could be found for co-existence of rutile (100) and anatase (112) planes. The *opposite* was in fact observed for the films on LAO. Therefore, it is suggested that an anatase–to–rutile transformation by nucleation of rutile (100) planes at anatase (112) twin boundaries [22] have *not* occurred, and that there is some other growth mechanism that leads to strong growth of rutile (100) planes.

As for B3–B4 on sapphire, high quality (100)-oriented rutile was observed. This was of course in stark contrast to the films on LAO and STO, and also in *some* contrast with B3–B4 on Si, because the latter films were substantially less textured. The growth of high quality (100)-oriented rutile was attributed to low lattice mismatch (3.58%). This further confirms that the choice of substrate can significantly alter film composition, in agreement with literature.

B5 on Si was, in Section 5.1, characterized as a mixture of polycrystalline rutile with minor (100) preferred orientation, and polycrystalline anatase with prominent (001) and (112) preferred orientations. It was also stated that the anatase phase seemed to dominate. Based on this, it would seem that the B5 growth parameters favor the anatase phase. This translated into the LAO and STO samples, which were characterized as mostly textured, (001)-oriented anatase, although some rutile was observed in GIXRD.

B5 on sapphire was characterized as textured, (100)-oriented rutile. This was attributed to substrate influence, similar to B3–B4 on LAO and STO. Furthermore, the crystalline quality determined through HRXRD for B5 on sapphire was not as good as B3–4 on sapphire. This further confirms that lower oxygen pressures (and thus, higher kinetic energies) were "rutile-favorable".

For the B–series, it does seem that higher oxygen pressures favor the anatase phase. This is in agreement with ref. [45], where higher oxygen pressures were associated with a decrease in the kinetic energy energy of ablated species—thus, with anatase being more stable at lower temperatures, favoring anatase growth.

The A2 films were noticeably different from the B–series on all substrates. A2 on Si was characterized as consisting primarily of (001)-oriented, polycrystalline anatase, in addition to some polycrystalline rutile. This suggests that the A2 deposition parameters were the most anatase-favoring of the A and B–series. Although the oxygen pressure was lower than for the B–series, the lower laser fluence of A2 ($0.8\,\mathrm{J/cm^2}$ compared to $2.0\,\mathrm{J/cm^2}$ for B–series) could have caused a lower kinetic energy in ablated species, which according to ref. [45] would be associated with anatase growth.

On the other substrates, the XRD characteristics of A2 were similar to B3–B4, but with substantially improved crystalline quality (as indicated by mean crystallite size estimates and less strain from HRXRD), with the exception of A2 on STO which was not so different from B3–B5. A2 therefore seemed to generally give better film crystalline quality. The A2 parameters differed from the B–series in oxygen pressure, laser fluence and film thickness. It is therefore difficult to single out which parameters caused the overall better quality.

5.5.2 Evaluation of Characterization Methods

It should be emphasized that the conclusions drawn for *the same* samples were often different based on the different characterization methods. The difference was largest for the θ–2θ and GIXRD methods. The θ–2θ results for B3–B4 on LAO and STO all indicated textured, (001)-oriented anatase, whereas the GIXRD data indicated only polycrystalline rutile. This was explained by the **k**-space trajectory of the GIXRD

configuration. As in Fig. 4 (a), the GIXRD measurement traces out a curve in reciprocal space, which may entirely miss the diffraction peaks from highly textured materials. Many of the more textured samples (like A2 on STO and the films on sapphire) did not show any signal apart from substrate artifacts in GIXRD, for the same reason.

While B3–B4 on silicon were characterized as rutile in both θ–2θ and GIXRD, the (100) preferred orientation for rutile was not registered in GIXRD. The reason for this is that GIXRD does not detect planes oriented parallel to the sample surface.

Owing to the textured nature of the samples, rutile–anatase phase quantifications such as by using the Spurr equation (Eq. (14)) would give highly erroneous results.

For characterization of pulsed laser deposited thin films by GIXRD, it is suggested that one should always do θ–2θ in addition to the GI measurements. While GIXRD has its advantages [19], this precaution will help to prevent loss of crucial characterization information when samples are textured.

Another difference in sample characteristics between techniques was that of the XRD methods and Raman spectroscopy. It was seen for several samples on several substrates that Raman spectroscopy sometimes detected TiO_2 phases which were not confidently detected in XRD. This was the case for the anatase phase in the films on sapphire. It would therefore seem that Raman spectroscopy was more sensitive with regards to phase identification, for the samples described in this work.

In general, the Raman spectroscopy complemented the XRD characterization. The Raman spectroscopy was also useful in cases where it was difficult to do phase identification by XRD alone. The conclusion is that Raman spectroscopy has functioned well as a complementary method to XRD in the present work. However, only quantitative analysis was performed, and the way quantitative Raman characterization would complement the XRD data has not been investigated.

5.6 Continuous Compositional Spread (CCS) Samples

The results and discussion for the CCS samples will be presented in this section.

The results for the *uncapped* samples will be presented first. This includes CCS-Si-NoCap, and its undoped reference sample CCS-Si-NoCap-Ref, which were both deposited using only O_2 gas. Next, the results of the *capped* samples will be presented. This is indcludes CCS-Si-Cap and its undoped reference sample CCS-Si-Cap-Ref. After this, the results of CCS-LAO-Cap will be presented.

The undoped references samples will always be presented first.

5.6.1 CCS-Si-NoCap-Ref

XRD Results and discussion

The θ–2θ scan of CCS-Si-NoCap-Ref, along with a thickness map of the sample, are shown in Figure 48 (b) and (a), respectively. The dashed boxes indicate the areas measured: Area 1 (blue box, close to the first plume center), Area 2 (orange box, close to the wafer center), and Area 3 (red box, close to the second plume center).

CCS-Si-Cap-Ref was deposited with the same deposition parameters as B5 on silicon in Section 5.1, but with two plume centers. As the XRD data in Fig. 48 (b) show, the film is similar to B5 on Si in all measured areas, which was expected. CCS-Si-Cap-Ref is therefore characterized as mainly polycrystalline anatase with (001) and (112) preferred orientations, along with some polycrystalline rutile (refer to Sec. 5.1.1 for details). No further discussion will be made for CCS-Si-NoCap-Ref, as it is only a reference sample for CCS-Si-NoCap, which will be presented next.

5.6.2 CCS-Si-NoCap

XRD Results and discussion

The θ–2θ data from sample CCS-Si-NoCap are shown in Figure 49, along with a thickness map of the sample, indicating the measured areas similar to in Fig. 48. The colored circles indicate the approximate positions where Raman spectroscopy measurements were made. Approximate dopant concentrations (for Cr) are also denoted. The data from the four areas are displayed together with the calculated rutile powder XRD pattern, in addition to the A (110) and A (004) peak positions for the anatase phase.

Several broad peaks can be seen for all areas in Figure 49, indicating existence of crystalline materials in the all areas of the film. The peak positions, intensities and widths can be seen to vary between positions, indicating a change in structural composition across the sample.

In Area 2 (blue curve in Fig. 49, 3 at% Cr), a prominent peak at the anatase (004)

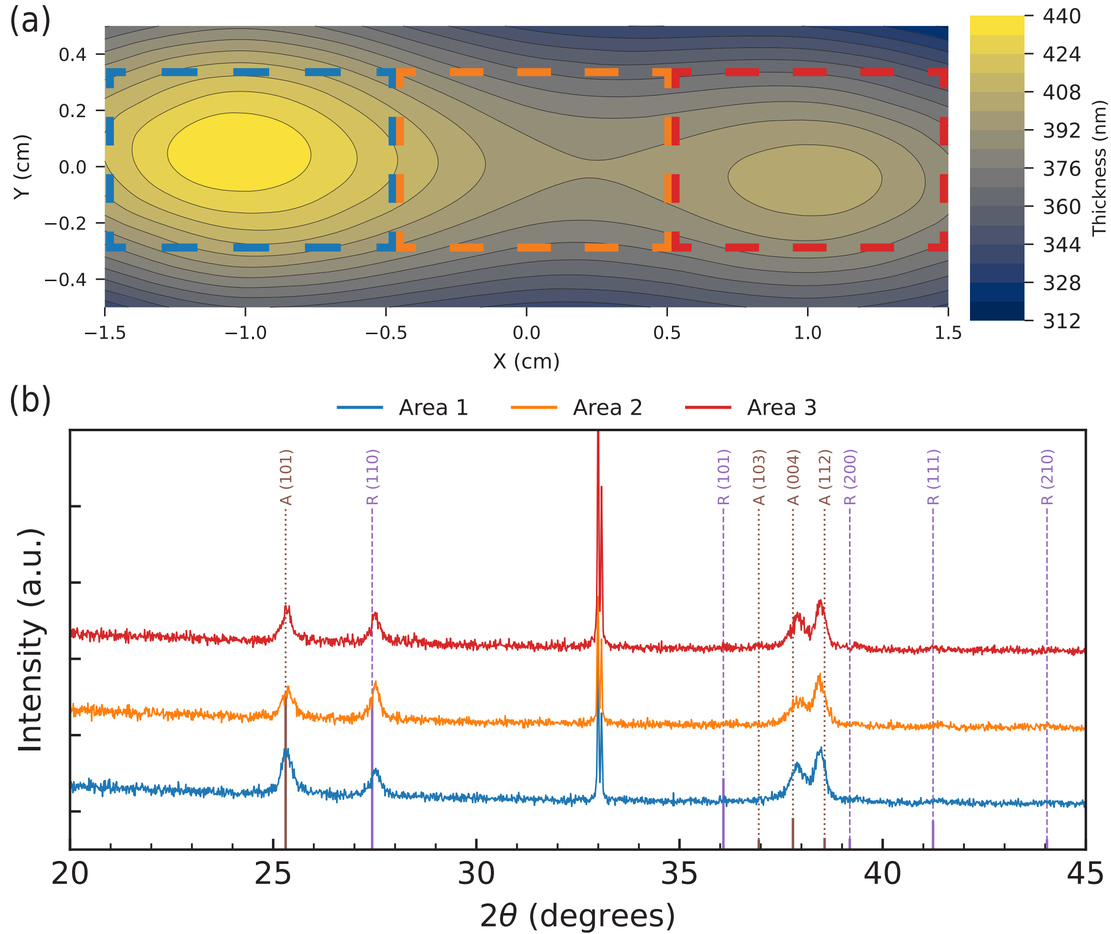

Figure 48: (a) Thickness map of sample CCS-Si-NoCap-Ref, with the areas measured by XRD indicated: (blue) Area 2, (orange) Area 2 and (red). (b) The θ–2θ diffractogram from the measured areas of CCS-Si-NoCap-Ref. The substrate peak from Si(200) is seen at 32.98°. The rutile and anatase powder patterns are also shown for reference, with solid lines indicating relative powder XRD intensities, and dashed lines to guide the eyes.

location can be seen. This peak appears to be the only clearly distinguishable peak from the anatase phase in Area 2. In Area 3 (orange curve, 5 at% Cr), the peak at the same 2θ angle has severely diminished compared with position 2. Based on these findings, it is suggested that Areas 2 and 3 contain textured, (001)-oriented anatase. By comparison with the reference sample data in Fig. 48 (b), it seems that the introduction of (Cr,N) doping has affected the anatase growth.

In Area 4, a peak is introduced at $2\theta \approx 25.3°$, the A (101) peak location. This peak can be seen in Fig. 49 (b) to become more prominent in Area 5. It is suggested that the anatase components in Areas 4 and 5 are *less* textured (as they only show the "characteristic" peak) compared with Areas 2 and 3. After comparison with the reference data in Fig. 48 (b), this development is attributed to the introduction of (Cr,N)-doping.

Some trends can also be seen across the sample with respect to the rutile phase. As seen from Figure 49, the rutile (200) peaks grow stronger and sharper from Area 2

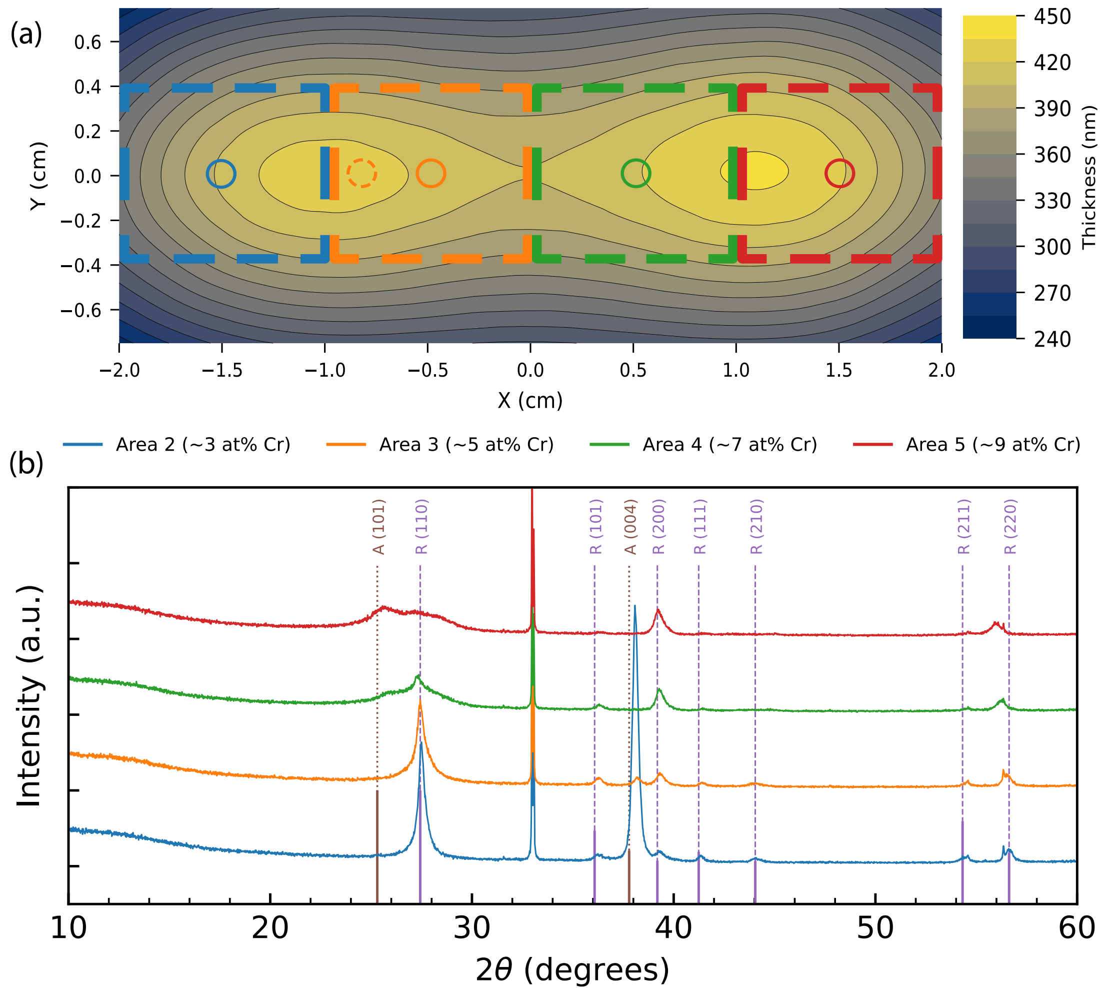

Figure 49: (a) Thickness map of sample CCS-Si-NoCap, with the areas measured by XRD indicated: (blue) Area 2, (orange) Area 3, (green) Area 4 and (red) Area 5. Circles indicate the approximate locations where Raman measurements were made. (b) The θ–2θ diffractogram from the measured areas of CCS-Si-NoCap. The substrate peak from Si(200) is seen at 32.98°. The rutile and anatase powder patterns are also shown for reference, with solid lines indicating relative powder XRD intensities, and dashed lines to guide the eyes.

towards Area 5, while other rutile peaks diminish in intensity. This indicates that the degree of preferred orientation increases, with respect to the (100)-orientation. It is therefore suggested that the (Cr,N)-doping favors the (100)-orientation of rutile.

Another trend observed for the rutile peaks in Figure 49 is a broadening of the R (110) peak. The broadening is prominent in Area 4 (green curve) and even more so in Area 5. This could indicate a decrease in the mean crystallite sizes of the rutile phase. The broadening could also come from a CrO_2 peak at $2\theta \approx 27.5°$ (see Fig. B.1 in Appendix B).

Quantitative data analysis

Curve fits were performed on all θ–2θ data of sample CCS-Si-NoCap, and the results are shown in Figure 50. The figure shows the total curve fits along with the raw data.

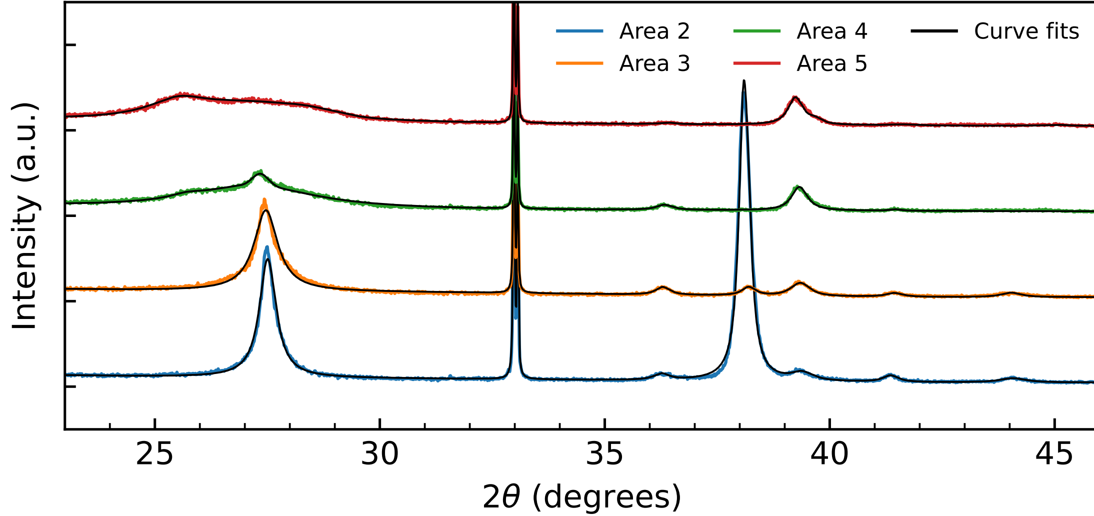

Figure 50: Plot of the curve fits performed on XRD data from CCS-Si-NoCap.

The quantitative data as extracted from the curve fits are displayed in Figure 51. The presentation and parameters are the same as what was presented in Section 5.1.1.

The data shown in Figure 51 generally confirm the visual analysis of the XRD data. As seen in Fig. 51 (a), the rutile peak intensities all diminish from Area 2 to 5, except for the rutile (200) peak, which increases. The same trend is also observed with regards to strain, where the rutile (200) peaks are calculated to show decreasing strain from Area 2 to 5, opposite of what the other rutile peaks indicate.

When studying figures 51 (d) and (e), a clear trend is seen for the increase in estimated mean crystallite size and texture coefficient for the R (200) peak.

A discussion seems appropriate with respect to the peak broadening of the R (110) peak, which could be seen for areas 4 and 5 in Figure 49. Figure 52 shows the curve fit together with the data in this region. The individual functions for the film peaks as well as the background are also plotted. The peak centered around the R (110) location was fitted using two peaks: one Lorentzian and one Gaussian. The estimated mean crystallite size for the latter function was 200 Å, whereas for the Lorentzian the estimate was 24 Å, smaller than the lattice constants of rutile. The two estimates therefore indicate the existence of both crystalline and amorphous–like rutile in Area 4.

Figure 52 also shows good agreement when fitting a peak close to the anatase (101) peak location in the data from Area 4. However, as seen in Fig. 51 (b), the calculated strain was approximately -1%.

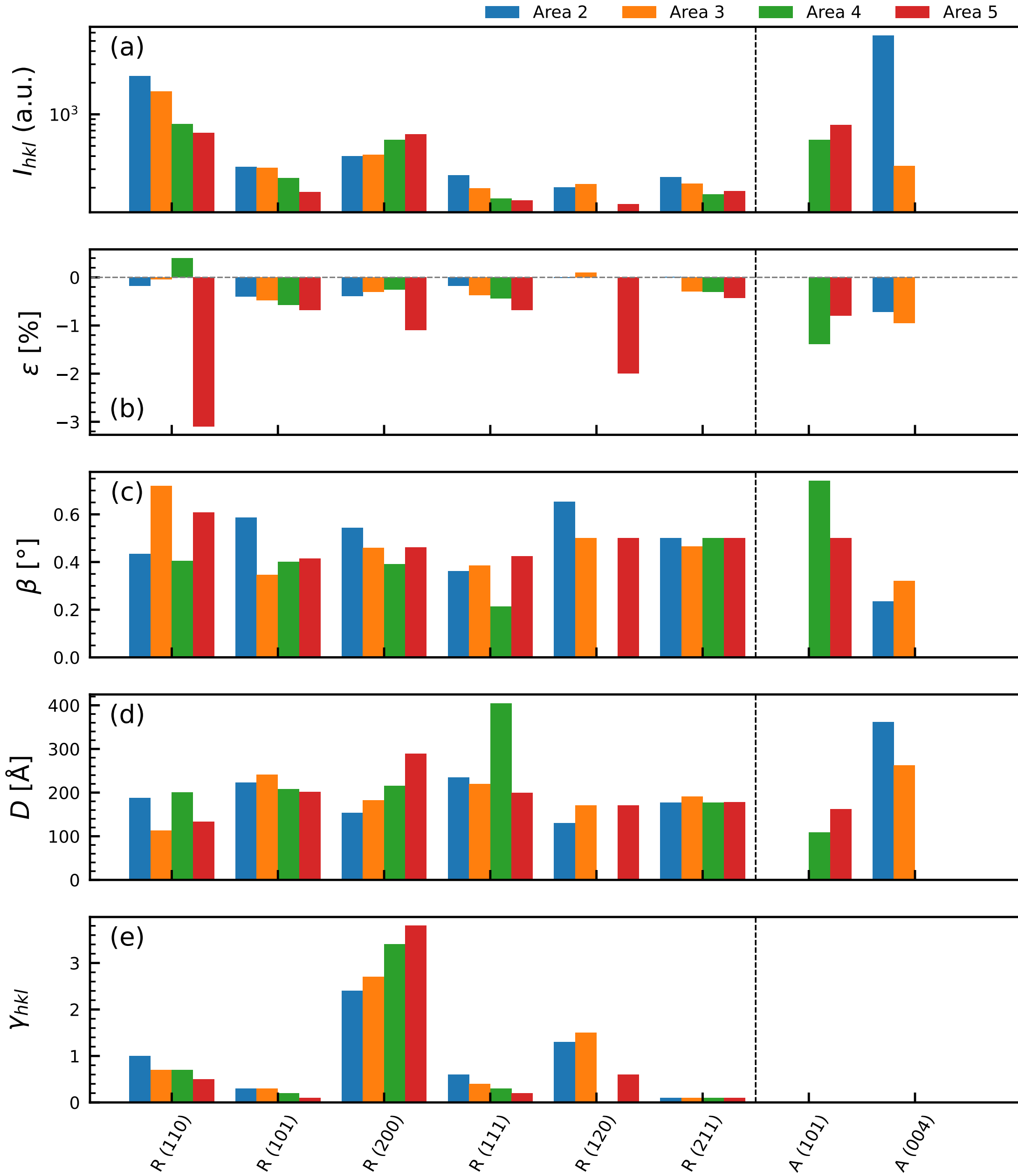

Figure 51: Quantitative data from the curve fits of CCS-Si-NoCap: (a) integrated intensity I_{hkl}; (b) measured strain ϵ; (c) full-width-half-maximum β; (d) estimated mean crystallite size D; (e) texture coefficient γ_{hkl}. Black, dashed line separates rutile and anatase planes.

A detailed plot of the curve fit for Area 5 is shown in Figure 53. The fit is generally worse than for Area 4 because the broad peak was significantly incompatible with either a Lorentzian or Gaussian function. A better fit may always be achieved by using more peak profiles, but the amount of profiles used was kept low in order to not obscure the discussion, as it might have been difficult to interpret a fit based on i.e. five different Lorentzians. Nonetheless, the curve fit suggests that the crystalline quality of the R (101) has deteriorated further when compared with Area 4, as there is a Gaussian profile with $D = 20\,\text{Å}$ at the R (101) location.

Notice also the peak ($D = 48$ Å) at $2\theta \approx 28.2°$, which is attributed to CrO_2 (see Fig. B.1 in Appendix B).

In agreement with the previous discussion, the Lorentzian fitted on the A (101) peak location is more intense and suggests less strain in Area 5 compared to Area 4. However, the estimated crystallite size is not significantly altered. It therefore seems that there is a difference in the behaviour of the anatase and rutile phase when dopant levels increase, as the A (101) peak is not compromised in the same manner as the R (110) peak.

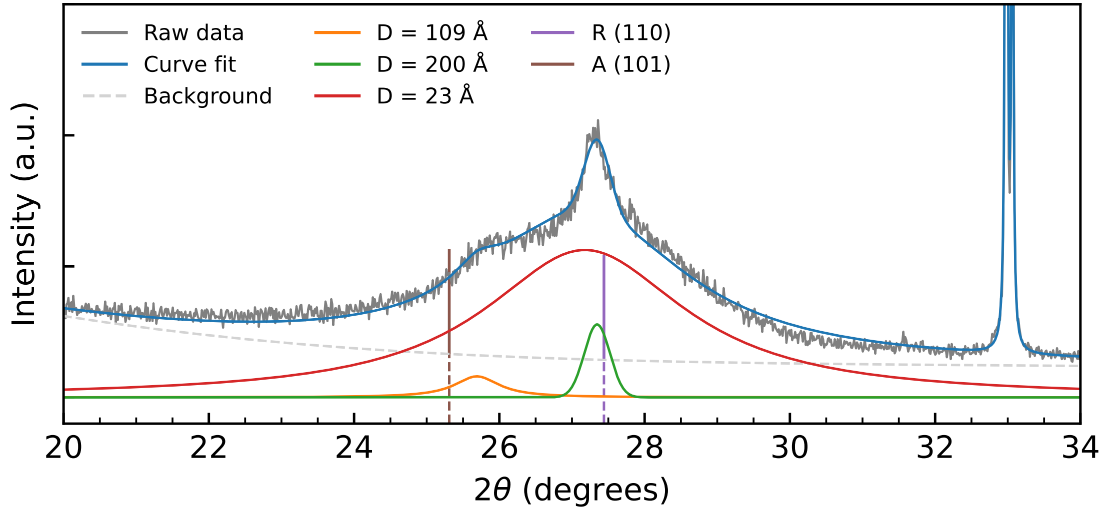

Figure 52: Details of the curve fit performed on XRD data from Area 4 of CCS-Si-NoCap. The total fit is plotted along with the fitted background and individual functions. Rutile and anatase peak locations are also shown.

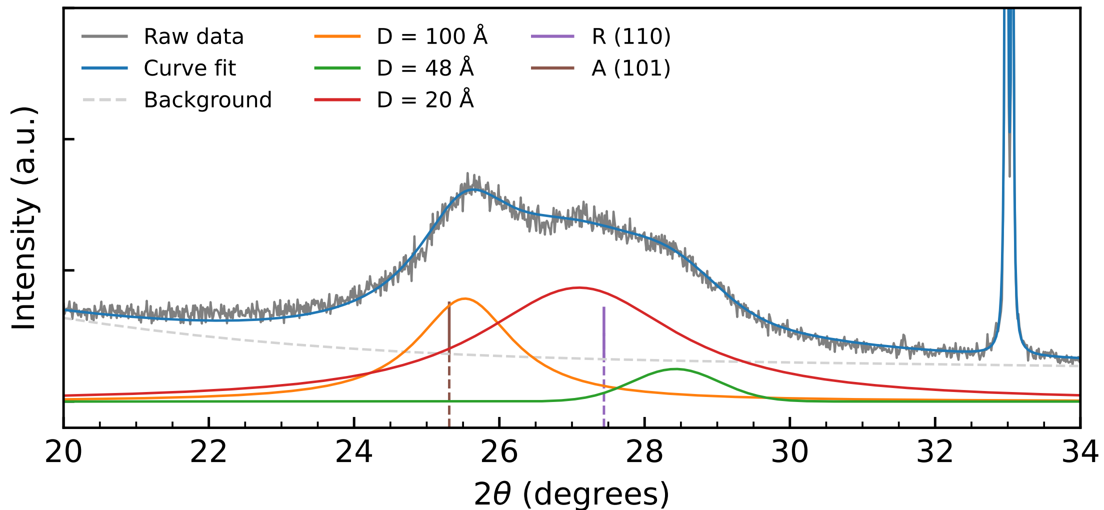

Figure 53: Details of the curve fit performed on XRD data from area 5 of CCS-Si-NoCap. The total fit is plotted along with the fitted background and individual functions. Rutile and anatase peak locations are also shown. The peak associated with $D = 48$ Å is attributed to CrO_2.

Raman spectroscopy results and discussion

The Raman spectroscopy results from CCS-Si-NoCap are shown in Figure 54. The data are plotted along with the reference spectra for rutile and anatase. Note that *two* locations were measured on Area 3—one at the center, and one closer to Area 2 (see Fig. 49 (a)). The acquired spectra show peaks with intensities that vary across the four measured areas.

For Area 2 (blue curve in Fig. 54), several prominent peaks can be seen which agree with the anatase reference spectrum. The most prominent of these is the distinct peak at 144.3 cm^{-1}. Peaks can also be seen at the 447.3 and 609.2 cm^{-1} rutile peak locations.

In Area 3 (orange curve), the peaks attributed to anatase rapidly fade away. Note, however, the dashed yellow line which represents the measurement on Area 3 *closer* to Area 2, (see Fig. 49 (a)). There, the anatase peak at 144.3 cm^{-1} is seen to be distinctly stronger than for the center of Area 3. This indicates a gradient of anatase concentration even across the individual areeas, which is expected from the combinatorial PLD method. Subtle traces of rutile may also be seen in Area 3 of Figure 54, similar to Area 2.

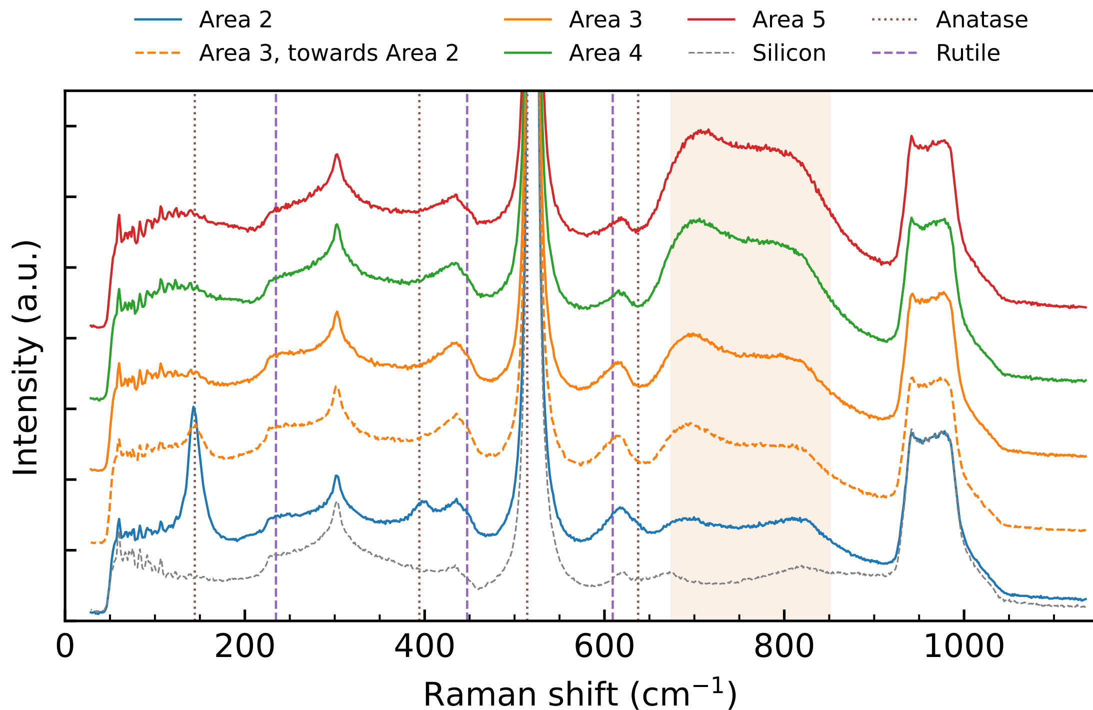

Figure 54: The Raman spectroscopy data from CCS-Si-NoCap. The data are plotted similarly to Fig. 63. Note that two measurements were made on Area 3—one at the center, and one towards Area 2. The peak positions of the anatase and rutile Raman spectra are shown for reference. Beige area indicates activity attributed to Cr–O bindings [59].

In Area 4 and 5, the distinct anatase peaks have diminished. However, a wide Raman band can be seen around 144 cm^{-1}. It is therefore suggested that the anatase phase has not completely disappeared, in agreement with the XRD discussion. As for the rutile peaks, it is hard to distinguish the rutile signature from the substrate signal in areas 4 and 5.

There is also an increasing amount of activity from Area 2 towards Area 5 in the 670–850 cm^{-1} range, as indicated by the beige area. This activity is attributed to increasing amounts of Cr–O bindings [59]. In view of the XRD results for Area 5, where CrO_2 was suggested to be present, it seems reasonable that this comes from amorphous CrO_2. This fits well with the Raman spectra described in ref. [59].

The Raman spectroscopy data generally outline a trend which resembles the XRD data for the same sample.

Summary

Summarized, the data indicate that the introduction of (Cr,N)-doping by the combinatorial PLD method has affected the structural composition of CCS-Si-NoCap. Growth parameters which (given no doping) would give polycrystalline anatase with (001) and (112) preferred orientations, are seen to give only the (001) anatase orientation for doping levels $\sim$ 3–5 at% Cr. For $\sim$ 7–9 at% Cr, anatase is still found, but with no obvious texture and lower crystalline quality.

Increased (Cr,N)-doping concentrations were generally seen to decrease the crystalline quality of rutile, *except* for the (100)-oriented grains, which grew stronger and sharper with increasing at% Cr levels.

Characteristics of CrO_2 were observed in both the XRD data and Raman spectra. The signatures were most prominent in Area 5, at the second plume center.

5.6.3 CCS-Si-Cap-Ref

The θ–2θ data from sample CCS-Si-Cap-Ref are shown in Figure 55, along with a thickness map of the sample, indicating the measured areas similar to in Fig. 48. Crosses denote (cyan) first plume center and (green) second plume center. Recall that during parts of the second plume center deposition, the gas was cycled to N_2. The XRD data from the four areas are displayed together with the calculated rutile powder XRD pattern, in addition to the A (110) and A (004) peak positions for the anatase phase.

For every area, several broad peaks may be seen, in addition to the sharp Si (200) peak at 32.98°. This indicates that crystalline materials are present in each area of the film. The peaks vary between areas, suggesting that there is a change in the structural composition across the sample. Specifically, some peaks are seen to increase and decrease in both intensity and width across the sample, indicating a change in the crystalline quality and structure from first to second plume center.

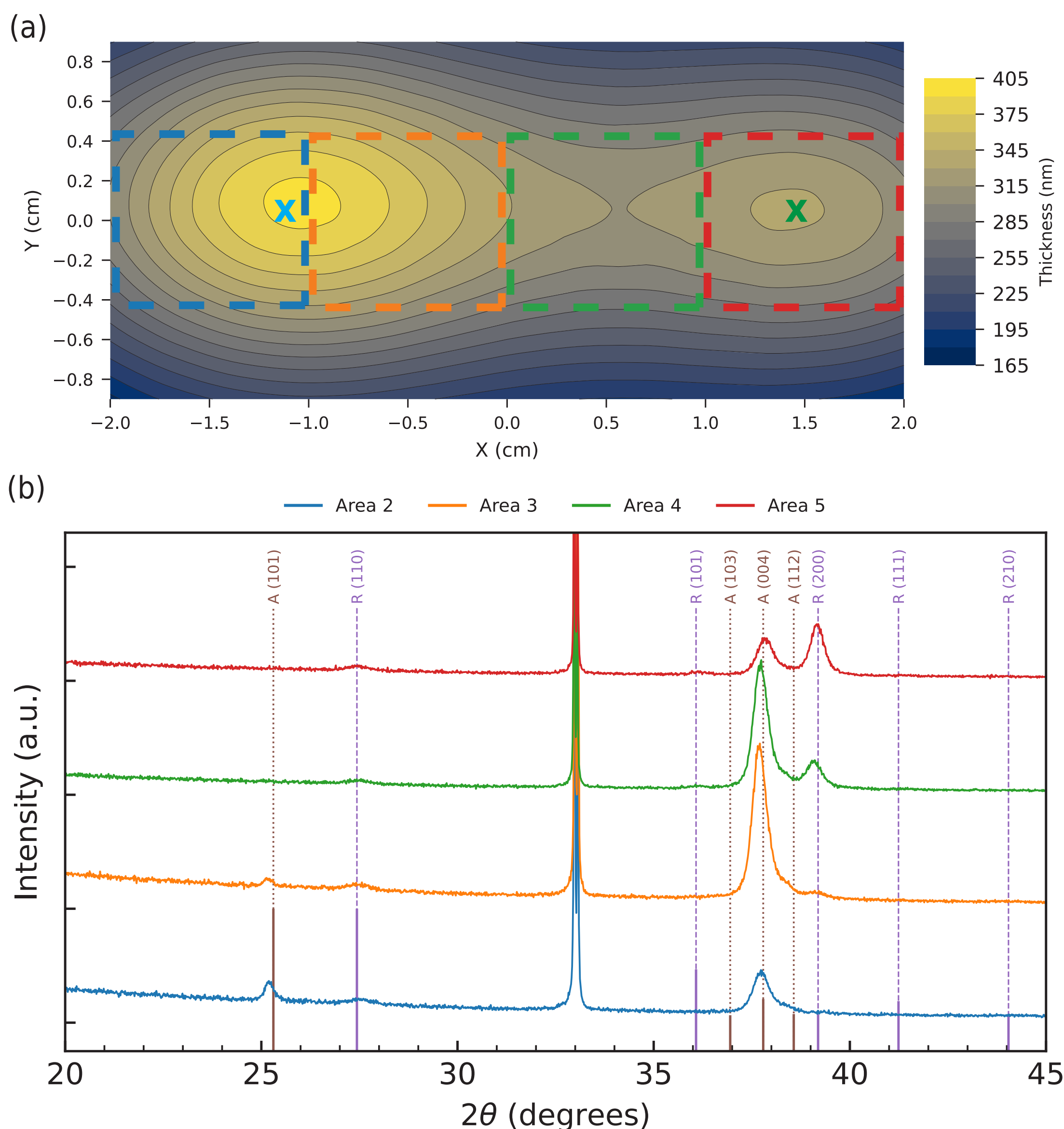

Figure 55: (a) Thickness map of sample CCS-Si-Cap-Ref, with the areas measured by XRD indicated in dashed boxes: (blue) Area 2, (orange) Area 3, (green) Area 4 and (red) Area 5. Crosses indicate (cyan) plume center deposited with pure O_2 flow and (green) plume center deposited with both O_2 and N_2 (see Fig. 20). (b) The θ–2θ diffractogram from the measured areas of CCS-Si-Cap. The substrate peak from Si(200) is seen at 32.98°. The rutile and anatase powder patterns are also shown for reference, with solid lines indicating relative powder XRD intensities, and dashed lines to guide the eyes.

By comparison with with CCS-Si-NoCap-Ref and B5 on Si, it seems plausible to attribute this change to the introduction of N_2 gas during parts of deposition.

A clear departure from what was seen for CCS-Si-NoCap-Ref (pure O_2 gas) is that the data indicates a higher degree of texture/preferred orientation for both the rutile and anatase phase. Whereas the CCS-Si-NoCap-Ref displayed polycrystalline anatase with (001) and (112) preferred orientations, Fig. 55 (b) shows a strong (001) preferred orientation for anatase in CCS-Si-Cap-Ref. However, a small shoulder can still be seen at the A (112) peak location. As for the rutile phase, there appears

to be a (100) preferred orientation in areas 3 to 5, which was not seen for CCS-Si-NoCap-Ref.

Three prominent trends can be seen from Figure 55: (1) the A (101) peak diminishes from first to second plume center, (2) the R (200) peak intensity increases from first to second plume center, and (3) the A (004) peak is strongest in areas 3 and 4, in between plume centers. It seems natural to attribute (1) and (2) to the higher concentration of TiO_2 deposited with N_2 gas (see Fig. 20). This is also supported by the observation that deposition in O_2–deficit gas conditions favored (100)-oriented rutile, as was seen in Section 5.1.

As for trend (3), it is suggested that a lower kinetic energy of ablated species in areas 3 and 4 have lead to the increased anatase (004) peak intensity (recall from Sect. 2.4 that the kinetic energy of ablated species should decline at increasing distances from the plume center). This is in agreement with ref. [45], where lower kinetic energy of deposited species was suggested to favor anatase growth, as a result of the anatase phase being more stable at lower temperatures.

Quantitative data analysis

Curve fits were performed on each area of sample CCS-Si-Cap-Ref, and the results are shown in Figure 56. The figure shows the total curve fit along with the raw data, in addition to the individual peak components and reference powder XRD lines for rutile and anatase. Only the 2θ ranges displaying crystalline peaks (except for the substrate peak) are shown.

The quantitative data as extracted from the curve fits are displayed in Figure 57. The presentation and parameters are the same as what was presented in Section 5.1.

As seen in Figure 56, there is good agreement when fitting Lorentzian functions onto the data, and the results underline the previous qualitative discussion of the results. In particular, the data in Fig. 57 (a) shows the intensities of the A (004) and A (112) peaks increase towards Area 4 and then decline. On the other hand, the A (101) peak decreases immediately and completely disappears in Area 4. The estimated crystallite sizes for the A (004) peaks also increase together with the intensities as seen from Fig. 57 (d).

The degree of preferred orientation with respect to the A (001) planes is also apparent from Fig. 57 (e), where the texture coefficient increases from $\gamma_{004} = 1.31$ to 1.86 between areas 2 and 3, respectively. Note that texture coefficients for the anatase phase were not calculated in areas 4 and 5 because *only* the A (004) peak was observed—meaning that γ_{hkl} in principle is infinite. However, it is also possible that more randomly oriented anatase also exists in Area 5, but that the signal is simply too weak to be detected.

The trends observed for the rutile phase in Figure 57 also confirm the qualitative observations derived from the XRD data. The R (200) peak intensity increases steadily from Area 3 to Area 5, together with an increase in estimated crystallite size and texture coefficient. The quantitative data therefore agrees with the rutile

phase growing more (100)–textured, with increasing crystalline quality, when moving from Area 2 to 5.

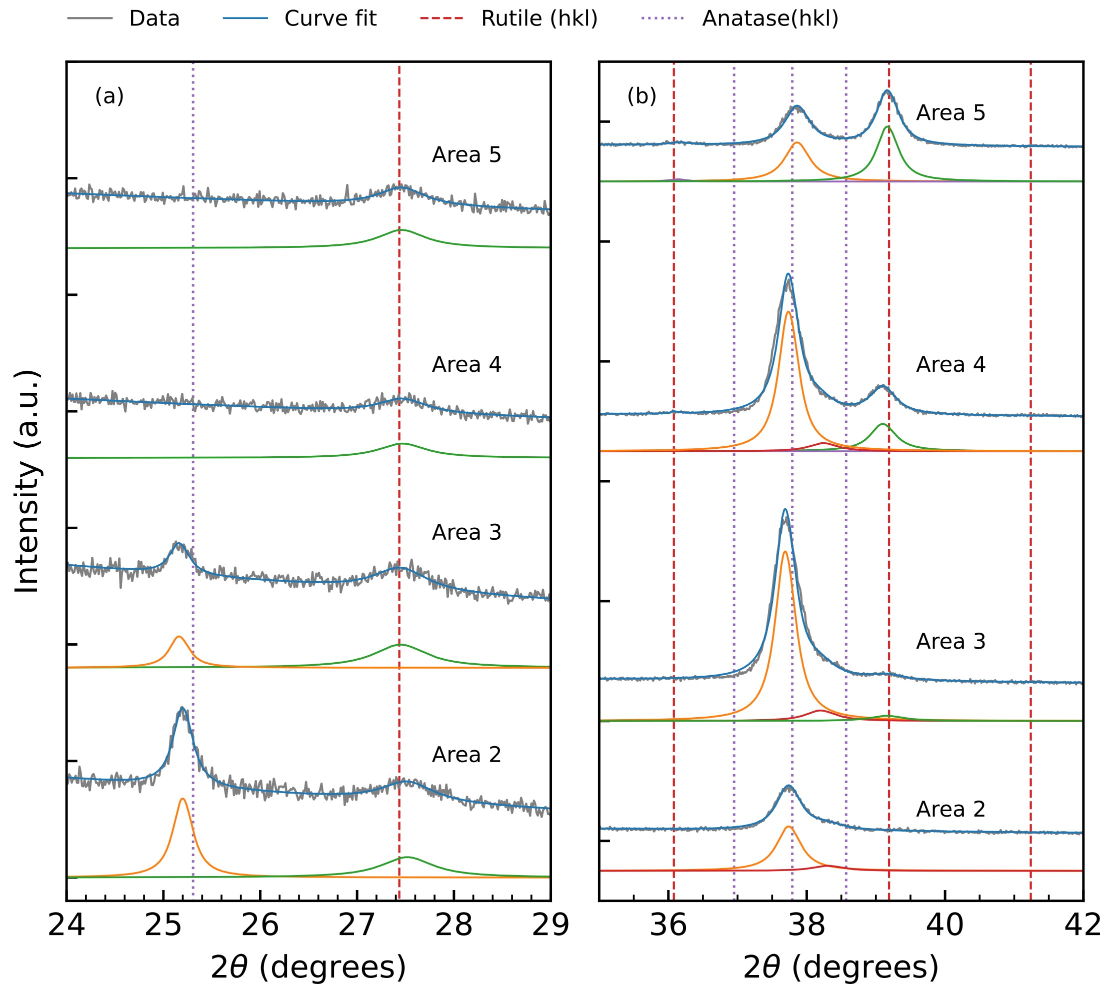

Figure 56: Details of curve fits performed on XRD data from CCS-Si-Cap-Ref. Left: Details of the curve fits and their individual components, in the 24–29° range. Right: The same, but for the 35.5–42° range. Peak locations for rutile and anatase are also shown.

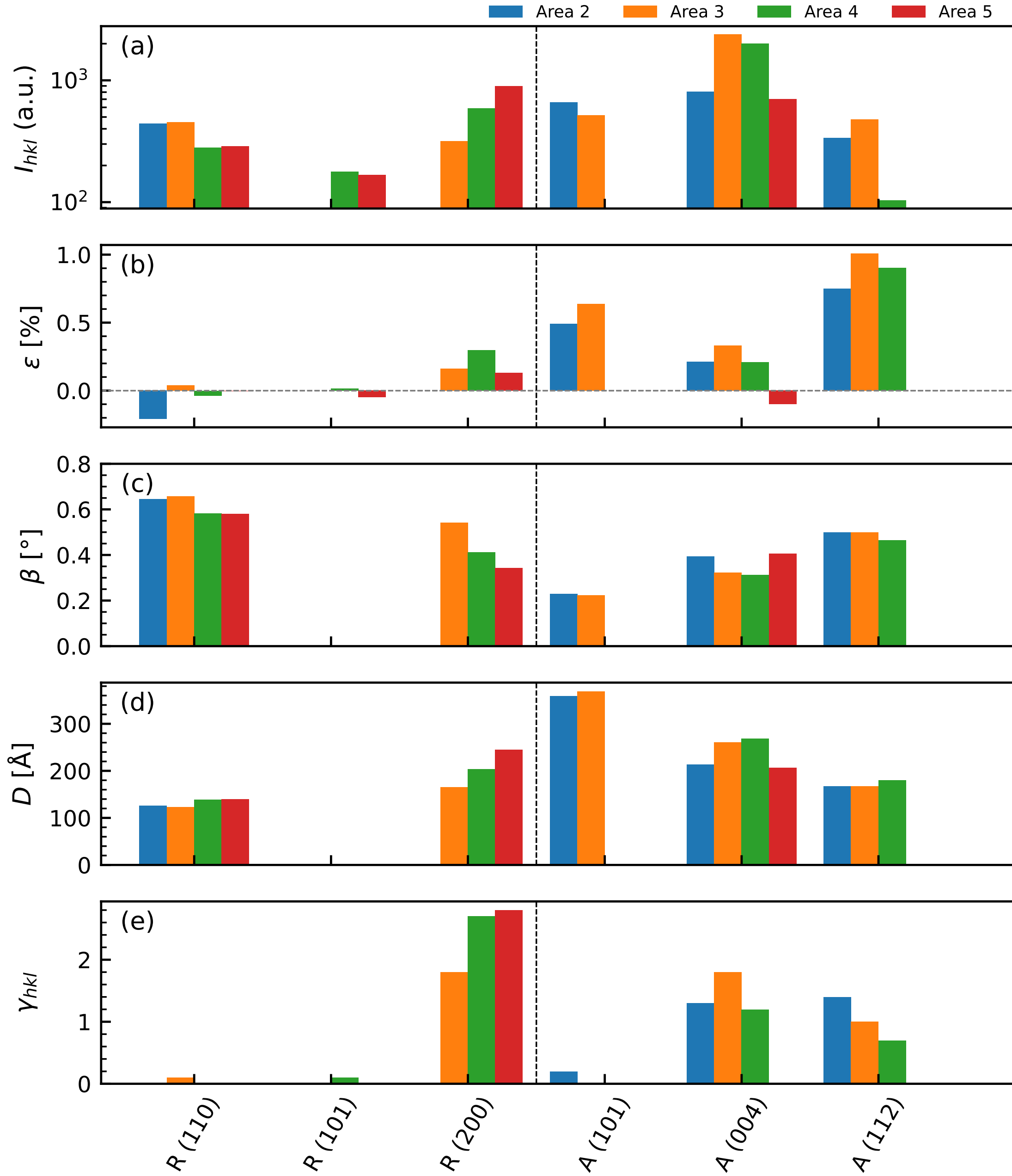

Figure 57: Quantitative data from the curve fits of CCS-Si-Cap-Ref: (a) integrated intensity I_{hkl}; (b) measured strain ϵ; (c) full-width-half-maximum β; (d) estimated mean crystallite size D; (e) texture coefficient γ_{hkl}. Black, dashed line separates rutile and anatase planes.

5.6.4 CCS-Si-Cap

XRD Results and discussion

The θ–2θ scans of the four areas of sample CCS-Si-Cap are shown in Figure 58 (b), with a thickness map of the sample in Fig. 58 (a). The data are plotted in a similar manner as in Section 5.6.1, with indications of approximate Cr doping levels. The

calculated powder XRD pattern for rutile, in addition to the A (004) peak position are also shown.

In the figure, several distinct peaks are seen for areas 2 and 3 (blue and orange curves), indicating existence of crystalline components in the film. All peaks lie in the proximity of some (hkl) line of rutile or anatase, which are also displayed. In areas 4 and 5 (green and red curves), only the Si(200) peak at 32.98° is visible, indicating that no crystalline materials were detected in the film. Note also the wide bump at low angles, seen in all positions, indicating amorphous materials.

Qualitatively, the data for areas 2 and 3 show some similar trends as for the reference sample. Recall that in the reference sample, textured anatase with a (001)-preferred orientation and textured rutile with a (100)-preferred orientation were observed.

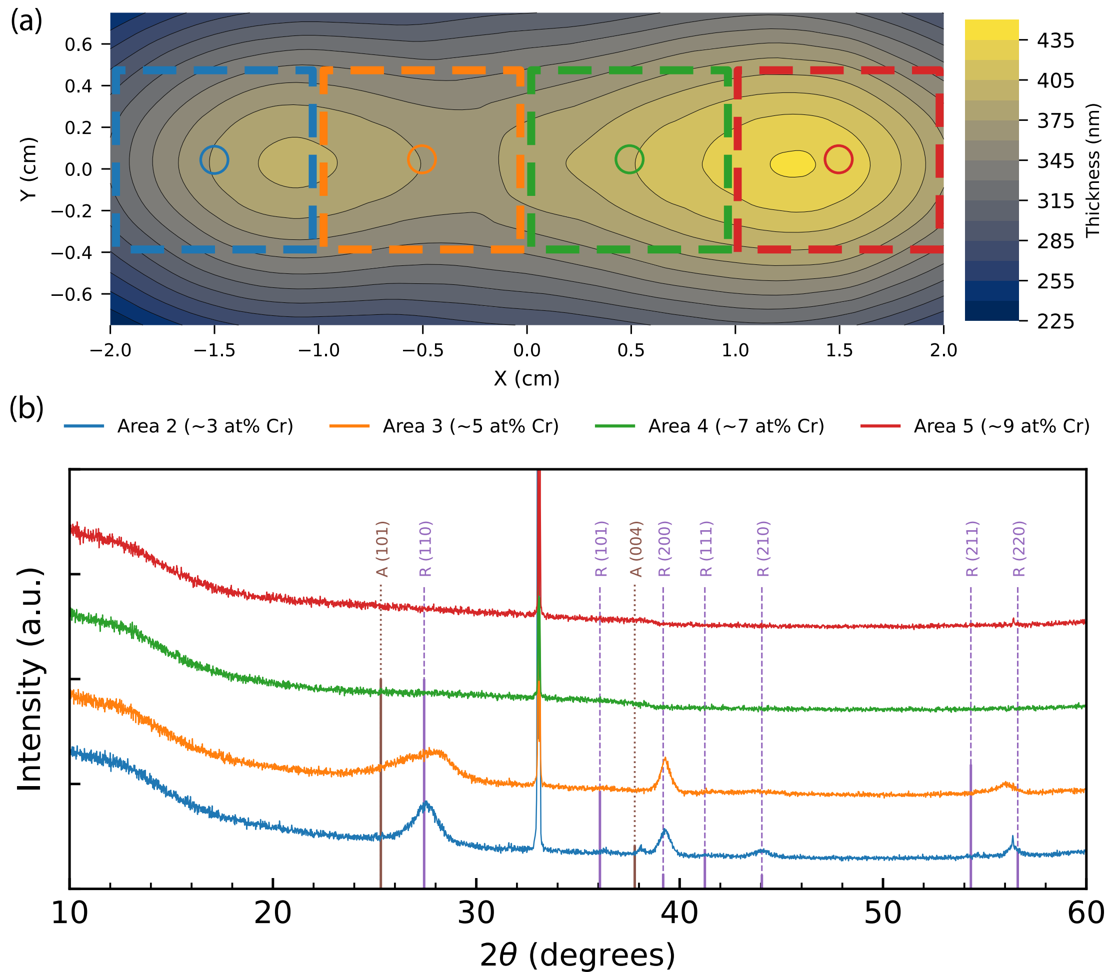

Figure 58: (a) Thickness map of sample CCS-Si-NoCap, with the areas measured by XRD indicated in dashed boxes: (blue) Area 2, (orange) Area 3, (green) Area 4 and (red) Area 5. Circles indicate the approximate locations where Raman measurements were made. (b) The θ–2θ diffractogram from the measured areas of CCS-Si-Cap. The substrate peak from Si(200) is seen at 32.98°. The rutile and anatase powder patterns are also shown for reference, with solid lines indicating relative powder XRD intensities, and dashed lines to guide the eyes.

In contrast to CCS-Si-Cap-Ref, however, the rutile (200) peak is already prominent for Area 2 in Fig. 58 (b), whereas the anatase (004) peak is considerably weak. In position 3, the anatase (004) peak has completely disappeared, while the rutile (200) peak has grown stronger. Furthermore, the rutile (110) peak at $2\theta = 27.44°$ has broadened, with a skewness towards lower angles. The details of this skewness will be discussed in relation to the curve fits, to be presented below.

Quantitative data analysis

Curve fits were performed for areas 2 and 3. The fits are displayed together with the raw data in Figure 59, with the quantitative results displayed in Figure 60. The presentation is mostly similar to that of Section 5.6.1. The only difference is that instead of calculating the texture coefficient γ_{hkl}, the quantity I/I_0 was used (see Sec. 3.2.4 for explanation).

The quantitative data in Figure 60 underline the qualitative observations. Fig. 60 (a) shows that the intensities of all peaks, *except* for the R (200) peak, decrease from Area 2 to Area 3. The mean crystallite size from the R (200) peak was estimated to increase slightly from Area 2 to Area 3. This occurred together with an increase in intensity and I/I_0 value, as well as decrease in estimated strain.

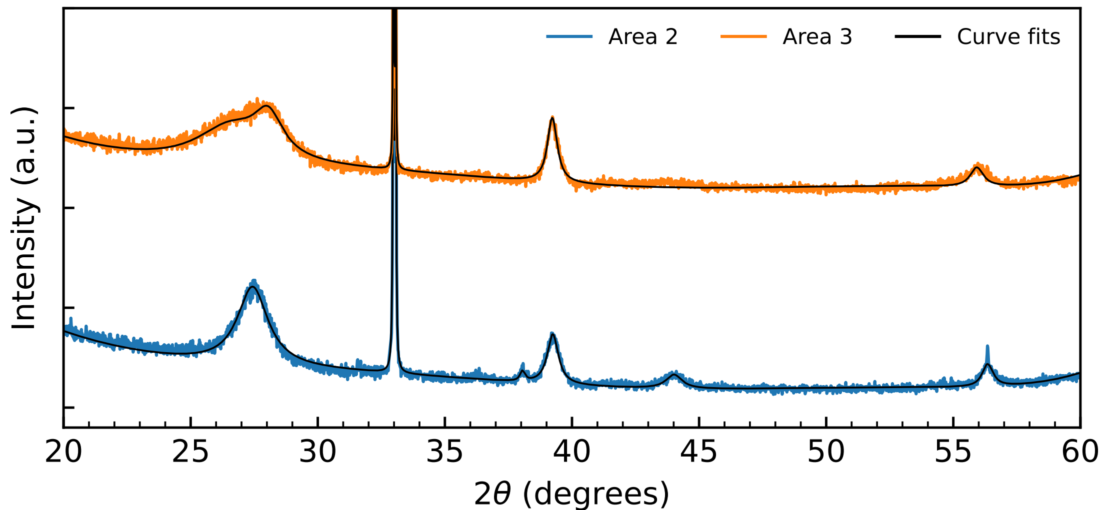

Figure 59: Plot of the curve fits performed on XRD data from CCS-Si-Cap.

A detail of the curve fit on Area 2, in the 2θ range from 35° to 42° is shown in Figure 61. There is fairly good agreement when fitting a Lorentzian peak at $2\theta = 38.02°$, which lies closest to the anatase (004) peak location. Since no other anatase peaks are visible in the full scan of Figure 58, it is difficult to confidently attribute this peak alone to the anatase phase. However, based on the insight from the reference sample in Section 5.6.3, (001)-oriented anatase is expected for these deposition parameters. Therefore, it is probable that anatase with a (001)-preferred orientation is indeed found in Area 2 of sample CCS-Si-Cap, albeit with weak intensity and some strain, as quantified in Fig. 60 (b). Note that the estimated $D = 452\,\text{Å}$ is likely

vastly overestimated due to the low intensity of the peak (but note again that this parameter is to be interpreted qualitatively).

As seen in Figure 60 (b)–(d), the data for Area 2 indicate strain of less than 1% for all peaks. The crystallite sizes for the rutile phase are estimated in the range of 60 Å to 170 Å. The smallest D estimate is for the R (110) peak and the largest is for the R (200) peak.

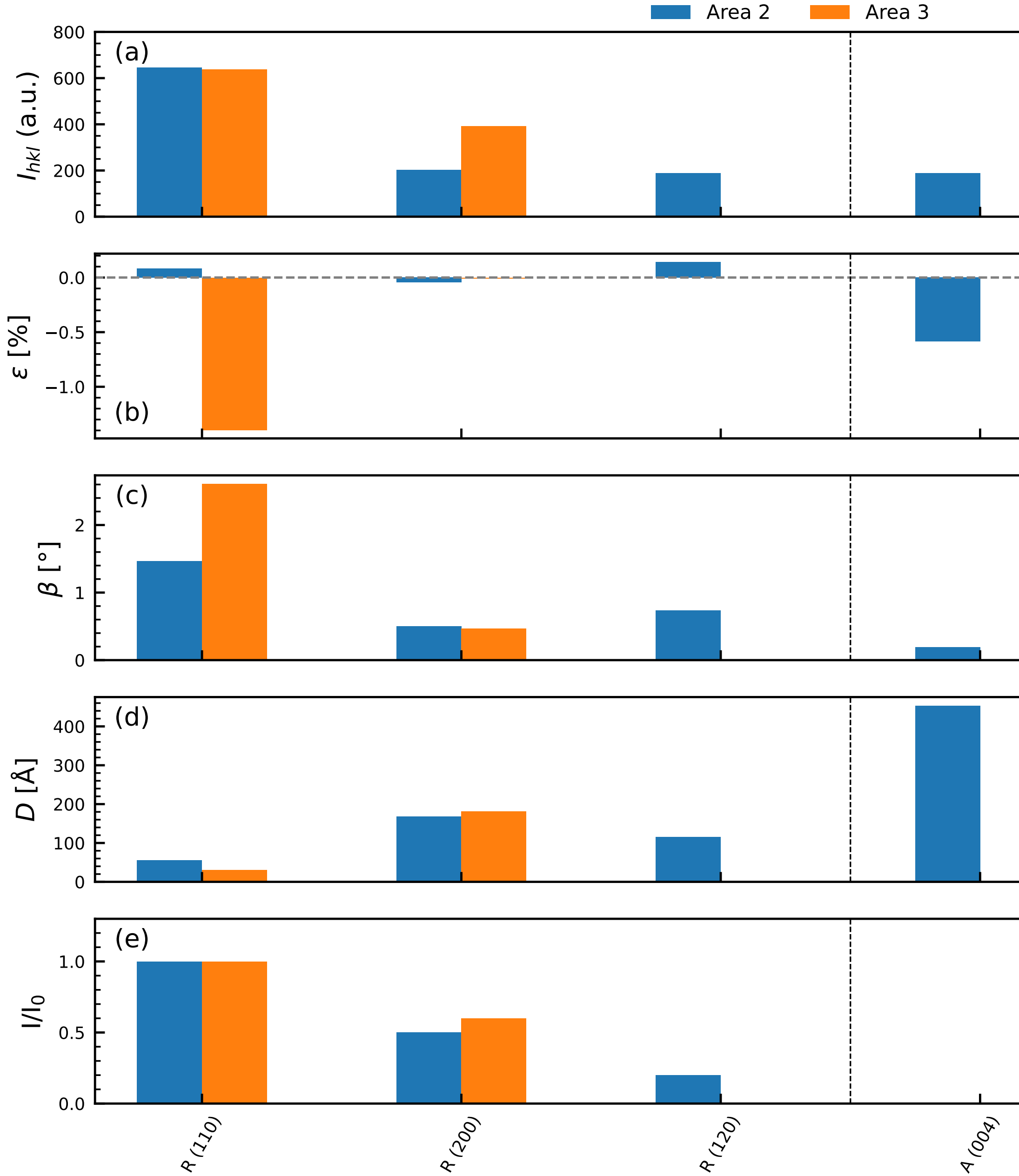

Figure 60: Quantitative data from the curve fits of CCS-Si-Cap: (a) integrated intensity I_{hkl}; (b) measured strain ϵ; (c) full-width-half-maximum β; (d) estimated mean crystallite size D; (e) I/I_0, a substitute for the texture coefficient. Black, dashed line separates rutile and anatase planes.

The R (110) peak that was seen for Area 3 in Figure 58 is significantly asymmetric. For the curve fit, this was accounted for by fitting two Lorentzians, which is shown in Figure 62. The first peak gave a crystallite size estimate of 57 Å. while the other gave an estimate of 24 Å. The latter value is smaller than the lattice constants of rutile and anatase, suggesting "amorphous-like" rutile or anatase. Similar to what was suggested for CCS-Si-NoCap, the peak at $2\theta \approx 28.1°$ could also come from CrO_2. The peak broadening of R (110) towards lower angles could also come from Cr_2O_3 (see Fig. B.1 in Appendix B).

The asymmetry seen in Figure 62 could be due to non-uniform strain of the rutile phase, but it seems more likely to attribute this to an anatase contribution at approximately 25.3°. The Lorentzian associated with $D = 24$ Å in figure 62 would then be associated with the anatase phase. This would suggest that anatase also exists in Area 3 of the sample, similar to the (CCS-Si-Cap-Ref), but with severely decreased crystalline quality, and no observable texture (since only the "characteristic" powder peak is observed).

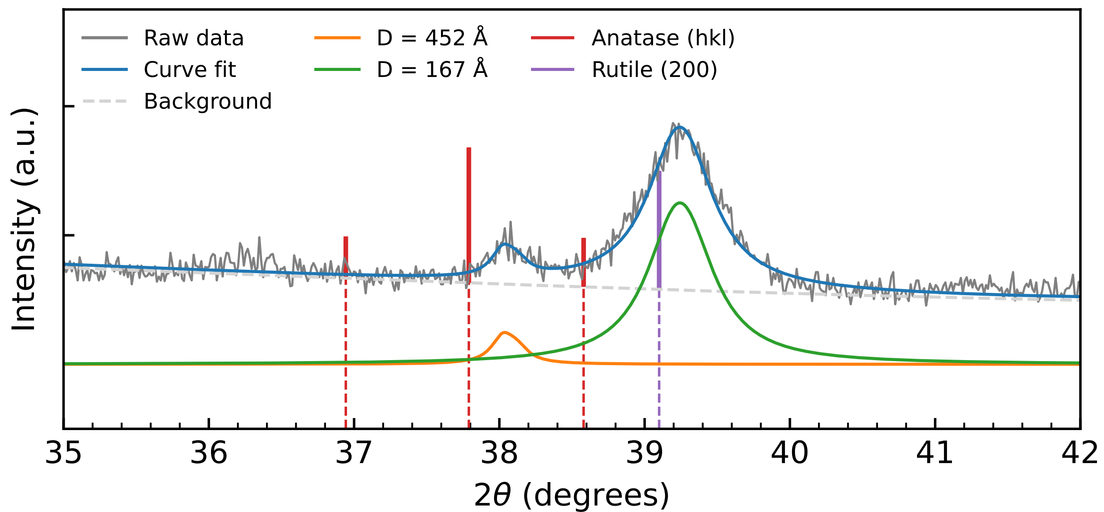

Figure 61: Details from the curve fit performed on XRD data from Area 2 of CCS-Si-Cap. The total fit is plotted along with the data, fitted background and individual functions for each peak.

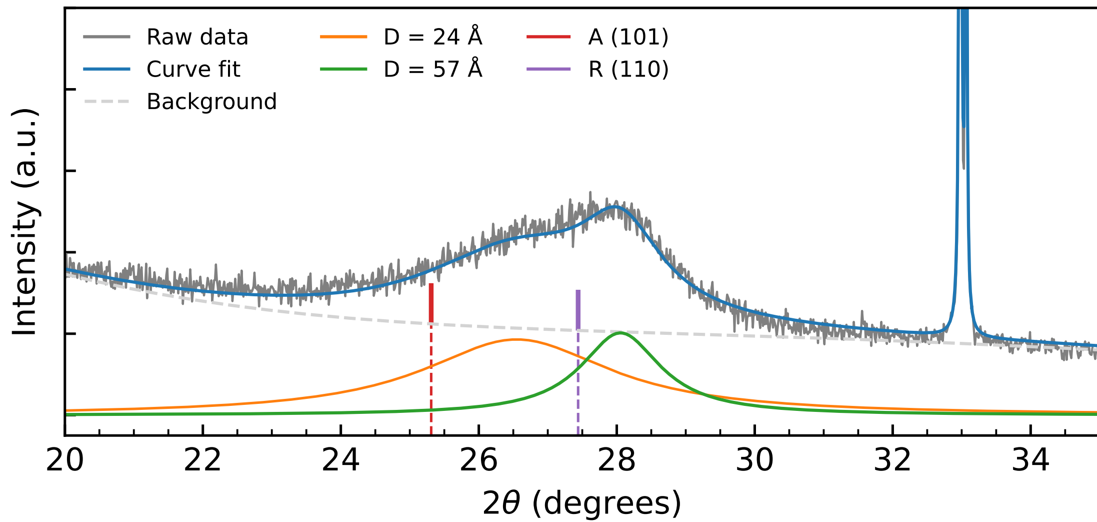

Figure 62: Details from the curve fit performed on XRD data from Area 3 of CCS-Si-Cap. The total fit is plotted along with the data, fitted background and individual functions for each peak.

Raman spectroscopy results and discussion

The Raman spectroscopy data for acquired from CCS-Si-Cap is shown in Figure 63. The spectra were acquired from the positions described in Fig. 58 (a). Spectra from all four areas are plotted along with the substrate signature and reference lines for the anatase and rutile Raman spectra.

The highest amounts of activity can be seen for Area 2 and 3 (blue and orange in Fig. 63, respectively). This agrees well with the XRD data from Figure 58. In fact, peaks are visible at the rutile locations reference which exceed the expected signal from the substrate. Note also the difference between the substrate signature and the spectrum from areas 2 and 3 at $\sim 144\,\text{cm}^{-1}$. The wide band which can be seen at this Raman shift location indicates anatase existing in both areas 2 and 3, supporting the discussion based on the XRD data.

The silicon signatures in Figure 63 seem to diminish from Area 2 through 5. This is especially apparent when comparing the film signal to the substrate reference in Figure 63. This indicates that the sample absorbs a larger fraction of the incident laser areas.

Similar to what was seen for CCS-Si-NoCap, activity in the 670–850 cm^{-1} (beige area) is attributed to Cr–O bindings [59], which may come from amorphous–like CrO_2 or Cr_2O_3, based on the XRD analysis.

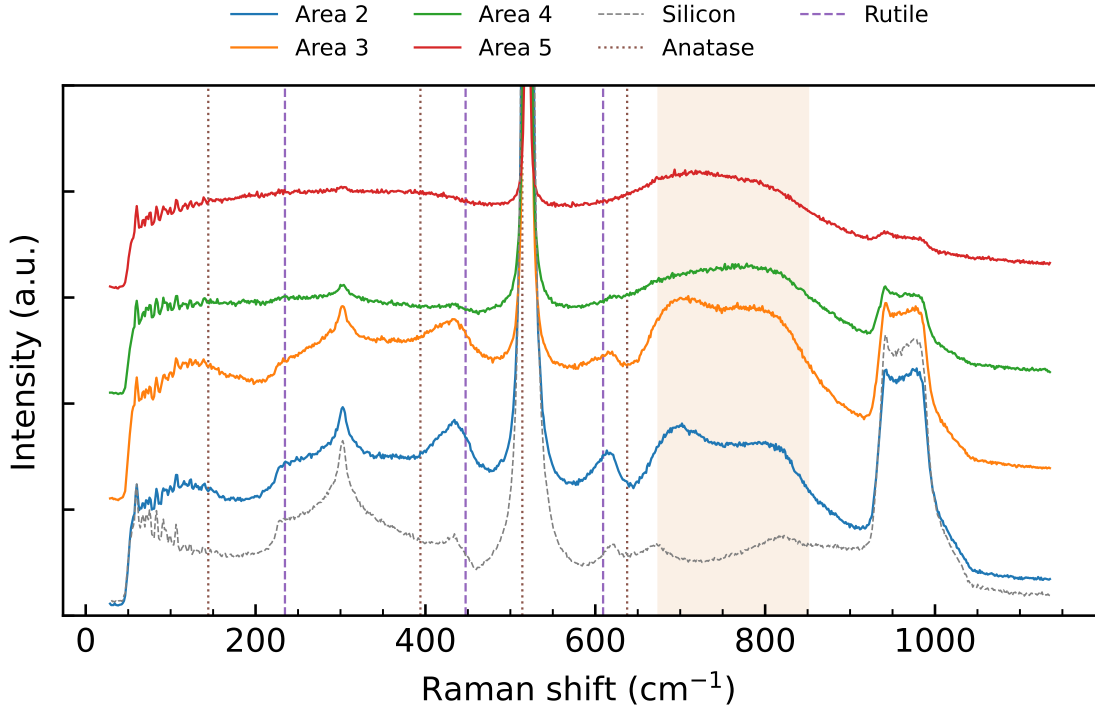

Figure 63: The Raman spectroscopy results of sample CCS-Si-Cap. The data from each measured positoin is plotted, along with the silicon substrate signature. The lines of the anatase and rutile spectra are shown for reference. Activity in the beige area is attributed to Cr–O bindings [59].

Summary

Summarized, the data indicate that the introduction of N_2 gas during parts of the deposition has considerably affected the structural composition of the samples, when compared with the samples described in Section 5.6.1.

For the reference sample (no (Cr,N)-doping), using N_2 gas during parts of the TiO_2 target ablation affected the phase composition and texture in the films. CCS-Si-Cap-Ref showed mostly (001)-oriented anatase and (100)-oriented rutile. The R (200) peak intensity increased substantially towards the second plume center. It is therefore suggested that depositing TiO_2 using pure N_2 gas favors (100)-oriented rutile. Recall from Section 5.1.1 that low-oxygen deposition parameters increasingly favored rutile with a (100) preferred orientation. Based on this, we can speculate that the lack of oxygen when depositing under N_2 gas is what causes the increased rutile (100) growth.

A minor observation is that areas 3 and 4 (in between plume centers) gave the strongest anatase (001) signals from CCS-Si-Cap-Ref. A lower kinetic energy of ablated species is expected at a distance from the plume centers. This finding therefore supports that lower kinetic energy favors anatase phase growth, in agreement with ref. [45].

Introduction of (Cr,N) doping was seen to severely decrease the crystalline quality

of the sample, when comparing CCS-Si-Cap-Ref with CCS-Si-Cap. The quality decreased for areas with increasing at% Cr levels. This suggestion is also in agreement with other characterization works made on similar samples, such as by Rosnes [37].

A further remark is that the overall quality of the CCS-Si-Cap was significantly lower than the *uncapped* CCS-Si-NoCap sample, where crystalline characteristics were observed in all positions. The highest crystalline quality estimate has so far been for Area 2 (∼3 at% Cr) of CCS-Si-NoCap, where highly textured (001)-oriented anatase was found. It is therefore suggested that the capping of the CrN layer has come at a great cost to the anatase crystalline quality.

5.6.5 CCS-LAO-Cap

The results of the θ–2θ scan for sample CCS-Lao-Cap is shown in Figure 64. No thickness map is available for this sample, but the areas correspond to (Area 1) low (Cr,N)-doping, (Area 2) medium (Cr,N)-doping and (Area 3) high (Cr,N)-doping.

Owing to rather weak signals, the figure displays the data in logarithmic scale, with the scans from each position in separate plots. Several distinct peaks are observed, many of which are sharp substrate artifacts, as well as, broader peaks which indicate crystalline materials in the film. In Figure 64 (a), the rutile powder XRD pattern as well as the anatase (004) peak location are shown. Note that because the sample was deposited on a LAO substrate, a large amount of substrate artifacts can be seen as a result of contamination from the Cu X-ray spectrum, similar to the undoped samples in Section 5.2.

Visual, qualitative analysis of Figure 64 (a) reveals that a number of—albeit small—peaks coincide with the rutile (hkl) pattern. Most of the peaks measured low intensity ($\sim 2 \times 10^2$ counts), except for the R (200) peak at $2\theta \approx 39.19°$, which peaked at $\sim 1.3 \times 10^4$ counts. This qualitative result indicates that polycrystalline rutile exists in Area 1 of CCS-LAO-Cap, with a prominent (100) preferred orientation.

A peak is also observed close to the anatase (004) peak location at $2\theta = 37.79°$. Based on Raman characterization of the sample (to be presented below), anatase is expected to be found in the sample, and it therefore seems reasonable to indeed assign this peak to the A (004) reflection. This result also agrees with what was observed for the undoped samples on LAO in section 5.2, where textured, (001) oriented anatase was observed, *in addition* to polycrystalline rutile.

In Area 2, seen in Figure 64 (b), the rutile signature has completely disappeared. Only a small peak close to the A (004) angle is observed. It therefore seems that the only crystalline TiO_2 found in Area 2 is textured, (001)-oriented anatase, although the measured intensity is small ($\sim$ 500 counts) compared with Area 1 ($\sim$ 4000 counts). Presumably, based on the lack of any polycrystalline signal, the other parts of the area comprised of TiO_2, if any exist, are amorphous.

In Area 3, seen in Figure 64 (c), no traces of TiO_2, neither rutile nor anatase, are observed.

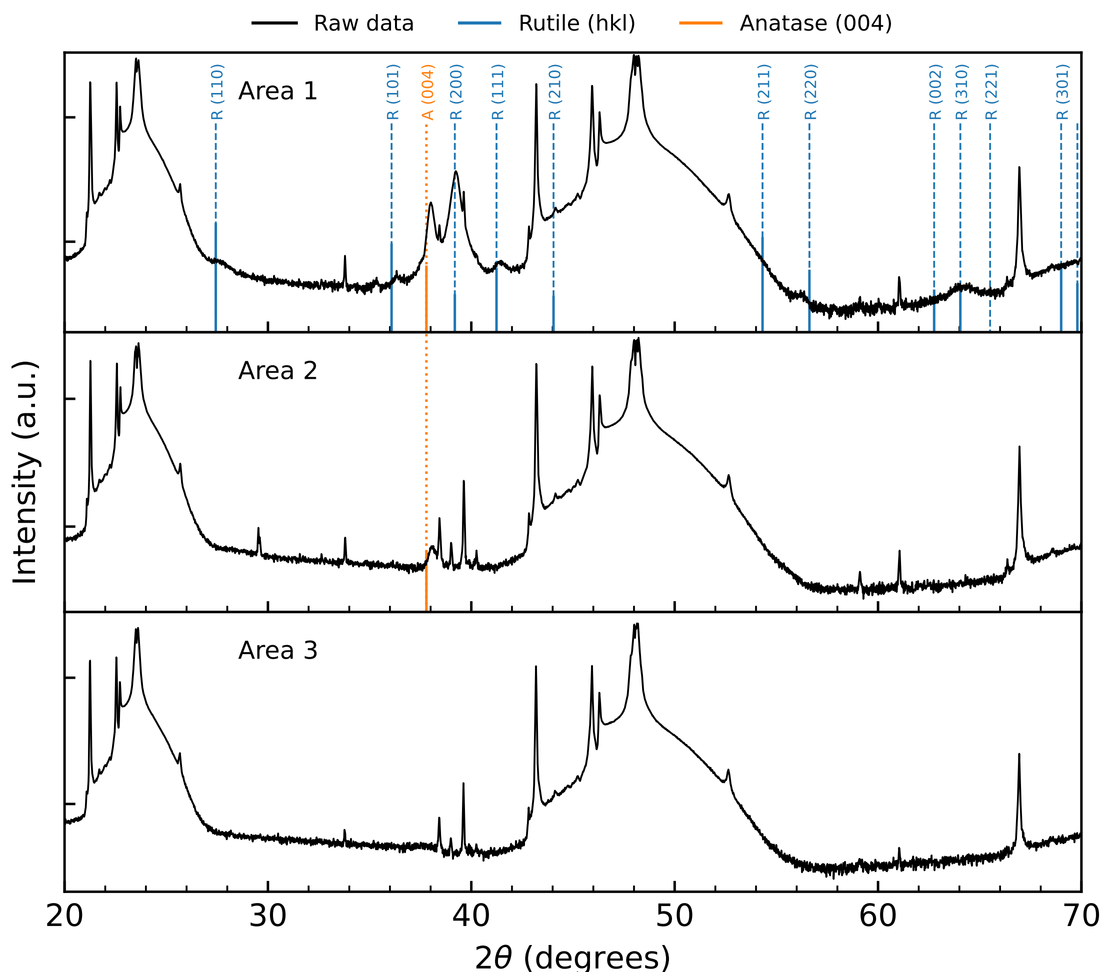

Figure 64: Logarithmic-scale plot of θ–2θ data for CCS-LAO-Cap; Area 1 (low doping), Area 2 (medium doping), Area 3 (high doping). The rutile powder diffraction pattern is shown in solid blue lines, with added dashed lines to guide the eyes. For anatase, only the (004) line is shown.

Raman results and discussion

The acquired Raman spectra for CCS-LAO-Cap are shown in Figure 65. The spectra from the three positions are plotted together with the substrate spectrum and reference spectra from rutile and anatase.

In Area 1, peaks may be seen close to the rutile bands at 447.3 and 609.2 cm^{-1}, indicating existence of rutile in agreement with the XRD data. The peaks are not visible in areas 2 and 3, indicating that the rutile phase has disappeared, which is also in agreement with the XRD data.

As for the anatase phase, the most prominent peak would be expected at 144 cm^{-1}, but from Figure 65 it is hard to tell whether any activity from anatase is registered in areas 2 and 3, because of the prominent substrate signature.

Recall from the XRD analysis of Figure 64 that (001)-oriented anatase was sugges-

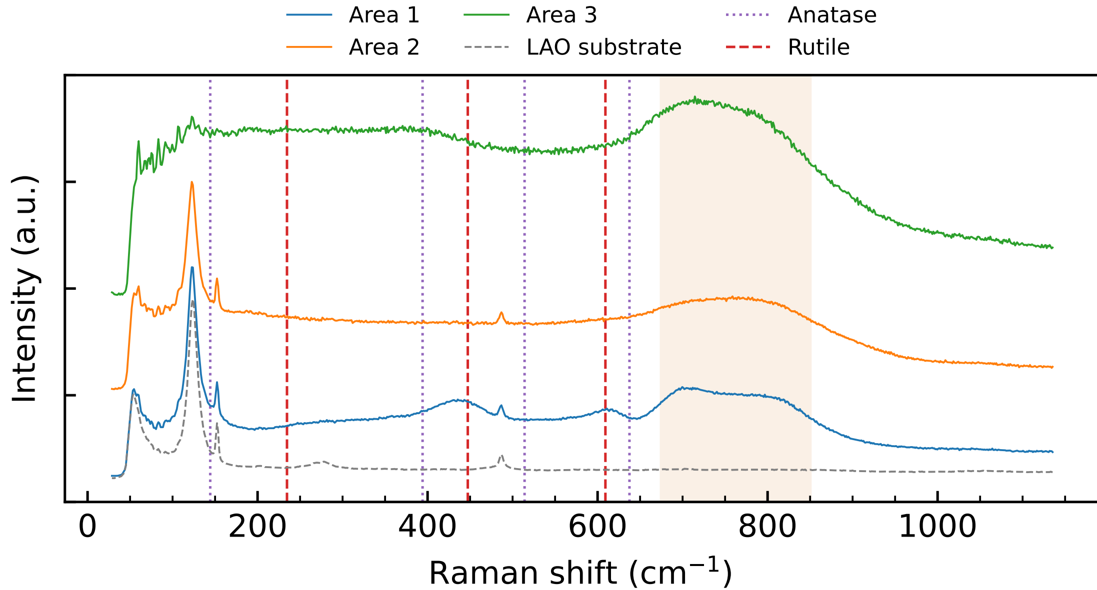

Figure 65: The Raman spectroscopy data from CCS-LAO-Cap. The data are plotted similarly to Fig. 63. Note that two measurements were made on position 3—one at the center, and one towards position 2. The peak positions of the anatase and rutile Raman spectra are shown for reference. Beige area denotes activity attributed to Cr–O bindings [59].

ted, but the measured intensity was considerably weak. This could translate into the Raman data in that the anatase signal may be too weak to be distinguished from the LAO signature.

Note that even the substrate signature seems to have disappeared in Area 3 of Figure 65, suggesting that the sample is more absorbing in this area.

Similar to the previously described doped samples, some activity is attributed to Cr–O bindings (beige area).

Recall from sections 5.1, 5.2 and 5.3 that on LAO and STO, textured anatase (001) was grown even in conditions which seemed to favor rutile. The growth was attributed to the small lattice mismatch of the two substrates with the anatase (001) orientation. It was also argued by comparison with the samples on Si (SiO_2) substrates, where samples B3 and B4 showed only polycrystalline rutile with (100) preferred orientation, whereas samples B3 and B4 on LAO and STO showed textured (001)-oriented anatase, in addition to the polycrystalline rutile. It therefore seems appropriate to consider that lattice matching with LAO could be the cause of the anatase (001) texture for sample CCS-LAO-Cap.

However, textured anatase (001) was also observed on some of the undoped samples on Si. This was most prominent in sample A2 on Si, and also somewhat prominent in sample B5 on Si. Additionally, anatase (001) was also observed on both of the undoped samples on Si (secs. 5.6.1) and 5.6.4. Because of this, it is difficult to state whether the textured anatase (001) observed in Figure 64 arised as a result of lattice matching with LAO, or as a result of growth conditions favoring (001)

oriented anatase. It would make sense that increasing dopant concentrations would obstruct the initial, substrate–forced growth, resulting in quenching of the anatase signal in areas 2 and 3. However, the same quenching of anatase (001) was also observed on the undoped samples on Si, which weakens the argument for lattice matching.

5.7 Summary of Discussion from Characterization of CCS Samples

This section will discuss the overall interpretation of the results and discussion presented in Section 5.6.

In Section 5.6.1, it was seen that the introduction of (Cr,N)-doping by combinatorial PLD significantly affected the structural characteristics of the TiO_2 films. Recall that CCS-Si-NoCap was deposited with similar parameters as sample B5 on Si in Section 5.1. This was also evident when investigating CCS-Si-NoCap-Ref, which was grown similar to CCS-Si-NoCap except that it had no doping and thus is the film most resembling the growth of B5 on Si. It was also seen from the XRD data. Quantitative data from CCS-Si-NoCap will be compared to the data from B5 on Si, as no quantitative data analysis was made for the reference sample.

At the first plume center (Area 2, ∼3 at% Cr) the (Cr,N) of CCS-Si-NoCap, doping was found to significantly alter the anatase characteristics in XRD. Only the (001) orientation was observed, but the estimated crystallite size was in fact higher than for the same orientation in B5 on Si. However, the calculated strain estimate was considerably higher for the doped sample. For the rutile phase in CCS-Si-NoCap, the introduction of (Cr,N) did not seem to alter the characteristics at the first plume center, compared with B5 on Si. The Raman spectra confirmed these observations.

Between the first plume center and wafer center (Area 3, ∼5 at% Cr) of CCS-Si-NoCap, the anatase signal was severely diminished. However, only the (001) anatase orientation was observed at this position, which indicates that it was also textured at this position. Based on this finding, we could speculate that the higher (Cr,N) doping levels negatively affected the anatase growth *rate*, but that the growth mechanisms (which resulted in the textured growth) were not significantly affected.

For the rutile phase in CCS-Si-NoCap, the higher introduction of higher (Cr,N) doping concentrations at Area 3 seemed to favor the (100) orientation of rutile. This was indicated by the texture coefficient γ_{hkl} increasing, as well as the estimated crystallite size. No significant strain effects were observed.

These trends continued into areas 4 and 5 of CCS-Si-NoCap, towards the second plume center. The data indicates that increasing doping concentrations for this sample negatively affected the crystalline quality of its rutile and anatase components, *except* for the (100) oriented rutile grains. The former showed increasingly amorphous–like characteristics, while the latter ((100) oriented rutile) yielded increasingly stronger XRD peaks, with increasing texture coefficients and estimated mean crystallite size. The findings indicate that (Cr,N) of TiO2 with these c-PLD

parameters favors textured rutile with a (100) preferred orientation.

For CCS-Si-Cap-Ref (no doping, but cycling between O_2 and N_2 gas), it was seen that the introduction of N_2 during the deposition affected the structural composition of the film. For the anatase phase, it was seen that all peaks except for the A (004) peak were quenched, as compared to B5 on Si. Furthermore, the A (004) peak was strongest closer to the wafer center (areas 3 and 4). It was speculated that this was due to lower kinetic energy of ablated species, similar to a suggestion from ref. [45]. However, this does not explain why such a trend was not observed for CCS-Si-NoCap-Ref.

As for the rutile characteristics in CCS-Si-Cap-Ref, it seems that the introduction of N_2 gas led to similar trends as was seen for CCS-Si-NoCap. That is, the rutile showed increasing degrees of (100) preferred orientation moving from the first to second plume center. It is suggested that this is at least partly due to the second plume center consisting of more species deposited without O_2 gas, as this was seen to favor rutile (100) growth in sections 5.1–5.4.

One could also speculate that it is the presence of nitrogen itself that causes the (100) preferred orientation for rutile. This could explain why the same trend was seen for CCS-Si-NoCap, which was not deposited under N_2 gas but was subjected to (Cr,N)-doping. The physical process that resulted in these trends has not been investigated.

Similar to for the undoped uniform samples in Section 5.5, no correlation between rutile (100) planes and anataes (112) planes could be found. It is therefore suggested that the anatase–to–rutile transformation at anatase (112) twin boundaries has not occured.

For CCS-Si-Cap, the introduction of (Cr,N)-doping *with* capping severely affected the structural characteristics of the film. At the first plume center (Area 2), the A (004) (as well as other anatase peaks) had almost completely disappeared compared with the previously mentioned samples. The data from Area 3 showed no A (004) peak at all, but a small shoulder from A (101) may have caused peak broadening of the R (110) peak.

For the rutile phase in CCS-Si-Cap, the degree of (100) preferred orientation was already prominent at the first plume center, and seemed to increase towards the wafer center. This finding was also confirmed by Rosnes, who studied a similar sample by Transmission Electron Microscopy [37]. It could therefore be suggested that, compared to the previously discussed samples, the combination of (Cr,N)-doping and capping of the CrN layer increasingly favored the (100) orientation of rutile. This is also somewhat surprising since CCS-Si-Cap was deposited with substrate temperature $\sim 550\,^{\circ}\mathrm{C}$, which is believed to favor anatase [22].

Across the wafer center and towards the second plume center (areas 4 and 5) of CCS-Si-Cap, no film peaks were seen. This indicates mostly amorphous materials, which was also confirmed by Rosnes. It therefore seems that (Cr,N) doping levels above $\sim$5–7 at% Cr, in addition to capping, negatively affected the growth of crystalline TiO_2, for these conditions.

For CCS-LAO-Cap, similar results as for CCS-Si-Cap were obtained at the first plume center. The sample was not divided into equivalent areas as CCS-Si-Cap, but it appeared that the LAO substrate was able to sustain the anatase phase for higher doping levels than the Si substrate. This was suggested through the fact that a film peak was only seen close to the A (004) location, close to the wafer center. At the second plume center, no film peaks were observed, indicating amorphous materials in the film.

For all the doped samples, traces of CrO_2 and Cr_2O_3 have been observed in areas with higher doping concentrations. No traces of CrN have been reported.

6 Conclusion

Uniform undoped and Continuous Compositional Spread (CCS) (Cr,N)-doped TiO_2 films, deposited by conventional and combinatorial pulsed laser deposition (PLD), respectively, have been studied using conventional θ–2θ X-Ray Diffraction (XRD), Grazing-Incidence X-Ray-Diffraction (GIXRD), High Resolution X-Ray Diffraction (HRXRD) and Raman spectroscopy. The investigated films were deposited on Si (100), LAO (001), STO (001) and sapphire (0001) substrates.

The amount of anatase-to-rutile in the uniform undoped samples was seen to be heavily influenced by the oxygen pressure during deposition. For no oxygen flow, stoichiometric transfer from the TiO_2 target did not seem to occur. It was seen that low oxygen pressures favored the rutile phase, while high oxygen pressures favored the anatase phase, according to XRD characterizations.

The majority of the undoped uniform samples displayed texture or some preferred orientations. For TiO_2 deposited on Si (which had oxidized, amorphous SiO_2 surfaces), the (100) orientation generally seemed to be preferred for the rutile phase. For the anatase phase, the (001) and (112) orientations seemed to dominate. No correlation was found between rutile (100) and anatase (112) planes, and it was suggested that the anatase–to–rutile transformation at anatase (112) twin boundaries had not occured.

It was found that the choice of substrate significantly altered the films' phase composition and texture. For STO (001) and LAO (001) substrates, highly textured anatase (001) was seen, even for deposition parameters which seemed to favor rutile growth. For sapphire (0001) substrates, textured rutile (100) was observed, even for parameters which seemed to favor anatase growth. This was attributed to low lattice mismatch with the substrates.

Some of the films on LAO and STO susbtrates were found to consist of both textured anatase, as well as un-textured rutile. Because of this, the sample characteristics were substantially different in GIXRD compared to θ–2θ XRD. It was concluded that GIXRD was not a sufficient characterization method for these samples. The growth mechanics that allowed for these characteristics were not investigated, but it was suggested that the anatase (001) grew pseudomorphically up to a certain film thickness, after which rutile grains started to dominate.

It was found that the samples with lower laser fluence and higher oxygen pressures, in addition to smaller film thickness (A2 samples), showed the highest crystalline quality on all substrates. However, since more than one deposition parameter separated them from the B–series samples, it is difficult to determine what caused the overall higher quality. It is speculated that lower kinetic energy the deposited species was a contributing factor.

The XRD results for the undoped uniform TiO_2 films were in general confirmed by Raman spectroscopy.

For the (Cr,N)-doped TiO_2 films on Si, it was seen that introduction of (Cr,N)-doping, as well as cycling to N_2 gas during parts of the deposition, significantly

altered the structural composition of the films. The doping and gas cycling seemed to negatively impact the quality of the anatase components in the film. However, it was observed that both increased (Cr,N) doping concentrations as well as N_2 gas favored growth of rutile (100).

Based on the XRD analysis, one can conclude that although the (Cr,N)-doping negatively affected the anatase crystalline quality, the deposition parameters themselves did not seem ideal for anatase growth, even in the undoped case. See suggestions for future work for further comments on this.

For the (Cr,N)-doped film on LAO (001), the trends were similar to that of the films on Si. However, it did appear as though the LAO substrate was able to sustain anatase growth for higher doping levels than for the Si substrates.

The Raman spectroscopy results for the doped samples generally confirmed the conclusions drawn from the XRD analysis.

7 Suggestions for Future Work

This work has been an investigation of the “bigger picture” characteristics of the samples. XRD methods such as those presented here offer statistical insight, but does not allow for a nanoscale view of the sample structures. This means that the nanoscale origins of many of the characteristics described here are unknown.

A valuable study would be to investigate the origins of the substrate-influenced growth. It was seen that the substrates were able to “force” either rutile or anatase, even for deposition parameters which seemed to favor the other phase. This could be investigated by TEM, which could provide insight into the growth mechanisms for the samples, by studying the nature of the grains that grew close to the substrate.

Some samples were also seen to consist of highly textured anatase, as well as untextured rutile. The nature of this coexistence could also be investigated using TEM. It was proposed in this thesis that the anatase phase grew from the substrate and up to a certain thickness, before rutile grains started to dominate, and TEM might provide confirmation or refutal of this. Another way of investigating the above, is by employing measurement techniques that allow for depth profiling, such as depth-profiling Raman spectroscopy methods, which were not used in this thesis.

The A and B–series samples were seen to be substantially different from each other. However, there were more than one deposition parameter that separated them. It is suggested that one deposits a series of TiO_2 on STO, LAO, Si and sapphire substrates, by only changing *one* parameter from, for instance, the B5 parameters to A2 parameters. An example of this could be to deposits films using the same pressures as in B1–B5, but changing the laser fluences to what was used for A2 ($0.8\,J/cm^2$). By then performing similar characterization as was performed here, more insight into the tuning of TiO_2 deposition may be gained.

It was found that the (Cr,N) doping negatively affected the anatase film of the films, and that capping *further* deteriorated the quality. However, it was suggested that increasing doping levels *increasingly favored* (001)-oriented rutile. If one wants to produce crystalline, (Cr,N)-doped TiO_2, this might be acheived by using rutile-favorable deposition parameters. In particular, since B4 on sapphire was seen to highly favor rutile, depositing a series of (Cr,N)-doped TiO_2 films on sapphire might lead to high quality, doped rutile films. Doing similar characterization as in this thesis might shed light on whether this high quality has been achieved.

It was also found that the deposition parameters were in general not ideal for anatase growth, as they all resulted in some polycrystalline rutile when growing on Si. It is therefore suggested that one can achieve better crystalline quality in (Cr,n)-doped anatase by using more anatase-favorable deposition parameters.

The films deposited with lower laser fluence were consistently of a higher quality than those with higher fluence. It is then natural to suspect that if one can ablate the TiO_2 target with lower fluence (i.e., $0.8\,J/cm^2$), while still ablating the CrN target with a sufficiently high fluence, this might lead to better overall crystalline quality of (Cr,N)-doped films.

References

[1] H.-O. Pörtner, D. Roberts, E. Poloczanska, K. Mintenbeck, M. Tignor, A. Alegría, M. Craig, S. Langsdorf, S. Löschke, V. Möller, and A. Okem, "Ipcc, summary for policymakers," 2022.

[2] D. O. Liu Zhenmin, Achim Steiner, "Theme report on energy transition: Towards the achievement of sdg 7 and net-zero emissions," 2021.

[3] IRENA, "Future of solar photovoltaic: Deployment, investment, technology, grid integration and socio-economic aspects (a global energy transformation: paper)," 2019.

[4] M. Green, *Third Generation Photovoltaics: Advanced Solar Energy Conversion.* Physics and astronomy online library, Springer, 2003.

[5] W. Shockley and H. J. Queisser, "Detailed balance limit of efficiency of p-n junction solar cells," *Journal of Applied Physics*, vol. 32, no. 3, pp. 510–519, 1961.

[6] A. Luque and A. Martí, "Increasing the efficiency of ideal solar cells by photon induced transitions at intermediate levels," *Phys. Rev. Lett.*, vol. 78, pp. 5014–5017, Jun 1997.

[7] A. Luque and A. Marti, "A metallic intermediate band high efficiency solar cell," *Progress in Photovoltaics: Research and Applications*, vol. 9, pp. 73 – 86, 04 2001.

[8] A. Luque and A. Martí, "The intermediate band solar cell: Progress toward the realization of an attractive concept," *Advanced Materials*, vol. 22, no. 2, pp. 160–174, 2010.

[9] W. Zhu, X. Qiu, V. Iancu, X.-Q. Chen, H. Pan, W. Wang, N. M. Dimitrijevic, T. Rajh, H. M. Meyer, M. P. Paranthaman, G. M. Stocks, H. H. Weitering, B. Gu, G. Eres, and Z. Zhang, "Band gap narrowing of titanium oxide semiconductors by noncompensated anion-cation codoping for enhanced visible-light photoactivity," *Phys. Rev. Lett.*, vol. 103, p. 226401, Nov 2009.

[10] A. Fujishima and K. Honda, "Electrochemical photolysis of water at a semiconductor electrode," *Nature*, vol. 238, pp. 37–38, Jul 1972.

[11] A. L. Linsebigler, G. Lu, and J. T. Yates, "Photocatalysis on tio2 surfaces: Principles, mechanisms, and selected results," *Chemical Reviews*, vol. 95, no. 3, pp. 735–758, 1995.

[12] M. Grätzel, "Photoelectrochemical cells," *Nature*, vol. 414, pp. 338–344, Nov 2001.

[13] R. Wang, K. Hashimoto, A. Fujishima, M. Chikuni, E. Kojima, A. Kitamura, M. Shimohigoshi, and T. Watanabe, "Light-induced amphiphilic surfaces," *Nature*, vol. 388, pp. 431–432, Jul 1997.

[14] K. Sunada, Y. Kikuchi, K. Hashimoto, and A. Fujishima, "Bactericidal and detoxification effects of tio2 thin film photocatalysts," *Environmental Science & Technology*, vol. 32, no. 5, pp. 726–728, 1998.

[15] W. Zhu, X. Qiu, V. Iancu, X.-Q. Chen, H. Pan, W. Wang, N. M. Dimitrijevic, T. Rajh, H. M. Meyer, M. P. Paranthaman, G. M. Stocks, H. H. Weitering, B. Gu, G. Eres, and Z. Zhang, "Band gap narrowing of titanium oxide semiconductors by noncompensated anion-cation codoping for enhanced visible-light photoactivity," *Phys. Rev. Lett.*, vol. 103, p. 226401, Nov 2009.

[16] C. Kittel, *Introduction to Solid State Physics.* Wiley, 8th ed. ed., 2004.

[17] B. Cullity and S. Stock, *Elements of X-ray Diffraction, Third Edition.* Prentice-Hall, 2001.

[18] H. P. Klug and L. E. Alexander, *X-ray diffraction procedures for polycrystalline and amorphous materials / Harold P. Klug, Leroy E. Alexander.* Wiley New York, 2nd ed. ed., 1974.

[19] A. Pandey, S. Dalal, S. Dutta, and A. Dixit, "Structural characterization of polycrystalline thin films by x-ray diffraction techniques," *Journal of Materials Science: Materials in Electronics*, vol. 32, pp. 1341–1368, Jan 2021.

[20] M. Bouroushian, "Characterization of thin films by low incidence x-ray diffraction," *Crystal Structure Theory and Applications*, vol. 01, pp. 35–39, 01 2012.

[21] A. Orlando, F. Franceschini, C. Muscas, S. Pidkova, M. Bartoli, M. Rovere, and A. Tagliaferro, "A comprehensive review on raman spectroscopy applications," *Chemosensors*, vol. 9, no. 9, 2021.

[22] D. A. H. Hanaor and C. C. Sorrell, "Review of the anatase to rutile phase transformation," *Journal of Materials Science*, vol. 46, pp. 855–874, Feb 2011.

[23] H. Tang, K. Prasad, R. Sanjinès, P. E. Schmid, and F. Lévy, "Electrical and optical properties of tio2 anatase thin films," *Journal of Applied Physics*, vol. 75, no. 4, pp. 2042–2047, 1994.

[24] F. De Angelis, C. Di Valentin, S. Fantacci, A. Vittadini, and A. Selloni, "Theoretical studies on anatase and less common tio2 phases: Bulk, surfaces, and nanomaterials," *Chemical Reviews*, vol. 114, no. 19, pp. 9708–9753, 2014. PMID: 24926899.

[25] S.-D. Mo and W. Y. Ching, "Electronic and optical properties of three phases of titanium dioxide: Rutile, anatase, and brookite," *Phys. Rev. B*, vol. 51, pp. 13023–13032, May 1995.

[26] C. J. Howard, T. M. Sabine, and F. Dickson, "Structural and thermal parameters for rutile and anatase," *Acta Crystallographica Section B*, vol. 47, no. 4, pp. 462–468, 1991.

[27] J. Zemann, "Crystal structures, 2nd edition. vol. 1 by r. w. g. wyckoff," *Acta Crystallographica*, vol. 18, no. 1, pp. 139–139, 1965.

[28] K. Momma and F. Izumi, "*VESTA3* for three-dimensional visualization of crystal, volumetric and morphology data," *Journal of Applied Crystallography*, vol. 44, pp. 1272–1276, Dec 2011.

[29] M. Lazzeri, A. Vittadini, and A. Selloni, "Structure and energetics of stoichiometric tio_2 anatase surfaces," *Phys. Rev. B*, vol. 63, p. 155409, Mar 2001.

[30] U. Balachandran and N. Eror, "Raman spectra of titanium dioxide," *Journal of Solid State Chemistry*, vol. 42, no. 3, pp. 276–282, 1982.

[31] B. Lafuente, R. T. Downs, H. Yang, and N. Stone, *1. The power of databases: The RRUFF project*, pp. 1–30. De Gruyter (O), 2015.

[32] D. P. Norton, *Pulsed Laser Deposition of Complex Materials: Progress Toward Applications*, ch. 1, pp. 1–31. John Wiley & Sons, Ltd, 2006.

[33] S. S. Chu and C. P. Grigoropoulos, "Determination of Kinetic Energy Distribution in a Laser-Ablated Titanium Plume by Emission and Laser-Induced Fluorescence Spectroscopy ," *Journal of Heat Transfer*, vol. 122, pp. 771–775, 06 2000.

[34] M. Ohring, "Chapter 8 - epitaxy," in *Materials Science of Thin Films (Second Edition)* (M. Ohring, ed.), pp. 417–494, San Diego: Academic Press, second edition ed., 2002.

[35] F. C. Frank, J. H. van der Merwe, and N. F. Mott, "One-dimensional dislocations. i. static theory," *Proceedings of the Royal Society of London. Series A. Mathematical and Physical Sciences*, vol. 198, no. 1053, pp. 205–216, 1949.

[36] D. Smith and I. index, *Thin-Film Deposition: Principles and Practice.* McGraw-Hill Education, 1995.

[37] A. Rosnes, "Tem study of cr, n codoped tio_2 thin film - structural properties of continous compositional spread film," Master's thesis, NTNU, june 2022.

[38] G. Carter, "Preferred orientation in thin film growth — the survival of the fastest model," *Vacuum*, vol. 56, no. 2, pp. 87–93, 2000.

[39] A. van der Drift, "Evolutionary selection, a principle governing growth orientation in vapour-deposited layers," *Philips research reports*, vol. 22, 1967.

[40] T. Hom, W. Kiszenik, and B. Post, "Accurate lattice constants from multiple reflection measurements. ii. lattice constants of germanium silicon, and diamond," *Journal of Applied Crystallography*, vol. 8, no. 4, pp. 457–458, 1975.

[41] "Crystalline oxygen compounds from a to z." Accessed: 2022-07-06.

[42] M. Schreyer, L. Guo, S. Thirunahari, F. Gao, and M. Garland, "Simultaneous determination of several crystal structures from powder mixtures: the combination of powder x-ray diffraction, band-target entropy minimization and rietveld methods," *Journal of Applied Crystallography*, vol. 47, no. 2, pp. 659–667, 2014.

[43] H. Long, G. Yang, A. Chen, Y. Li, and P. Lu, "Growth and characteristics of laser deposited anatase and rutile tio2 films on si substrates," *Thin Solid Films*, vol. 517, no. 2, pp. 745–749, 2008.

[44] M. Walczak, E. Papadopoulou, M. Sanz, A. Manousaki, J. Marco, and M. Castillejo, "Structural and morphological characterization of tio2 nanostructured films grown by nanosecond pulsed laser deposition," *Applied Surface Science*, vol. 255, no. 10, pp. 5267–5270, 2009. Laser and Plasma in Micro- and Nano-Scale Materials Processing and Diagnostics.

[45] E. György, A. Pérez, A. Pérez Del Pino, G. Sauthier, A. Figueras, F. Alzina, and J. Pascual, "Structural, morphological and local electric properties of tio2 thin films grown by pulsed laser deposition," *Journal of Physics D Applied Physics*, vol. 40, pp. 5246–5251, 09 2007.

[46] X.-S. Zhou, Y.-H. Lin, B. Li, L.-J. Li, J.-P. Zhou, and C.-W. Nan, "Processing and characterization of tio_2 film prepared on glass via pulsed laser deposition," *Journal of Physics D: Applied Physics*, vol. 39, pp. 558–562, jan 2006.

[47] C. C. Hsieh, K. H. Wu, J. Y. Juang, T. M. Uen, J.-Y. Lin, and Y. S. Gou, "Monophasic tio2 films deposited on srtio3(100) by pulsed laser ablation," *Journal of Applied Physics*, vol. 92, no. 5, pp. 2518–2523, 2002.

[48] K. Krupski, A. Sanchez, A. Krupski, and C. McConville, "Optimisation of anatase tio2 thin film growth on laalo3(0 0 1) using pulsed laser deposition," *Applied Surface Science*, vol. 388, pp. 684–690, 2016. E-MRS 2015 Fall Meeting, Symposium D: "12th International Symposium on Electrochemical/Chemical Reactivity of New Materials (ECRNM 12) – Surface Science – key to understand advanced materials" 15th-18th September 2015, Warsaw, Poland.

[49] S. Yamamoto, T. Sumita, T. Yamaki, A. Miyashita, and H. Naramoto, "Characterization of epitaxial tio2 films prepared by pulsed laser deposition," *Journal of Crystal Growth*, vol. 237-239, pp. 569–573, 2002. The thirteenth international conference on Crystal Growth in conj unction with the eleventh international conference on Vapor Growth and Epitaxy.

[50] V. Silva, V. Bouquet, S. Députier, S. Boursicot, S. Ollivier, I. Weber, V. Silva, I. Santos, M. Guilloux-Viry, and A. Perrin, "Substrate-controlled allotropic phases and growth orientation of tio 2 epitaxial thin films," *Journal of Applied Crystallography*, vol. 43, no. 6, p. 1502 – 1512, 2010.

[51] C. Weidenthaler, "Pitfalls in the characterization of nanoporous and nanosized materials," *Nanoscale*, vol. 3, pp. 792–810, 2011.

[52] Bruker AXS, *DIFFRAC.SUITE User Manual*, April 2021.

[53] J. I. Langford and A. J. C. Wilson, "Scherrer after sixty years: A survey and some new results in the determination of crystallite size," *Journal of Applied Crystallography*, vol. 11, no. 2, pp. 102–113, 1978.

[54] U. Holzwarth and N. Gibson, "The scherrer equation versus the 'debye-scherrer equation'," *Nature Nanotechnology*, vol. 6, pp. 534–534, Sep 2011.

[55] C. S. Barrett and T. B. Massalski, *Structure of metals : crystallographic methods, principles and data / C.S. Barrett, T.B. Massalski*. Pergamon Oxford ; New York, 3rd rev. ed. ed., 1980.

[56] G. Harris, "X. quantitative measurement of preferred orientation in rolled uranium bars," *The London, Edinburgh, and Dublin Philosophical Magazine and Journal of Science*, vol. 43, no. 336, pp. 113–123, 1952.

[57] R. A. Spurr and H. Myers, "Quantitative analysis of anatase-rutile mixtures with an x-ray diffractometer," *Analytical Chemistry*, vol. 29, no. 5, pp. 760–762, 1957.

[58] M. R. Jorge, *Potential Oxide-Based Intermediate Band Materials: Fabrication and Photoemission Studies*. PhD thesis, NTNU, 2020.

[59] M. Mohammadtaheri, Q. Yang, Y. Li, and J. Corona-Gomez, "The effect of deposition parameters on the structure and mechanical properties of chromium oxide coatings deposited by reactive magnetron sputtering," *Coatings*, vol. 8, no. 3, 2018.

[60] W. H. Baur and A. A. Khan, "Rutile-type compounds. iv. sio2, geo2 and a comparison with other rutile-type structures," *Acta Crystallographica Section B*, vol. 27, no. 11, pp. 2133–2139, 1971.

[61] L. W. Finger and R. M. Hazen, "Crystal structure and isothermal compression of fe2o3, cr2o3, and v2o3 to 50 kbars," *Journal of Applied Physics*, vol. 51, no. 10, pp. 5362–5367, 1980.

[62] G. Nolze, G. Wagner, R. Neumann, R. Skala, and V. Geist, "Orientation relationships of carlsbergite in schreibersite and kamacite in the north chile iron meteorite," *Mineralogical Magazine*, vol. 70, pp. 373–382, 08 2006.

Appendix

A Basic crystallography

This section presents basic theory and conventions for crystallography as a setup for the X-ray diffraction theory. The theory presented in this section is based on Chapters 1 and 2 of Kittel [16] and Chapter 2 of Cullity [17]. Citations will be omitted unless a reference is appropriate.

Crystals are defined as solids composed of atoms, ions or molecules arranged in a periodic pattern in three dimensions. A common way of understanding crystals is to first ignore the actual atoms or molecules, and instead represent the crystals as a *lattice*, where the set of points $\mathbf{r}$:

$$\mathbf{r} = m\mathbf{a}_1 + n\mathbf{a}_2 + o\mathbf{a}_3 \tag{19}$$

define the lattice. Here, m, n, o are integers, and $\mathbf{a_1}$, $\mathbf{a_2}$, $\mathbf{a_3}$ are translation vectors that define the lattice. The atoms, ions or molecules are then introduced through the *basis* of the crystal structure. The center of atom j relative to the associated lattice point is then

$$\mathbf{r}_j = u_j\mathbf{a}_1 + v_j\mathbf{a}_2 + w_j\mathbf{a}_3, \tag{20}$$

where u, v, w are real numbers such that $0 \leq u_j, v_j, w_j \leq 1$.

The direction of any line in a crystal lattice may be represented by its *indices* as $[uvw]$. Negative directions are represented by a bar, e.q. $[\overline{u}vw]$. Note that the same direction may be defined by an infinite number of lines, but conventionally, the lowest set of integers indices are used, so that $[\frac{1}{2}\frac{1}{2}1]$, [112] and [224] are all represented by [112].

Wherever a set of directions are related by symmetry, they may all be represented by the indices of one of the directions through angular brackets, as $\langle uvw \rangle$. An example is the four body diagonals of a cube, [111], $[1\overline{1}1]$, $[\overline{1}\overline{1}1]$ and $[\overline{1}11$, which may all be represented by $\langle 111 \rangle$.

Miller indices

An important and popular convention, which will be consistently employed in this thesis, is the use of *Miller indices* to represent planes in a crystal structure. For any plane in a crystal lattice, the Miller indices (hkl) are defined as the reciprocal of the plane's intercepts with the crystallographic axes. A plane with Miller indices (hkl) will thus intercept the crystallographic axes at $1/h$, $1/k$ and $1/l$. When the lengths of the lattice vectors are a, b, c, the planes will intercept the axes at a/h, b/k, c/l. Whenever a plane is parallel to an axis, then the index for that axes is 0.

Interplanar spacing

The space between two neighboring planes in a set of planes (hkl) is denoted by d_{hkl}, and is called the *d-spacing*. The d-spacing depends on the relative magnitudes and angles between the lattice vectors. For the cubic crystal system, the d-spacing is given by

$$\frac{1}{d^2} = \frac{h^2 + k^2 + l^2}{a^2} \qquad \text{(cubic)} \tag{21}$$

whereas for the tetragonal system, the d-spacing is given by

$$\frac{1}{d^2} = \frac{h^2 + k^2}{a^2} + \frac{l^2}{c^2} \qquad \text{(tetragonal)} \tag{22}$$

The reciprocal lattice

A concept which has important applications in diffraction is that of the *reciprocal lattice*. In terms of the crystal (previously defined) axis vectors of the crystal lattice, $\mathbf{a}_i$, the axis vectors of the reciprocal lattice are defined as

$$\mathbf{b}_1 = \frac{\mathbf{a}_2 \times \mathbf{a_3}}{\mathbf{a}_1 \cdot \mathbf{a}_2 \times \mathbf{a}_3}, \quad \mathbf{b}_2 = \frac{\mathbf{a}_3 \times \mathbf{a_1}}{\mathbf{a}_1 \cdot \mathbf{a}_2 \times \mathbf{a}_3}, \quad \mathbf{b}_3 = \frac{\mathbf{a}_1 \times \mathbf{a_2}}{\mathbf{a}_1 \cdot \mathbf{a}_2 \times \mathbf{a}_3} \tag{23}$$

Points $\mathbf{G}$ in the reciprocal lattice are thus described by

$$\mathbf{G} = m\mathbf{b}_1 + n\mathbf{b}_2 + o\mathbf{b}_3, \tag{24}$$

where m, n, o are integers.

The reciprocal lattice is the Fourier transform of the crystal lattice, and satisfies $\mathbf{b}_j \cdot \mathbf{a}_j = \delta_{ij}$, where δ_{ij} is the Kronecker delta. In this work, the reciprocal lattice will be said to reside in *reciprocal space*, while the crystal lattice will occupy the *real space*.

B XRD Signatures of CrO_2, Cr_2O_3 and CrN

Figure B.1 shows the powder XRD patterns of CrO_2 [60], Cr_2O_3 [61] and CrN [62].

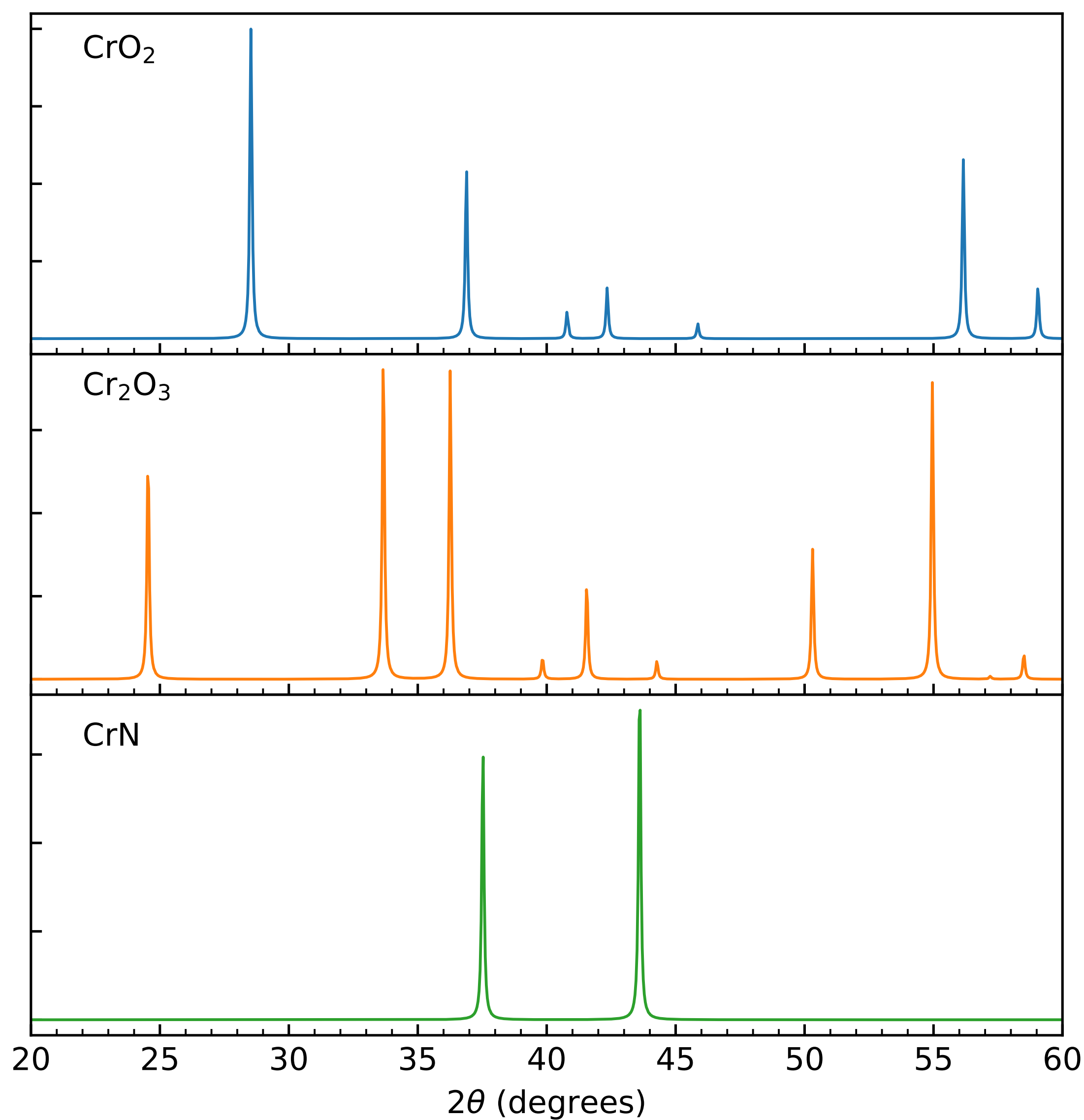

Figure B.1: Powder XRD patterns of CrO_2 [60], Cr_2O_3 [61] and CrN [62].

C CrN films deposited on silicon

The films described in this section were synthezied by Hogne Lysne and Thomas Brakstad as part of their PhD research.

Figure C.1 displays θ–2θ XRD data from two pulsed laser deposited films, deposited on a 2×2 inch Si wafer using a CrN target. One of the films was deposited with pure O_2 gas flow, and the other with cycling between O_2 and N_2 gas. The films are seen to be similar to polycrystalline Cr_2O_3, when analyzed by XRD.

Figure C.2 displays θ–2θ data from a pulsed laser deposited film, deposited on a Si wafer using a CrN target under pure N_2 gas.

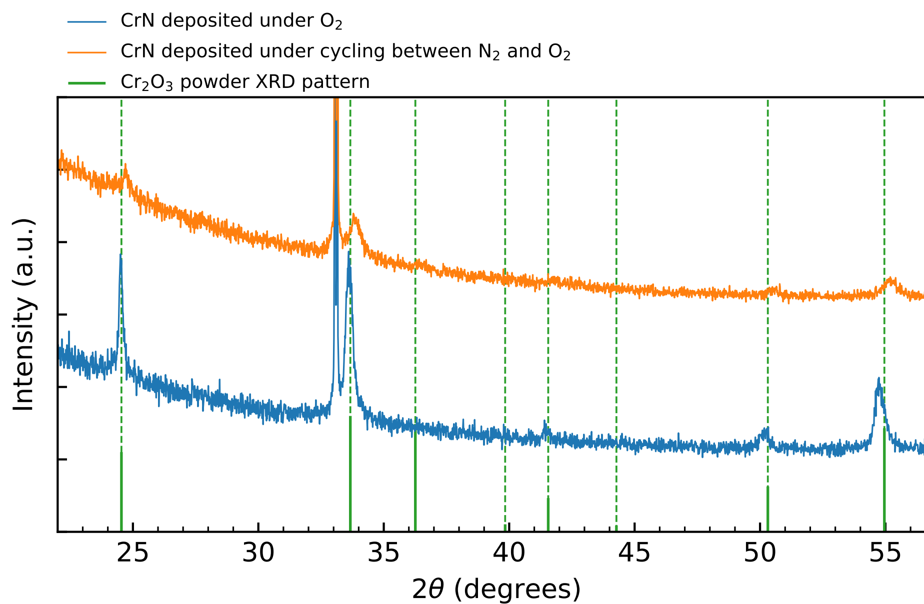

Figure C.1: θ–2θ XRD data from PLD deposited films on silicon, using a CrN target. The calculated powder XRD pattern for Cr_2O_3 [61] is shown.

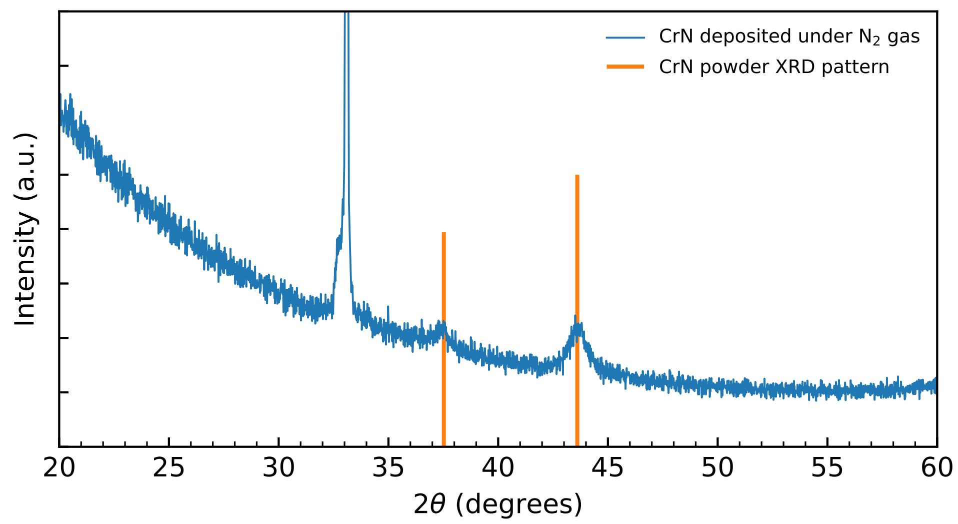

Figure C.2: θ–2θ XRD data from a PLD deposited film on silicon, using a CrN target under pure N_2 flow. The calculated powder XRD pattern for CrN [62] is shown.